

# Microtremor localisation based on cross-correlation stacking

Dissertation

Zur Erlangung des Doktorgrades der Naturwissenschaften im  
Fachbereich Geowissenschaften der Universität Hamburg

vorgelegt von

Mehrnoosh Behzadi

aus

Teheran, Iran

Hamburg

2015

Als Dissertation angenommen vom Fachbereich Geowissenschaften  
der Universität Hamburg

Auf Grund der Gutachten von Prof. Dr. Dirk Gajewski  
und PD Dr. Claudia Vanelle

Hamburg, den

*Laudation to the God of majesty and glory!*  
*Obedience to him is a cause of approach and gratitude in increase of benefits. Every*  
*inhalation of the breath prolongs life and every expiration of it gladdens our nature;*  
*wherefore every breath confers two benefits and for every benefit gratitude is due.*

-The Rose Garden of Sadi

*To my husband Mojtaba, without his love, patience, and encouragement it would not have been possible to write this doctoral thesis; and my parents Maryam and Ezatollah, who have over the years supported and guided me in my endeavors.*



# Contents

<b>Abstract</b>	<b>vii</b>
<b>1 Introduction</b>	<b>1</b>
1.1 Impulsive source . . . . .	1
1.2 Microtremor phenomena . . . . .	2
1.3 Non-volcanic tremors . . . . .	2
1.4 Localisation of tremors . . . . .	4
1.5 Thesis outline . . . . .	5
<b>2 Cross-correlation stacking based imaging</b>	<b>7</b>
2.1 Localisation and imaging conditions . . . . .	7
2.2 Travelttime computation . . . . .	10
2.2.1 Finite difference solution of the Eikonal equation . . . . .	10
2.2.2 Fast sweeping solution of the Eikonal equation . . . . .	11
2.2.3 Ray tracing . . . . .	12
2.3 Static moveout correction . . . . .	14
2.4 Cross-correlation . . . . .	15
2.5 Stacking . . . . .	16
2.6 Localisation with Three component measurements . . . . .	17
<b>3 Application to synthetic data</b>	<b>19</b>
3.1 Homogeneous medium . . . . .	19
3.2 Travelttime error in homogeneous medium . . . . .	21
3.3 Heterogeneous medium . . . . .	23
3.4 Localisation in a blocky velocity model . . . . .	24
3.4.1 Point source . . . . .	24
3.4.2 Microtremors simulated by explosion source . . . . .	27
3.5 Smoothing the velocity model . . . . .	28
3.6 First and most energetic arrivals . . . . .	30
3.7 Localisation in the smoothed velocity model . . . . .	31
3.7.1 Point source . . . . .	31
3.7.2 Microtremors simulated by explosion source . . . . .	34
3.7.3 Microtremors simulated by horizontal single force . . . . .	36
3.7.4 Microtremors simulated by Vertical single force . . . . .	37

---

<b>4</b>	<b>Acquisition footprint and propagation effects</b>	<b>41</b>
4.1	Geometrical spreading compensation . . . . .	41
4.2	Acquisition footprint . . . . .	43
4.3	Application to synthetic data with an impulsive source . . . . .	48
<b>5</b>	<b>Application to field data</b>	<b>55</b>
5.1	Induced microseismic event . . . . .	55
5.2	Non-volcanic tremors in the Cascadia . . . . .	60
<b>6</b>	<b>Conclusion</b>	<b>75</b>
6.1	Summary . . . . .	75
6.2	Outlook . . . . .	77
	<b>Bibliography</b>	<b>79</b>
	<b>List of Figures</b>	<b>79</b>
	<b>Acknowledgements</b>	<b>86</b>
	<b>Eidesstattliche Versicherung</b>	<b>87</b>

# *Abstract*

Passive seismic methods are of high interest to the petroleum industry. Reservoir monitoring, hydro-fracture mapping and imaging enhanced oil recovery are only a few applications of passive seismic methods in exploration seismics. Passive seismic methods reduce the number of unnecessary wells and contribute to a cleaner and environmentally friendlier exploration process. In this case exploration teams can identify reservoir prospects easier, reduce the number of holes drilled, reduce drilling costs, and cut exploration time. This leads to economic and environmental benefits: a reliable, affordable environmentally sustainable technology in the oil and gas exploration is one of the major challenges facing society.

In this study, a new passive seismic method based on cross-correlation and stacking, is introduced to localise the elastic emissions. The new method is applied to point source and microtremor data, in order to highlight some of its advantages and disadvantages. The method does not require picking of events and uses all recorded channels simultaneously, which allows to detect even very small events. The method has similarities to the diffraction stacking method and differs particularly in the way the time axis is collapsed in the imaging process which is performed by zero lag cross-correlation. The maximum value of the image obtained by this method provides the source location.

Since in passive seismic the target zone can be located in access-limited environments, the acquisition geometry often follows a sparse irregular pattern, which can have a significant effect on the results: The spatial distribution of input traces is irregular, the results are often contaminated by acquisition artifacts. To achieve a higher resolution image, an alternative algorithm based on Voronoi cells is proposed countermand the effect of acquisition footprint. Thus weighting the data in this case results in a better focused image function with lower noise, however sometimes it leads to artificial focusing in the image.

I apply the procedure to synthetic data modelled with different source types, acquisition geometries and apertures. Weighting the data results in a more focused image function and improves the image by reducing the amount of noise, however sometimes it leads to artificial focusing in the image. The moveout of first and most energetic arrivals are considered. Finally I apply the method to field data examples as well, which comprise a microseismic event from a hydro-fracturing reservoir and non volcanic tremors from a subduction zone. The localisation result obtained by cross-correlation stacking demonstrate the new method's robustness and its potential for real time monitoring of the subsurface.



# Chapter 1

## Introduction

Seismic events are the result of release of energy on the surface or within the Earth. In general, all seismic events contain the valuable information about the Earth's interior and processes going on inside. Thus, localisation of these events can give us an important insight into properties and physical processes in the Earth. Seismic monitoring is a key problem in seismology toward understanding the physics of the rupture process, Seismic monitoring has recently gained grow in oil and gas industry. Real-time seismic monitoring of natural or induced seismic events in or around oil and gas production or waste water injection provides operators with the data needed to manage their operations and assess potential risk of induced seismicity.

### 1.1 Impulsive source

A source which concentrates its energy then releases it simultaneously at a point in space, is known as impulsive source. Numerical studies of this work relies mainly on two types of impulsive sources, i.e., explosion and oriented sources. The explosion source is the simplest source model and is expected to produce an outward directed compressional first motion in all directions. Theoretically, for the explosion case, only P-waves are generated, but as a pure explosion is not possible, real explosions generate some S-waves. Whereas oriented source represents a directed force and is called single force source. a single force on the Earth may result from an acceleration of the centre of mass of the source in the direction opposite to the force, or deceleration of the centre of mass of the source in the same direction as the force [[Šílený and Milev, 2005](#)].

## 1.2 Microtremor phenomena

For the past four decades, the Earth's ambient noise is being extensively used for sedimentary basin studies and, particularly, seismic hazard and microzonation studies. Nevertheless, only in the past ten years have passive seismic techniques, applicable to seismic ambient noise, gained growing interest for hydrocarbon exploration, scientifically as well as economically [Emidio and Nunes, 2010; Graf et al., 2007; Saenger et al., 2007]. These techniques do not require artificial sources or large number of personnel, therefore the costs are low. Furthermore, they can be used in sensitive environments where conventional seismic methods face problems [Emidio and Nunes, 2010]. Moreover, passive seismic techniques reduce the number of unnecessary drilled wells and contribute to a cleaner and environmentally friendlier exploration process. Recently, passive seismic methods have even been suggested as a tool to detect a direct hydrocarbon indicator [Graf et al., 2007; Lambert et al., 2009; Saenger et al., 2007; Steiner, 2009].

Passive seismic methods use a simple empirical observation of an increase in the ambient seismic noise's spectral energy at a frequency range around 1 to 6 Hz in the presence of hydrocarbons. Such frequency anomalies have been observed above several hydrocarbon reservoirs but not outside the reservoir area (see Figure 1.1). Figure 1.1(b) demonstrates a typical structure of a reservoir with two receivers on the surface. One receiver is set above the reservoir and the other outside the reservoir area. Waves depicted in black define the background noise and those in red define the ambient seismic noises due to the reservoir. The spectrum of vertical component seismograms, which are shown in Figure 1.1(a), show the existence of a high amplitude anomaly between 2 to 4 Hz above the reservoir, whereas it is absent outside the reservoir area. Although the origin of the spectral anomalies is yet unexplained, a possible source could be the resonant oscillation of oil and gas within the reservoir [Steiner, 2009]. This phenomenon represents a low-frequency event which is also referred to as microtremor. Microtremors continuously emit seismic energy over a durations from few hours to weeks from the source area. In contrast, classical seismic events usually last seconds. Microtremor events are also observed in volcanic areas and in several subduction zones.

## 1.3 Non-volcanic tremors

For a long time, it was widely believed that regular earthquakes are the main observable mechanism by which major plate boundary faults release stress. Recent observations of slow slip and/or deep non-volcanic tremor (NVT) at several major world faults force geophysicists to research this phenomenon. Now, it appears that slow slip and tremors represent important modes of faults releasing stress. Studying these paradigms is essential for a better understanding of the physics of earthquakes and fault zones. NVTs are

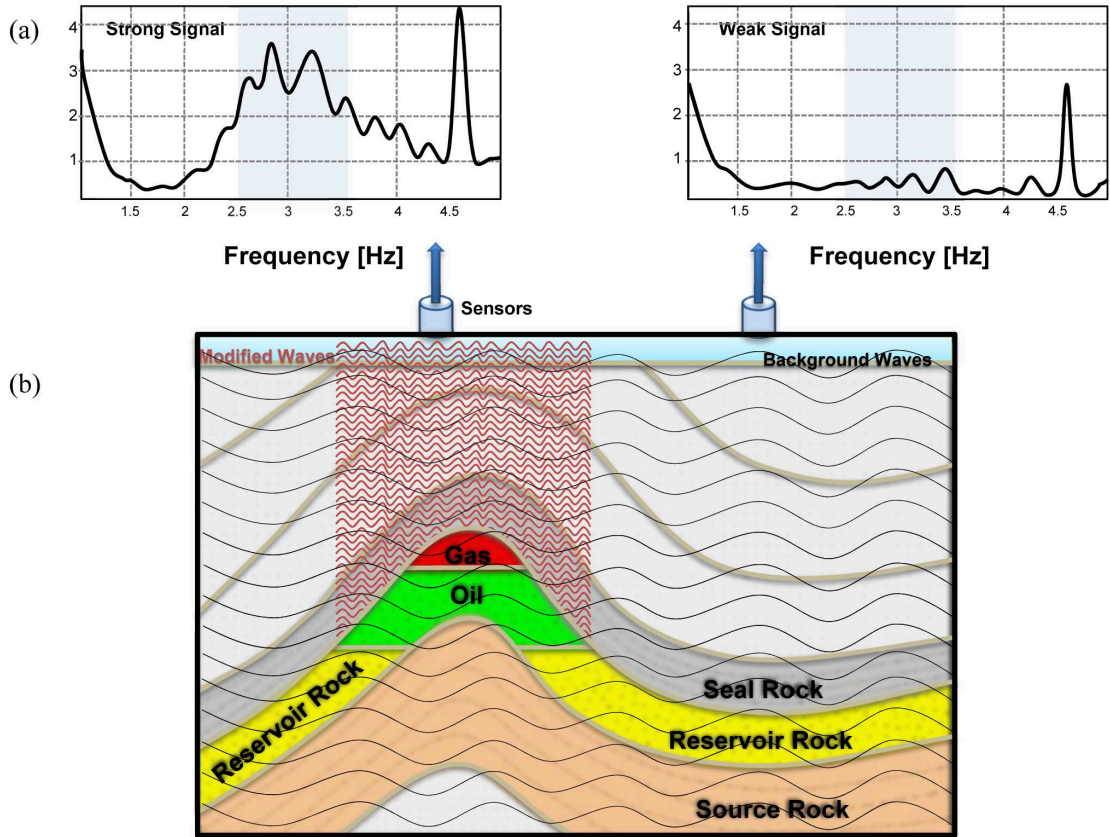


FIGURE 1.1: Schematic passive technology (a) Spectral microtremor analysis from field survey in Austria [Steiner, 2009]; (b) Typical geological structure with two receivers on the surface. One receiver is set above the reservoir and the other outside the reservoir area. Waves depicted in black define the background noise and those in red define the ambient seismic noises due to the reservoir. The spectrums of vertical component seismograms, show the existence of a high amplitude anomaly between 2 to 4 Hz above the reservoir, whereas it is absent outside the reservoir area.

characterised by apparently noise-like, emergent waveforms that are depleted in high-frequency energy, in contrast to regular small earthquakes. NVTs last for a few seconds to several days, and have envelopes which are coherent at seismic stations kilometres apart [Ghosh, 2011].

In subduction zones, slow slip and tremors are often coupled in space and time [Ghosh, 2011]. NVT has been observed in several tectonically active regions. In Cascadia, USA, and southwest Japan (e.g. Osaka), a relation of NVTs' occurrences with the subduction dynamics is inferred from the current occurrence of slow slip, which is detected geodetically [Obara, 2002; Obara and Hirose, 2006]. In these regions, the occurrence of major episodic tremor and slip (ETS) events is surprisingly periodic [Rogers and Dragert, 2003]. Minor NVT has been triggered by the stresses imposed by low-frequency seismic

waves radiated by major distant earthquakes [Calvert et al., 2011; Miyazawa and Mori, 2005]. Also, NVT is modulated by ocean tidal loading, indicating that small stress perturbations trigger it [Rubinstein et al., 2008]. NVT is characterised by low amplitudes, lack of energy at high frequencies, emergent onsets, absence of clear impulsive phases, and durations from seconds to days [Obara, 2002; Obara and Hirose, 2006]. Due to the lack of impulsive phases, which are identifiable across seismic networks, conventional techniques fail to accurately locate NVT source positions.

Tremor episodes which continue for several days are accompanied by geodetically observed slow slip in both Cascadia and southwest Japan [Ghosh, 2011; Obara, 2002; Obara and Hirose, 2006; Rogers and Dragert, 2003]. This fact leads to the widely accepted interpretation that tremors and slow slip are manifestations of the same process in southwest Japan. In contrast, attempts to locate tremor in Cascadia have resulted in a broad, 50 km-thick, distribution in depth [Kao et al., 2005; McClausland et al., 2005]. This leads to the interpretation that much of the tremor is related to fluid migrations throughout a large volume above the plate interface [Kao et al., 2005; La Rocca et al., 2009; McClausland et al., 2005].

## 1.4 Localisation of tremors

Being able to localise the origin of microtremor events would be helpful in seismology, volcanology, and hydrocarbon studies. The key step in these studies is always the reliable localisation of the origin of the microtremor data. However, since microtremors are continuous in time, they can not be picked. The localisation of microtremors therefore requires other techniques than those applicable for classical seismic events [e.g., Eisner et al., 2006; Grasso, 1992]. Imaging or back projection methods, as used for active seismic data, have not yet exploited their potential as localisation techniques, but can be considered a starting point for such a technique. In microtremor localisation, the time axis is collapsed (steered by an appropriate imaging condition) to obtain a source image, however, requires special consideration.

Gajewski and Tessmer [2005] introduced a localisation method based on reverse time modelling, which does not require any picking of events and uses all recordings simultaneously. The advantage of this method is that the focused energy in the back projection process allows to image very weak events, which could not be identified in an individual seismogram of the recording network. Later, Gajewski et al. [2007] proposed a new technique based on a diffraction stacking approach to back project passive seismic observations. The subsurface is discretised and each subsurface discrete point is considered to be a potential location of a seismic event. Zhebel [2013] extended the diffraction stacking method as a suitable tool to locate the origin of seismic events even when the



signal-to-noise ratio (SNR) <sup>1</sup> is rather poor. [Zhebel et al. \[2011\]](#) studied the impact of the acquisition geometry and propagation effects as well.

[Steiner et al. \[2008\]](#) applied time reverse modelling (TRM) to image microtremor events to the subsurface. Their idea of locating the spatial origin of signals with time reverse modelling has been adapted from existing studies by other authors in physics, medicine and seismology. Of various methods in TRM to collapse the time axis, [Steiner et al. \[2008\]](#) used the absolute particle displacement or velocity per grid point throughout the entire time of the reverse modelling. In this imaging condition, the highest values correspond to either the highest amplitude of one wave front or to the positive interference of recorded signals, which were reversely propagated to the corresponding subsurface locations.

## 1.5 Thesis outline

This thesis deals with the development and the application of a new seismic imaging method based on cross-correlation stacking as a numerical tool to locate the elastic emissions tremor episodes. The tremor episodes may be generated by various anthropogenic types of sources, e.g. atmospheric disturbances, media fractures, underground movement of magmatic, or hydrothermal fluids. Hence observation, detection and localisation of tremors can gain useful information on dynamic properties of the subsurface. I develop a localisation method based on cross-correlation stacking, for imaging low frequency tremor episodes measured by passive seismics. In passive seismics a variety of techniques are used for detecting natural low frequency Earth movements, usually with the purpose of understanding geological structure and locating underground hydrocarbon reservoirs or other resources.

Although passive seismic sources have been monitored and studied [[Eisner et al., 2011](#); [Emidio and Nunes, 2010](#); [Graf et al., 2007](#); [Ryberg et al., 2010](#); [Steiner et al., 2008](#); [Zhebel et al., 2011](#)], a high resolution imaging process, which detects very weak events, has yet to be properly explored. This thesis seeks to improve existing knowledge of passive seismic monitoring by focussing on imaging the location of tremors by detecting their coherency. It should be noted that this research does not intend to discuss the physical explanation for tremors which is still a open problem. It rather focusses on the localisation of seismic events.

In chapter 2, a new localisation method is described, based on static moveout shift and cross-correlation stacking. It does not require picking of events and uses all recordings simultaneously. The cross-correlation serves as the imaging condition to collapse the time axis of the recording window.

---

<sup>1</sup> $SNR(db) = 20\log_{10}(\frac{A_{Signal}}{A_{Noise}})$

Chapter 3 illustrates the impact of different source types and different arrival traveltimes on the localisation results obtained by cross-correlation stacking. This imaging condition is equally applicable to point source events of short duration and microtremor events. Moreover, velocity error and smoothing the velocity model are discussed.

To improve the results and gain a better resolution of image, in chapter 4 an alternative algorithm is provided to solve the geometrical problems due to the ray propagation or so called geometrical spreading compensation and seismic array acquisition, known as acquisition footprint. Synthetic examples in 3-D are presented.

Several field examples for point source and microtremor data are presented in chapter 5 to verify and characterise the method.

Finally the general conclusions of the research and the outlook are given in chapter 6.

## Chapter 2

# Cross-correlation stacking based imaging

In this chapter theoretical fundamentals of localisation of seismic events based on Cross-correlation stacking is introduced.

### 2.1 Localisation and imaging conditions

The coherence of two traces follows from how well correlated they are. It can be quantified by the cross-correlation function [e.g., [Winter and Steinberg, 2008](#)]. In other words, cross-correlation is a measure of the similarity of two waveforms as a function of a time-lag between them. This property is exploited in the localisation method, that I describe in the following.

I consider a discretised subsurface, where each node of the subsurface grid represents a potential source location. The nodes are called image points in the following. The traveltimes from each image point to all the receiver locations of the recording network is determined. For this step a velocity model is required. For each image point the shortest traveltimes to a receiver is selected. This receiver represents the apex location of the corresponding traveltimes curve and is denoted zero time  $\tau_0$  (see [Figure 2.1\(a\)](#)). Based on the zero time, the moveout at the other receiver locations is determined and applied as a static shift to the input seismograms. For a consistent velocity model, the seismic events should align after applying the static moveout (SMO) shift for correct event location (see [Figure 2.1\(b\)](#)).

Then a zero-lag cross-correlation is applied, which represents the imaging condition, to collapse the time axis of the considered time window. In this process, any trace may be considered as the master trace for the correlation.

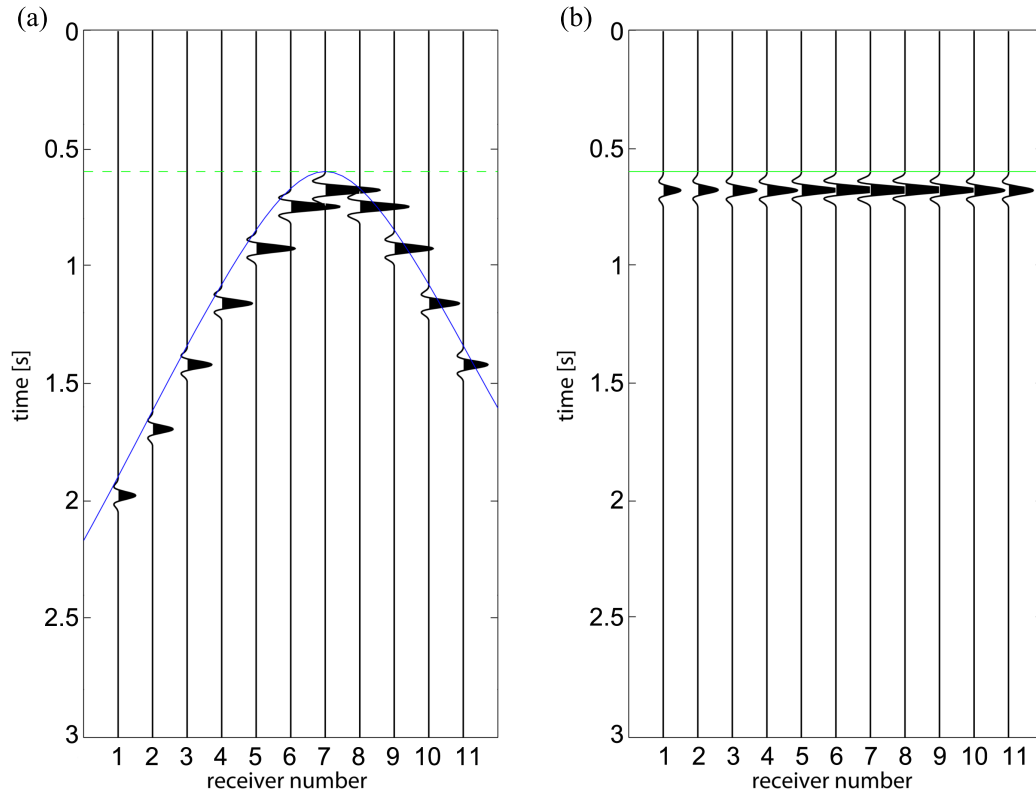


FIGURE 2.1: Simulated seismograms in a homogeneous model (a) before and (b) after static moveout shift. For the consistent velocity model and the correct location, the event in the data is flat after static moveout correction

Finally, all cross-correlation results are stacked over all receivers, thus leading to the amplitude assigned to the image point under consideration. Repeating the procedure for all image points provides the image function or section. The maximum of the stacked energy corresponds to the source location. Figure 2.2 demonstrates the concept of the cross-correlation stacking procedure in a homogeneous model. In Figure 2.2(a) input seismograms are shown, Figure 2.2(b) shows seismograms after static moveout shift for the false source position, and the result of zero-lag cross-correlation is shown in Figure 2.2(c), before collapse the time axis. In this case some amplitudes are stacked. Figure 2.2(d) represents seismograms after static moveout shift for the true source position, whereas in Figure 2.2(e) the result of zero-lag cross-correlation is shown, before collapse the time axis. There is a perfect match of the traveltime curve and the event, which leads to the greatest contribution for the image function.

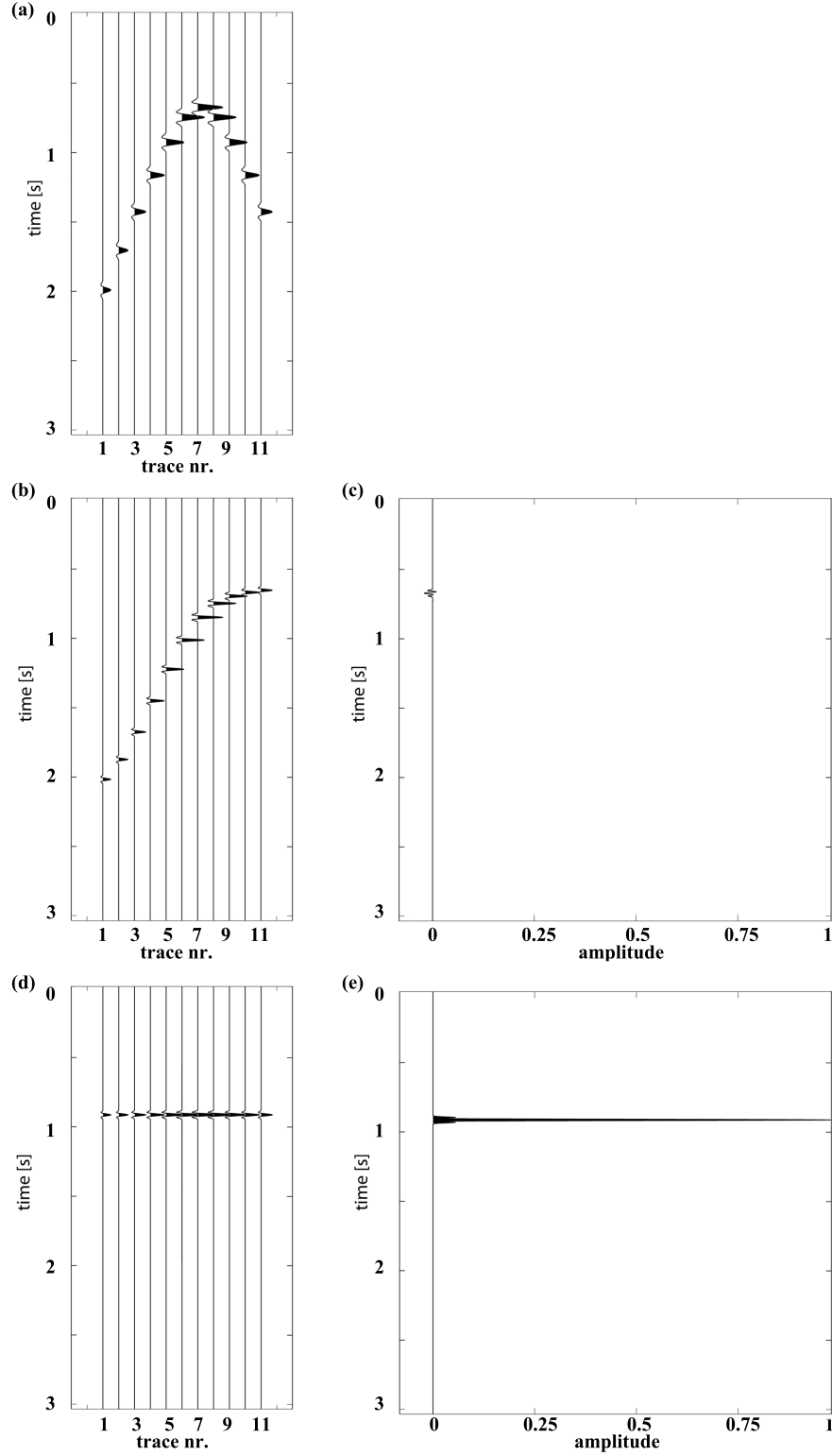


FIGURE 2.2: The concept of the cross-correlation stacking procedure in a homogeneous model. (a) Input seismograms are shown (b) Seismograms are shown after static moveout shift for the false source position, and (c) represents the result of cross-correlation procedure before collapse the time axis. In this case some amplitudes are stack. (d) Seismograms are shown after static moveout shift for the true source position, whereas in (e) the result of cross-correlation is shown. The amplitudes are normalised. There is a perfect match of the traveltime curve and the event, which leads to the greatest contribution for the image function.

The advantage of this method is that problem with the different polarities can be solved by cross-correlation stacking. Since zero-lag cross-correlation is a simple multiplication, in case of a source type with different polarities, It would not result to a low or zero value at the source position. More details about the procedure are given in the following sections.

## 2.2 Traveltime computation

The key observation of this section is the seismic signal's transit time. Physical properties of the media i.e. velocity or attenuation can be deduced from systematic observations of the arrival times. There are a variety of ways to compute the transit times of seismic wave propagation. Generally, more complicated media require more expensive and involved schemes to find the transit time.

### 2.2.1 Finite difference solution of the Eikonal equation

Through the past few decades, the growing need for the fast and accurate prediction of traveltime in complex media has generated various grid and ray based solvers. Grid based solutions, usually involve the calculation of traveltimes to all regular grid points. These methods represent numerical relations of Eikonal equation. They became increasingly popular for being computationally efficient and highly robust. They are often based on finite difference solutions of the Eikonal equation [Popovici and Sethian, 2002; Rawlinson et al., 2007; Vidale, 1988]. A particular solution of the Eikonal equation using finite differences was proposed by Vidale [1988]. The technique is presented for solving the Eikonal equation for inhomogeneous, isotropic media. An expanding wavefront scheme on a rectangular mesh of points is employed, in order to ensure causality and minimise grid anisotropy. In this method wave fronts propagate radially outward from a point source using each grid point as a secondary source for each successive grid point. The Eikonal equation, in 3-D, is given in the form of

$$\nabla\tau^2 = \frac{1}{V^2(x_i)}, x_i \in \mathbb{R}^3 \quad (2.1)$$

where  $\tau$  is the traveltime,  $v$  a given velocity field. This nonlinear problem is the first order hyperbolic partial differential equation. The energy propagates through a gridded media from the boundary. Due to the non-linearity, media may intersect like the formation of stress in hyperbolic conservation law. The solution is still continuous at these intersections but may not be differentiable. It is fundamental in many applications including computer vision [Bruss, 1982], path planing (e.g. computation of radio-wave attenuation in the atmosphere), image processing [Malladi and Sethian, 1996], and many more.

There are mainly two approaches to solve the Eikonal equation. The Eikonal equation transformation to a time dependent problem is the first approach. A semi-Lagrangian purpose, in the control framework, is obtained for Hamilton-Jacobi equations by discretising the dynamic programming principle in time [Falcone and Ferretti, 1994; Zhao, 2004]. However, many time steps may be needed for the convergence of the solution in the entire domain due to finite speed of propagation for time stability. The second approach is a stationary boundary value problem. The system solution for nonlinear equations after discretisation would include designing an efficient numerical algorithm [Zhao, 2004]. The fast marching is of this type [Helmsen et al., 1996]. The purpose solution, in the fast marching method, follows the causality of a consecutive way. I.e., the solution updates grid point by grid point in the order of increasing solution.

A major advantage of the method, is that the traveltimes are directly calculated for a grid of points. Therefore, no subsequent interpolation is required. Although in case that receiver positions does not coincide with the grid points, interpolation would be required. In contrast interpolation of the calculated traveltimes by ray tracing is essential. Because of its iterative nature, ray tracing through complex models can be expensive and cumbersome. Nevertheless, the combination of the later arrivals makes Eikonal equation a viable alternative to ray tracing. The disability to compute later arrival traveltimes and a lower accuracy compared to ray tracing are disadvantages of finite difference Eikonal solvers. Moreover, it is difficult to compute quantities other than traveltimes without first extracting the ray paths.

### 2.2.2 Fast sweeping solution of the Eikonal equation

A solution of the Eikonal equation based on fast sweeping is suggested by Zhao [2004]. It is an efficient iterative method for stationary Hamilton Jacobi equations. It relies on natural ordering provided by a rectangular mesh. In this method, each sweeping order follows the series of characteristics of the corresponding Eikonal equation in a certain direction of a rectangular grid simultaneously. The main idea of the fast sweeping method is to use a Godunov upwind differencing scheme and Gauss-Seidel iterations with alternating sweeping order on the interior nodes [Zhao, 2004]. Figure 2.3 illustrates the hypothetical distance function calculation from a point source at centre through the fast sweeping procedure ordering 1. Nodes with red dots indicate an updated solution. This illustrates that each ordering corresponds to a class of characteristic curves. It can be seen that ordering scheme 1 propagates information along the arrow or first quadrant characteristics into the entire shaded (upper right) region [Detrixhe et al., 2013].

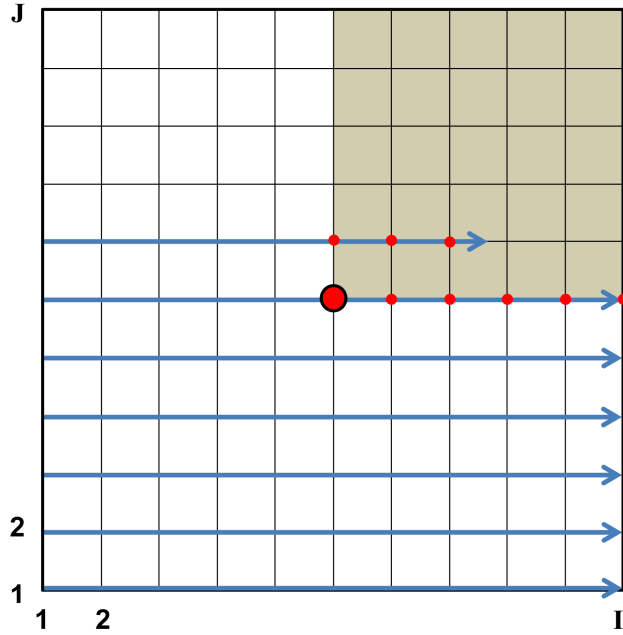


FIGURE 2.3: A snapshot of the calculation midway through the fast sweeping procedure ordering 1. Nodes with red dots indicate an updated solution. This illustrates that each ordering corresponds to a class of characteristic curves. It can be seen that ordering scheme 1 propagates information along the  $\nearrow$  or first quadrant characteristics into the entire shaded (upper right) region [Detrixhe et al., 2013].

### 2.2.3 Ray tracing

Instead of directly solve the Eikonal equation, its characteristics can be considered, which are the trajectories to the wavefront. The traveltime determination in a media smoothly varying can be performed by ray tracing. In physics ray tracing is a method to determine the wave path through a medium with varying velocities, and reflecting at interfaces. Heterogeneities result into bending or changing the direction of the rays, or reflection at interfaces, which leads to a complicated ray path [Červený, 2001]. This approach is often highly efficient and accurate, and therefore leads to the prediction of various seismic wave properties [Julian and Gubbins, 1977; Rawlinson et al., 2007]. Disadvantages of ray tracing include its complicated implementation. It may fail to converge to a two-point path. Moreover ray theory is applicable in smoothly varying media. This usually requires to smooth the velocity model such that the variations are small in dimension compared to the dominating wave length of the signal [Červený, 2001].



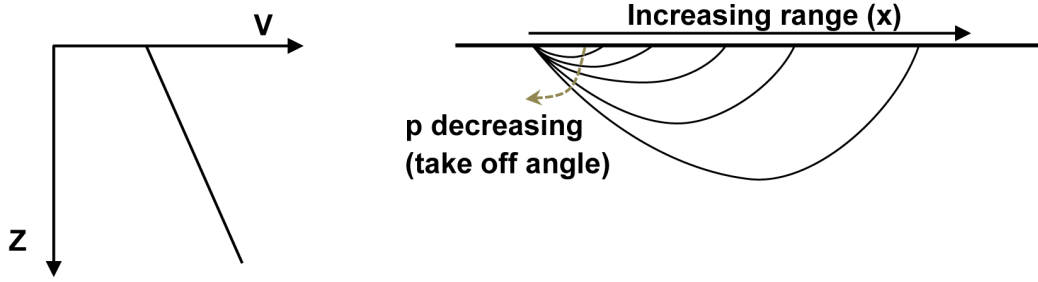


FIGURE 2.4: Schematic view of ray propagation in a media of gradually increasing velocity with depth. In general, the offset increases as take off angle decreases [Aster, 2011].

According to Snell's Law, when seismic rays propagate through a laterally homogeneous Earth where the velocity increases with depth when travelling deeper, they will be bent towards the horizontal (see Figure 2.4). In case  $r$  represents the position vector of a point on a wavefront, and  $l$  the path length of the curve traced out by this point as the wavefront evolves

$$\frac{dr}{dl} = \frac{\nabla\tau}{s} \quad (2.2)$$

Since both sides are unit vectors parallel to the path, slowness  $s$  represents the rate of change of traveltime  $\tau$  along the path

$$s = \frac{d\tau}{dl} \quad (2.3)$$

and by taking the gradient of both sides, Equation 2.2 and 2.3 can be combined as the kinematic ray equation

$$\frac{d}{dl} \left[ s \frac{dr}{dl} \right] = \nabla s \quad (2.4)$$

which describes the trajectory of ray paths in smoothly varying isotropic media. In isotropic media, the Hamiltonian is often written as [Rawlinson et al., 2007]

$$\mathcal{H}(x, p) = \frac{1}{2}[p^2 - s^2] \quad (2.5)$$

where  $p = \nabla\tau$ . In case of a Hamiltonian  $\mathcal{H} = 0$  the characteristics can be satisfy the Eikonal equation. The Hamiltonian equations which describe the characteristics can be written as

$$\frac{dx}{d\tau} = \frac{\partial\mathcal{H}}{\partial p} \quad \text{and} \quad \frac{dp}{d\tau} = -\nabla\mathcal{H} \quad (2.6)$$

These equations can be integrated forward in time from given initial conditions using standard numerical solvers such as the Runge Kutta method [Rawlinson et al., 2007]. Analytic ray tracing is possible for a few special cases. It usually requires to solve Equation 2.2 by reducing it to a convenient first order initial value system of equations. Using an eigenvalue of the Eikonal equation leads to the following kinematic ray tracing for the parameter  $\tau$

$$v_i = \frac{dx_i}{d\tau} = a_{ijkl} p_l g_j g_k \quad \text{and} \quad \frac{dp_i}{d\tau} = -\frac{i}{2} a_{nijkl,i} p_n p_l g_j g_k \quad (2.7)$$

where  $v_i$  is the  $i$ -th component of group velocity vector. Considering  $ds/d\tau = v$ , the kinematic ray tracing system for the parameter  $s$  results to

$$\frac{dx_i}{ds} = \frac{1}{v} a_{ijkl} p_l g_j g_k \quad \text{and} \quad \frac{dp_i}{ds} = -\frac{i}{2v} a_{nijkl,i} p_n p_l g_j g_k \quad (2.8)$$

In isotropic media, the system can be reduced to

$$\frac{dx_i}{d\tau} = V^2 p_i \quad , \quad \frac{dp_i}{d\tau} = -\frac{1}{V} \frac{\partial V}{\partial x_i} \quad (2.9)$$

$$\frac{dx_i}{ds} = V p_i \quad , \quad \frac{dp_i}{ds} = -\frac{1}{V^2} \frac{\partial V}{\partial x_i} \quad (2.10)$$

Kinematic ray tracing does not allow to compute the amplitudes. The amplitudes are inversely proportional to geometrical spreading. This limitation can be compensated by differentiating the kinematic ray tracing equations are obtained with respect to the ray parameters (i.e., dynamic ray tracing). Dynamic ray tracing allows to compute the ray Jacobian along one ray. Detailed information on ray tracing and transport equation can be found in, e.g. Červený [2001].

In this study both ray tracing and the Eikonal equation are used to compute traveltimes for the comparison of the localisation results. The NORSAR ray tracing is used to compute the traveltimes of first and most energetic arrivals. In this program package the ray tracing equation is solved using a Taylor expansion or 4th order Runge-Kutta method. The Taylor method is faster whereas the 4th order Runge-Kutta method is more accurate. In this study, 4th order Runge-Kutta method is considered to solve the ray tracing equation.

## 2.3 Static moveout correction

To increase trace coherency, I apply simple static moveout shift (SMO) before cross-correlation. As soon as the traveltimes for each image point are available, a SMO is

performed to prepare the data for correlation and stacking. As mentioned before, the minimum time of the traveltime curve represents the apex time  $\tau_0$ . The apex location in a heterogeneous medium generally does not coincide with the lateral position of the image point under consideration. The static moveout  $\tau_{SMO}^i$  is the time difference in the seismic section between the one-way traveltime  $\tau^i$  at a receiver located on the surface  $(x_i, y_i, 0)$  from the apex location  $(x_{apex}, y_{apex}, 0)$  with the minimum traveltime  $\tau_0$  along the aperture, measured between image point  $(x, y, z)$  and receiver located on the surface  $(x_i, y_i, 0)$  from the apex located at

$$\tau_{SMO}^i = \tau^i - \tau_0 \quad (2.11)$$

Where  $\tau_{SMO}$  is the static moveout for each image point  $P(x, y, z)$  in the model to a receiver located on the surface  $(x_i, y_i, 0)$ . The set of all static moveouts  $T_{SMO}$  for each image point  $P(x, y, z)$  in the model to all receivers  $[1, N]$  is defined by:

$$T_{SMO} = \{t_{SMO}^1, t_{SMO}^2, \dots, t_{SMO}^N\} \quad (2.12)$$

In the data this moveout is applied as a static time shift for each trace to align them to a common  $\tau_0$ . For a velocity model consistent with the data and a correct location of the image point, all events would be perfectly aligned within the time window.

## 2.4 Cross-correlation

In this step, the cross-correlation equation is used for two signals  $x(\tau)$  and  $y(\tau)$ , each one with finite energy, which is defined as [Shearer, 2009]:

$$r_{xy}(t) = \int_{t_1}^{t_2} x(\tau - t)y(\tau)d\tau \quad (2.13)$$

where the parameter  $t$  is the (time) shift (or lag),  $t$  is the time sample at the selected time interval  $[t_1, t_2]$  and  $r_{xy}(t)$  yields the cross-correlation coefficient at time lag  $t$ . In this study, a zero-lag cross-correlation is applied to data, i.e. traces are just multiplied sample wise and the products are summed.

A critical issue is the choice of the master trace in the correlation process. One may consider the trace with the best SNR as master trace, which may require additional processing steps. Alternatively, each trace can be chosen as master trace and to stack all correlation results over each image point. If there are  $N$  traces in the data,  $N \times N$  correlations are obtained. This brute force approach will be independent of the master trace but is computationally challenging. Another option for imaging could be the

pairwise cross-correlation. It directly multiplies two traces next to each other. It is intuitive that using pairwise cross-correlation for each time sample, instead of considering each trace as master trace, decreases the computational costs significantly. Although it may result in lower image resolution, it solves the problem of source radiation patterns with polarity changes [Zhebel, 2013]. Throughout this study, each trace is considered as master trace.

Regarding the Equation 2.13, image values  $E_i(x, y, z)$  at every grid point  $P(x, y, z)$  of the model are obtained by the coherent energy of the time interval for  $i$ th trace as master trace,

$$E_i(x, y, z) = \sum_{t=t_1}^{t_2} a_i(t + \tau_{SMO}(i))A(t + T_{SMO}) \quad (2.14)$$

$a_i(t)$  corresponds to the amplitudes of  $i$ th trace as master trace and  $A(t)$  corresponds to the matrix of amplitudes of all the traces.

## 2.5 Stacking

To increase the SNR and to avoid a particular choice of the master trace, the amplitudes of all correlation results for all offsets and master traces are stacked for each image point in this step. This result corresponds to the amplitude of the image point. The Equation 2.13, can be expanded to

$$E_i(x, y, z) = \sum_{t=t_1}^{t_2} \sum_{j=1}^N a_i(t + \tau_{SMO}(i))a_j(t + \tau_{SMO}(j)) \quad (2.15)$$

where  $j$  marks the number of trace in correlation. Finally a stack over all image values of the previously selected time interval  $[t_1, t_2]$  and over all receivers  $[1, N]$  provides the final image of the localisation.

$$M(x, y, z) = \sum_{i=1}^N E_i(x, y, z, t) \quad (2.16)$$

The summation over all receivers yields regions of distinct stacked energy. Thus, the image point in the final image  $M(x, y, z)$  with maximum stacked energy is assumed to represent the source location.

## 2.6 Localisation with Three component measurements

For elastic media, the described above can be applied to both horizontal and vertical components of the data. In theory, three components' contributions of recordings could give reasonable estimation of tremor depths. This issue has been a highly debated since the discovery of tremors. In the simplest case, the stacking images obtained from vertical and horizontal components can provide the final amplitude of the image point in this case.

$$M(x, y, z) = \sum_{\text{component}} M_{\text{component}}(x, y, z) \quad (2.17)$$

Another option is the normalisation of the image obtained from the horizontal component (horizontal image) with the image obtained from vertical component (vertical image) to get the final value of the image point. Throughout this study this imaging condition is referred to as “scaled horizontal to vertical” images.

$$M(x, y, z) = \frac{\sqrt{M_{H1}(x, y, z)^2 + M_{H2}(x, y, z)^2}}{M_V(x, y, z)} \quad (2.18)$$

where  $M_{H1}$  and  $M_{H2}$  are the localisation images obtained from horizontal component seismograms in x and y-directions.  $M_V$  represents the localisation images by considering vertical component seismograms.

Figure 2.5 shows a typical structure of the subsurface comprising a hard bedrock and a soft soil. Horizontal and vertical displacements do not change throughout the bedrock. Whereas wave propagation through the soft soil results in increase of the amplitude of the displacement horizontally in general and slightly in vertical direction on the surface at receiver position [Nakamura, 1989].

In the soft soil, horizontal motion is larger than vertical motion. In the hard ground, both horizontal and vertical motions are similar to each other in both the maximum value and waveform. In tremors studies horizontal component is considered as horizontal motion of vertical incidence of S-waves whereas vertical component represents the vertical motion of vertical incidence of P-waves [Nakamura, 2008]. During the ray's transition through the soft soil comprising the weathered layer and fluids horizontal component is more affected so I some how normalise the highly affected amplitudes during the propagation versus vertical component with minimal affect.

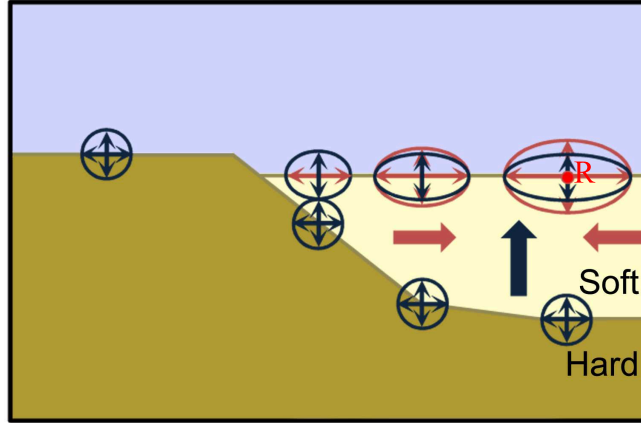


FIGURE 2.5: Illustration of H/V method [Nakamura, 2008].

It was hypothesised that the vertical component of the ambient seismic noise on the ground surface keeps the characteristics of basement. It is relatively influenced by Rayleigh wave on the sediments. Therefore it can be used to remove both of the source and the Rayleigh wave effects from the horizontal components. Based on the diffuse field theory, suggested by Sánchez-Sesma et al. [2011], the microtremors' H/V corresponds to the square root of the ratio of the imaginary part of horizontal displacement for a horizontally applied unit harmonic load and the imaginary part of vertical displacement for a vertically applied unit load. The same diffuse field concept leads us to derive a simple formula for body waves' H/V. That is, the ratio of the horizontal motion on the surface for a vertical incidence of S-wave divided by the vertical motion on the surface for a vertical incidence of P-wave with a fixed coefficient [Kawase et al., 2011].

In this study, I considered stacked horizontal and vertical image and scaled horizontal to vertical image as the final image. I have compared the results of both imaging condition to vertical image. It is important to note that depending on the source type and contribution of S-Wave in the stacked energy, scaled horizontal to vertical images may provide a better result.

In the following chapter different source mechanisms will be considered. Next chapter is dealing with imaging conditions at homogeneous and heterogeneous media.

## Chapter 3

# Application to synthetic data

Seismic event location is an inherently 3-D problem. Despite this fact 2-D synthetic examples are considered in this chapter to illustrate the method and to study its performance. The 2-D numerical examples serve as a feasibility study for verification purposes and to discuss advantages and disadvantages. Homogeneous and heterogeneous models are considered. Point source data of short duration and microtremor events are considered. Since the latter are considerably lower in frequency content than acoustic emissions this issue needs special attention for complex media.

### 3.1 Homogeneous medium

Prior to the application of the method to complex models it is essential to define the concept of the cross-correlation approach. On a generic example a sparse network of receivers is considered. A 2-D homogeneous medium is assumed with a P-wave velocity of 2500 m/s. Its the size is 9000 m in  $X$ -direction and 3000 m in  $Z$ -direction. The total number of receivers is 11 in  $X$  direction located at  $Z = 0$  with a spacing of 750 m starting from  $X = 750$  m. An explosive source is set at (5250, 1500) m, i.e. the acquisition is not symmetrical with respect to the lateral position of the source. NORSAR-3D is used to compute P-wave traveltimes although analytical computations would be possible for this simple example. Figure 3.1 shows the image function of the cross-correlation stacking where different traces are considered as master traces for the correlation (i.e., 1st in Figure 3.1(a), 7th in Figure 3.1(b), 11th in Figure 3.1(c)). Figure 3.1(d) shows the stack of the correlations which each trace was used as master trace.

The colour scales indicate the absolute value of the image, to show the impact of the chosen master trace on the result. The maximum value of the image function coincides with the real source position.

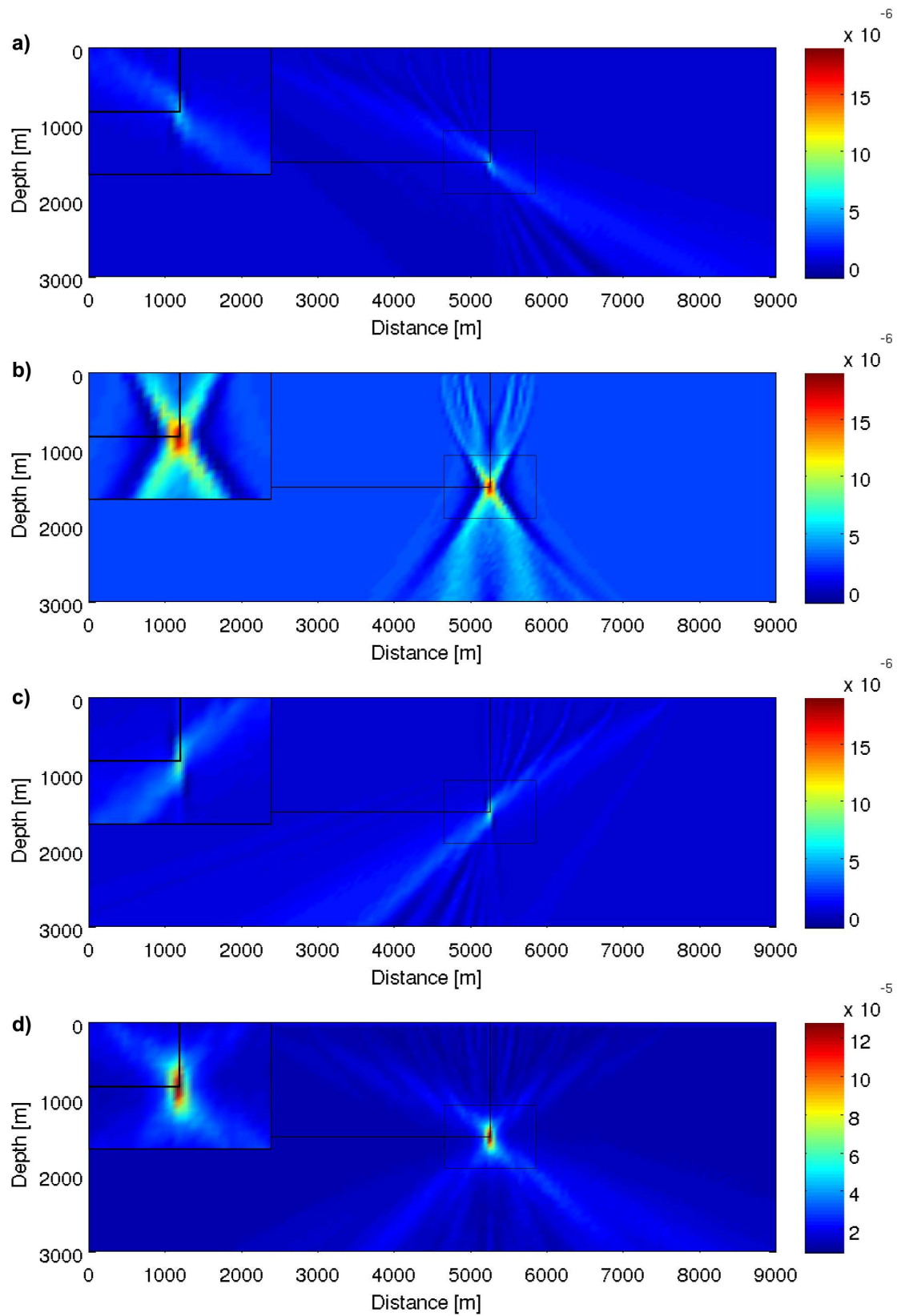


FIGURE 3.1: Localisation images of an explosive source in a homogeneous medium, using cross-correlation stacking obtained by (a) 1st, (b) 7th, (c) 11th trace of seismogram as master trace and (d) stacking over all images when each trace is considered as master trace.



Whereas the pattern of noise and the image seem dependent on the choice of master trace, the maximum value of the image function seems independent on the choice of the master trace. The stacking of all results removed this dependence and optimised the image function. The localisation procedure will work well in the presence of uncorrelated noise which may completely mask the actual signal. The potential to detect these events is raised by increasing the number of receivers in the observing network. However it is possible to locate the event also in a sparse network, the requirement on the data quality (i.e., the SNR) is higher in this case.

### 3.2 Traveltime error in homogeneous medium

The major issue of localisation's uncertainty is the errors in velocities which leads to errors in traveltimes and often results to unaddressed location in passive seismics [Eisner et al., 2009; Usher et al., 2013]. This section's objective is to improve the accuracy of seismic location determination, and reduce the uncertainty of the estimated locations. Here the improvement in the location performance is demonstrated using a time lag cross-correlation between normalised seismograms.

Location performance is tested on the synthetic data generated in a 2-D homogeneous medium with a P-wave velocity of 2500 m/s and the size of 9000 m in  $X$ -direction and 3000 m in  $Z$ -direction. The total number of receivers is 11 in  $X$  direction located at  $Z = 0$  with a spacing of 750 m starting from  $X = 750$  m. For simplicity, an explosive source is set at (5250, 1500) m, i.e. the acquisition is not symmetrical with respect to the lateral position of the source. The model and event are under control, as it is always the case in synthetic studies. For this simple model the correct traveltime determination is approved. Nevertheless, the traveltimes are determined by adding %5 error to the velocity model to test the performance of correction. As expected, the error in the velocity model causes incorrect approximation in the traveltime prediction and therefore leads to a shift in the focusing point. Figure 3.2 illustrates the traveltimes of incorrect and accurate models from a shot at (0, 5250) m to all image points location. Figure 3.3 shows the localisation image of the explosion source with considering a zero-lag and a time-lag cross-correlation stacking approach. The red line in Figure 3.3(a) indicates the high amplitudes of the image. Since valuable information are lost considering the incorrect moveout correction in localisation procedure. It led to a wrong localisation result. To overcome this limitation, I chose a 32 ms time lag in localisation procedure. The potential to improve the location increases with increasing the time lag in such a sparse network (see Figure 3.3(b)). Cross-correlation stacking results to a wall focused image, although the maximum value of the image occurs 50m deep compared to the actual depth of real source.

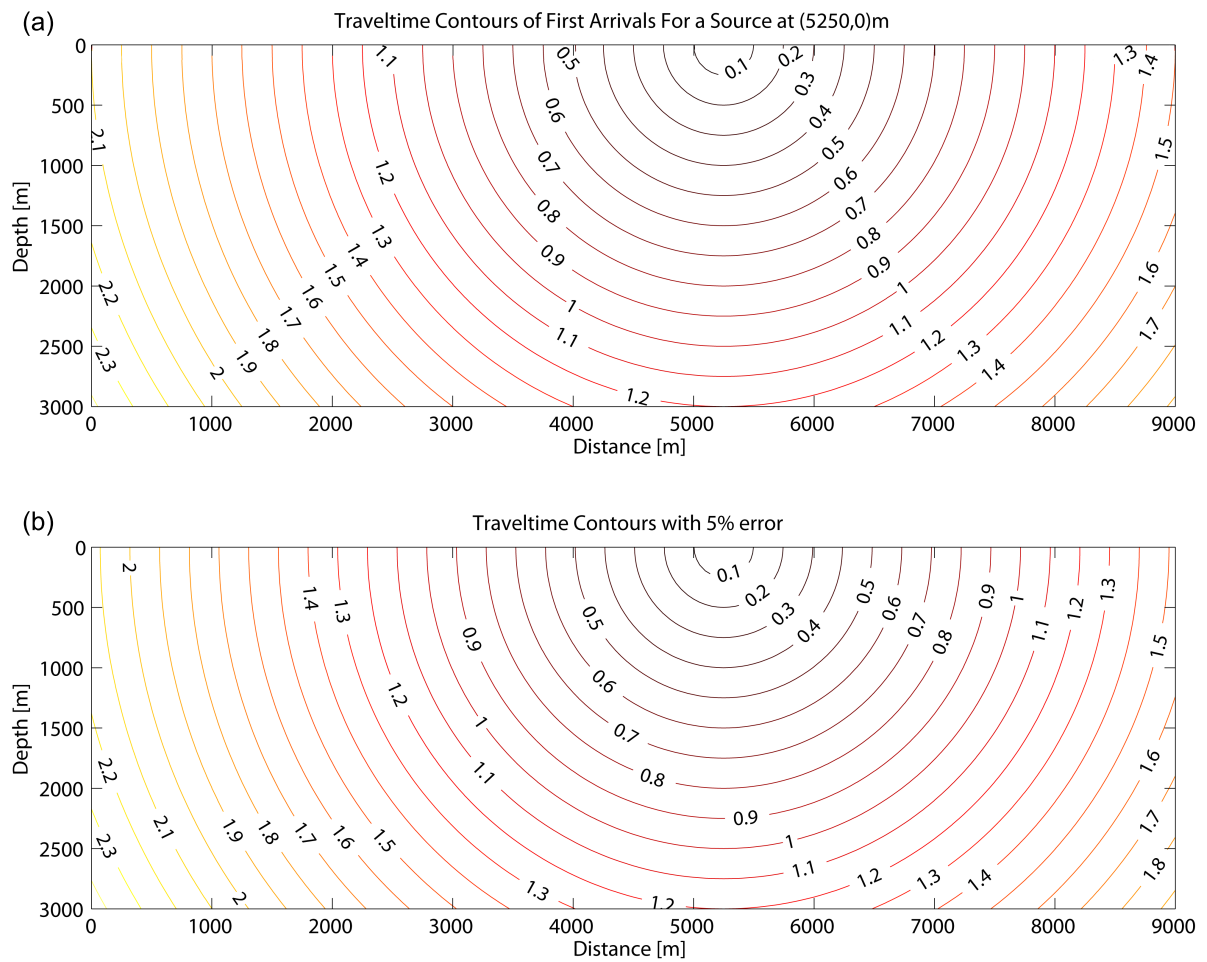


FIGURE 3.2: Comparison of the traveltimes contours: (a) the correct traveltimes and (b) incorrect traveltimes for a shot set at (5250, 0)m.

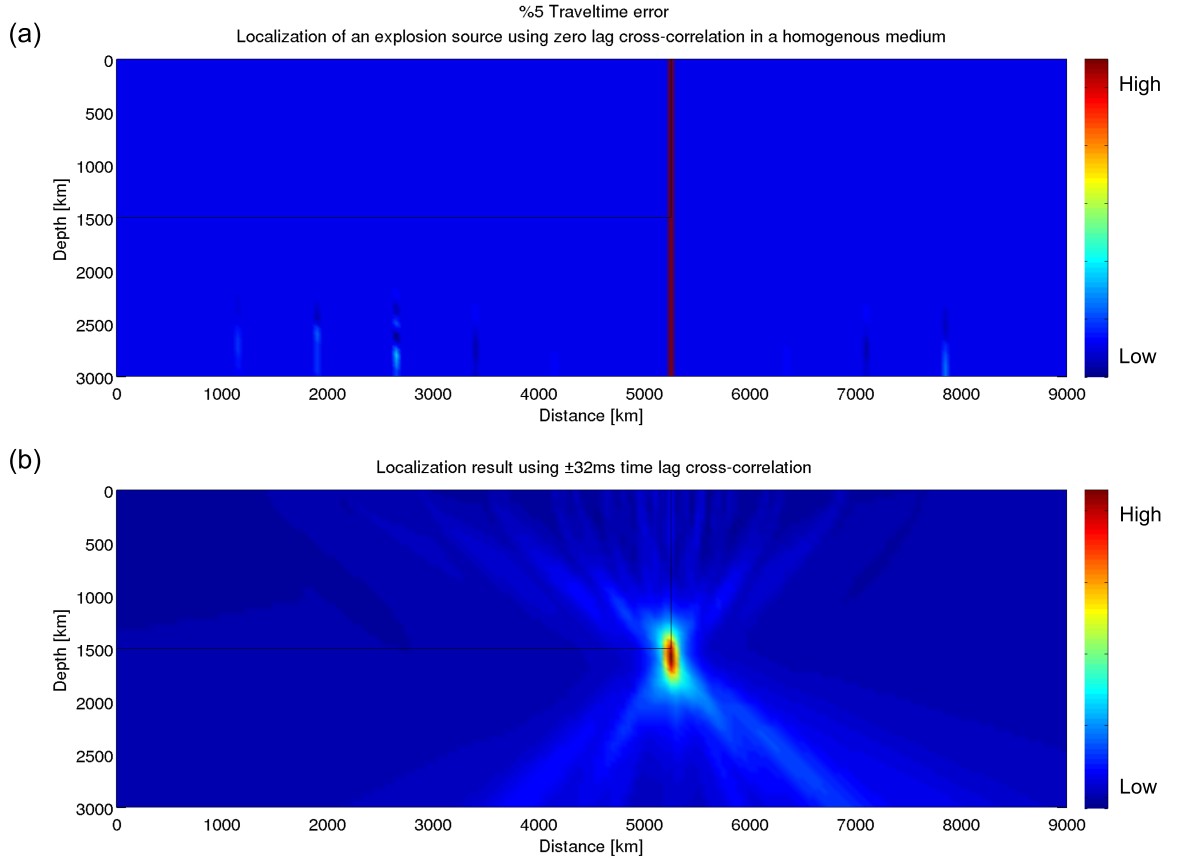


FIGURE 3.3: Localisation of an explosive source simulated by a Ricker wavelet with a central frequency of 10 Hz in homogeneous medium. (a) a zero time lag, and (b) 24 ms time lag cross-correlation is applied in the localisation procedure. The intersection of black lines indicates the real source location

### 3.3 Heterogeneous medium

Here a complex heterogeneous velocity model constructed by [Steiner \[2009\]](#) is considered. This model consists of ten sedimentary layers with P-wave velocities between 1200 to 3000 m/s above a crystalline basement with the P-wave velocity of 6000 m/s. The black contour around a 50 m thick and 2000 m wide area represents a reservoir. The total number of receivers is 11 in  $X$ -direction, located at  $Z = 0$  with a spacing of 750 m, starting from  $X = 750$  m (see Figure 3.4).

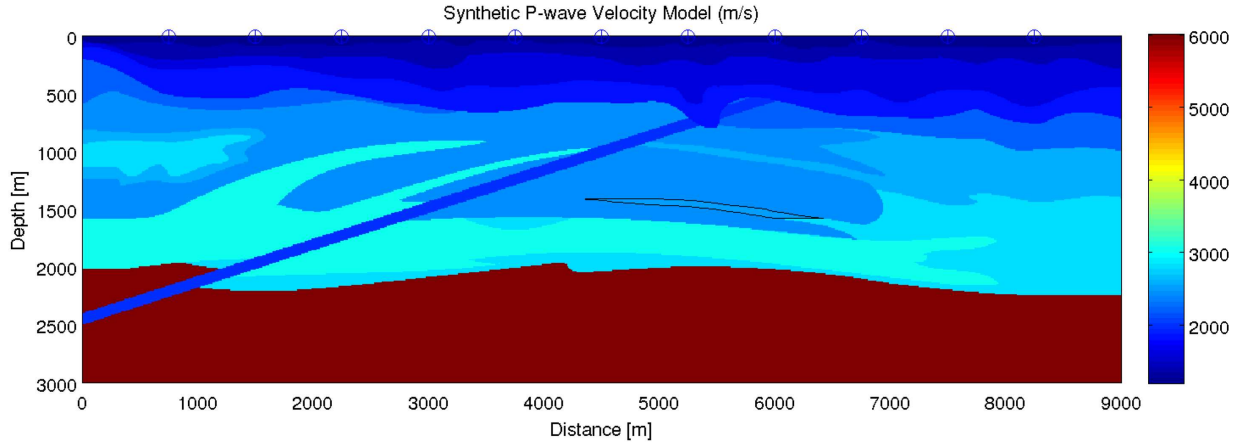


FIGURE 3.4: The synthetic heterogeneous velocity model consists of ten sedimentary layers above a basement unit. A thin area representing the reservoir defines the seismic source region of microtremor signals. The blue circles represent the position of seismometers on the surface. The colour scale on the right shows the P wave velocity [Steiner, 2009].

### 3.4 Localisation in a blocky velocity model

First the model is considered as displayed in Figure 3.4. This does not allow the application of ray tracing. Therefore a finite difference solver of Eikonal equation [Vidale, 1988] was used to generate traveltimes for each image point to the 11 receiver positions. Eikonal equation generates the traveltimes of first arrivals. To illustrate the impact of different source types in localisation, three numerical simulations with different source mechanism are considered to generate seismograms. Two point sources with different prevailing frequencies and one microtremor event.

#### 3.4.1 Point source

The synthetic data was generated for a point source at  $X = 5000$  m and  $Z = 1500$  m. For the elastic modelling of wave-fields a pseudo spectral modelling method [Tessmer, 2000] with a time step of 0.5 ms was used. Wave-fields up to a total time of 4 s were computed. The vertical components of Seismograms are shown in Figure 3.5 where two different prevailing frequencies of the signal are considered to generate the seismograms, corresponding to high and low frequency point sources. A Ricker signal is used as a source time function. This signal has a short duration in time, i.e. it resembles the shape of an elastic emission. A signal with the central frequency of 60 Hz represents

the spectral content of an elastic emission observed at the surface. A signal with the central frequency of 4.5 Hz represents the spectral content of a microtremor signal. The prevailing frequencies in the considered events are about half of the main frequency. The P-wave traveltimes of the first arrivals is also displayed in the seismogram sections.

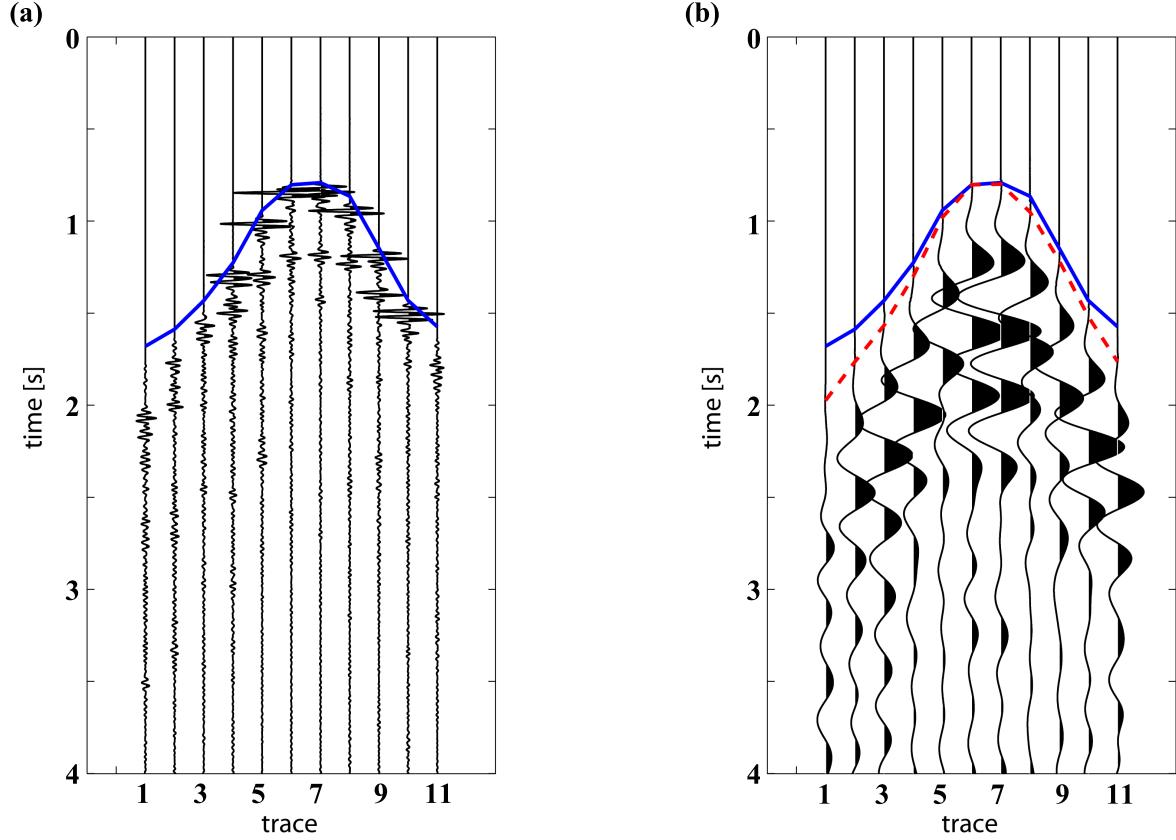


FIGURE 3.5: Vertical component seismograms in a heterogeneous model (a) Ricker wavelet with central frequency of 60 Hz representing a high frequency signal, (b) Ricker wavelet with central frequency of 4.5 Hz representing a low frequency signal [Tessmer, 2000]. Blue curves indicate the FD Eikonal traveltimes corresponding to high frequency event and dashed curve in red represents the traveltimes fitted to low frequency event.

The visual appearance of the data is quite different due to the different interferences for the high and low frequency data. The apparent time delay of the low frequency event compared to the high frequency event will not affect the localisation process. However, its different moveout compared to the high frequency event will influence the localisation. Traveltimes computed by FD Eikonal solvers always represent the arrival times of high frequency events.

The cross-correlation stacking approach is applied by using first arrival traveltimes provided by FD Eikonal solver to localise the point source events. Results of the localisation of the high frequency (60 Hz central frequency) and low frequency (4.5 Hz central frequency) event for the heterogeneous velocity model are shown in Figure 3.6 and Figure 3.7. The localisation was applied both to the horizontal and vertical component of the particle velocity separately and then stacked to obtain the image function. In general the localisation images, presented in this study, are normalised. This means they do not depend on the absolute amplitudes. The maximum of the image function is close to the exact source location. However, high amplitude scattering is also observed. I observed a strong false maximum which may be considered as source. This can be explained by sparse though acquisition. In case of having more receivers, the noise would likely be decreased and loose imaging artefacts would be presented (e.g. the migration apertures are visible).

The maximum of the image function for the low frequency event is shifted 100 m upward with respect to the actual source location. It can be observed that the localisation image pattern in complex media displays the frequency dependence. Whereas for high frequency signals a good localisation result was obtained, a location error was observed for the low frequency signal. The computed traveltimes describe the arrival times of high frequency events. This might explain the reduced localisation performance for the low frequency signal. This conclusion may impact the localisation of microtremor events in complex media since these events are of low spectral content.

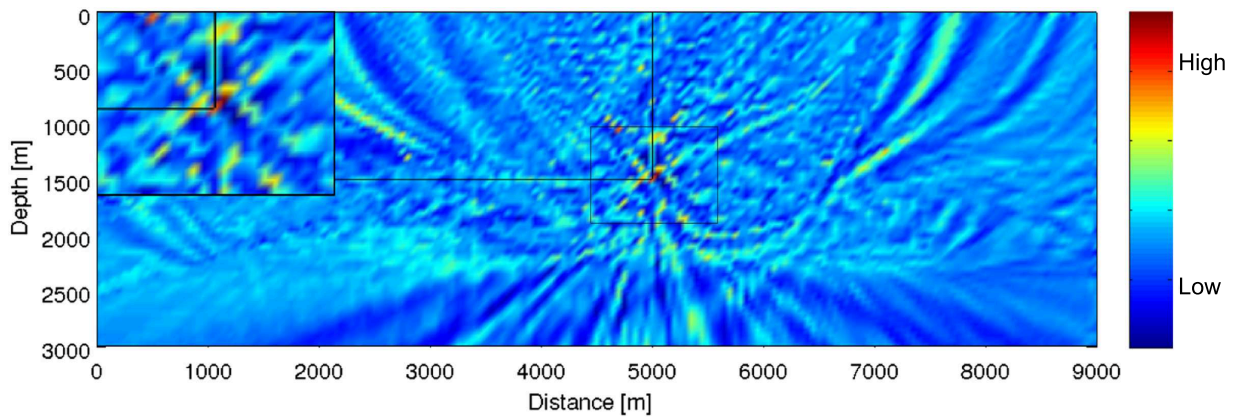


FIGURE 3.6: Localisation of a high frequency point source event simulated by a Ricker wavelet with a central frequency of 60 Hz in heterogeneous media. Stacking over the results of the horizontal and vertical components are shown. The colour scale on the right shows the relative value of the amplitude of the image function. The maximum of the image function is close to the exact source location.

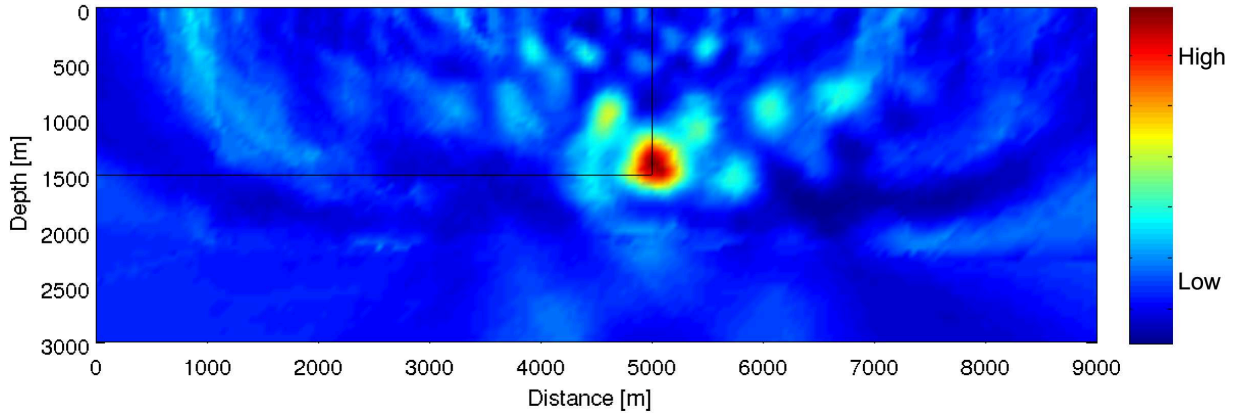


FIGURE 3.7: Localisation of a low frequency point source event simulated by a Ricker wavelet with a central frequency of 4.5 Hz in heterogeneous media. Stacking over the results of the horizontal and vertical components are shown.

### 3.4.2 Microtremors simulated by explosion source

Microtremors are low frequency seismic signals of the Earth which have a long duration in time. Microtremor observations above some reservoirs display remarkably similar spectral characteristics to each other. These observations point out to a common source mechanism, although the depth, fluid content (oil, gas or gas condensate of different compositions and combinations) and reservoir rock type (such as sandstone, carbonates, etc.) for each of the sites are quite different [Steiner, 2009].

The synthetic microtremor data I used here was generated by Steiner et al. [2008]. They used a two-dimensional finite difference (FD) simulation of elastic wave propagation from random point sources in the reservoir area (indicated by the black line in Figure 3.4). Continuous microtremors are simulated by applying 574 low-frequency point sources with a prevailing frequencies ranging between 1.5 Hz and 4.5 Hz. These sources are arbitrarily spaced within the area representing the reservoir. The source times are randomly distributed in a 180 second time window used for the numerical simulation. The resulting signal simulates a microtremor which has a spectrum similar to natural microtremors. The source type used in this section corresponds to explosive sources. P-waves are simulated by adding values to the normal stresses in the stress equations. The horizontal and vertical particle velocities are recorded by 11 vertical seismometers at the model surface (see Figure 3.4).

The elastic model corresponds to the model shown in Figure 3.4. In Figure 3.8 a localisation result is displayed for the heterogeneous velocity model. First arrival traveltimes



computed by a FD Eikonal solver were used to localise the microtremor event. High amplitudes with a lateral extension similar to the reservoir width are observed. However, the high amplitudes occur above the reservoir area. The white star in the image indicate the largest amplitude of the image. However, the high amplitude area appears too high compared to the actual depth of the source area. Also the image point with the largest amplitude is observed high above the actual reservoir depth.

Again this could be an effect of the low frequency content in the data, whereas the computed traveltimes correspond to high frequency events. Moreover, FD Eikonal solver models first arrivals which often have very small amplitudes. In addition to these facts, another complication in heterogeneous media may complicate the localisation process: triplications in the traveltime curve. Triplications are very diagnostic of the presence of a steep velocity increase or a discontinuity [Shearer, 2009]. This can lead to complex interference patterns between first and later arrivals, particularly for low frequency signals. Later arrivals can be computed by ray tracing which however requires smoothing of the complex model.

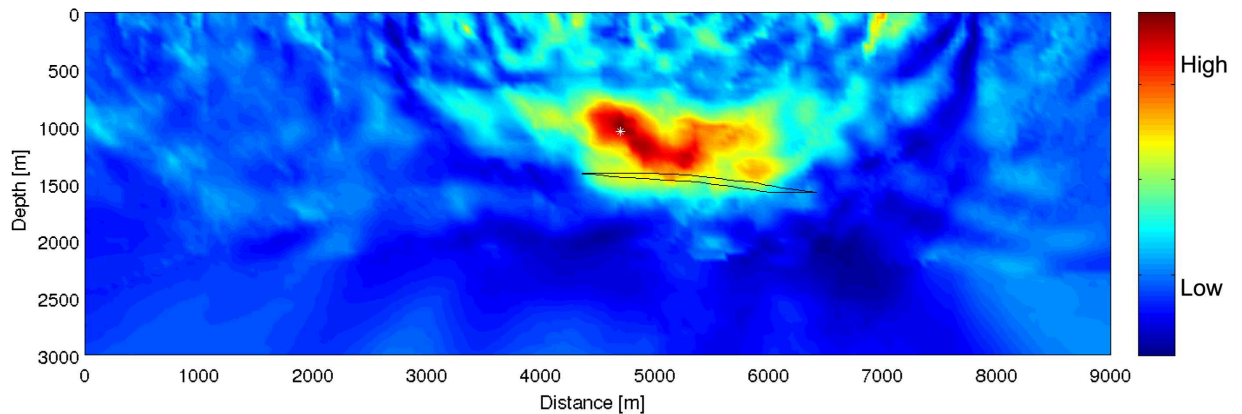


FIGURE 3.8: Localisation image of a synthetic microtremor signal, simulated by explosion sources in the reservoir area, in heterogeneous media. Stacks over the results of horizontal and vertical components are shown. First arrivals were used. The white star indicates the maximum of the image function.

### 3.5 Smoothing the velocity model

In complex media, prediction of traveltime is a challenging issue, that can be achieved by ray theory. The foundation of ray tracing techniques is based on the high frequency assumption of the wave equation. Therefore, modelling of seismic signals by ray tracing is possible whenever the spatial variations of velocity and its derivatives are small



with respect to the wavelength of the signal under consideration [Gajewski et al., 2002]. Appropriate smoothing is determined by optimising the scattering of the rays and distorting the structure of the Earth model. Losing the accuracy of the velocity model may cause incorrect arrival times, and cause a spatial shift of a focusing point [Gray, 2000]. To compute the first and later arrival times, it is required to apply ray tracing. Therefore, slowly varying interfaces and property fields are required. Thus, the velocity model needs to be smoothed (filtered) to handle complex velocity models.

In this study a 1-D Hamming operator is running over the velocity model with 200 and 500 m extension which is applied to each dimension of the model. It is applied repeatedly in each direction until each grid point affects the neighbourhood defined by extension. However, the effective size of the Hamming filter will be smaller. Figure 3.4 shows a complex velocity model simulated by Steiner [2009]. The smoothing with the 200 m window preserves most of the velocity features of the original model (Figure 3.9).

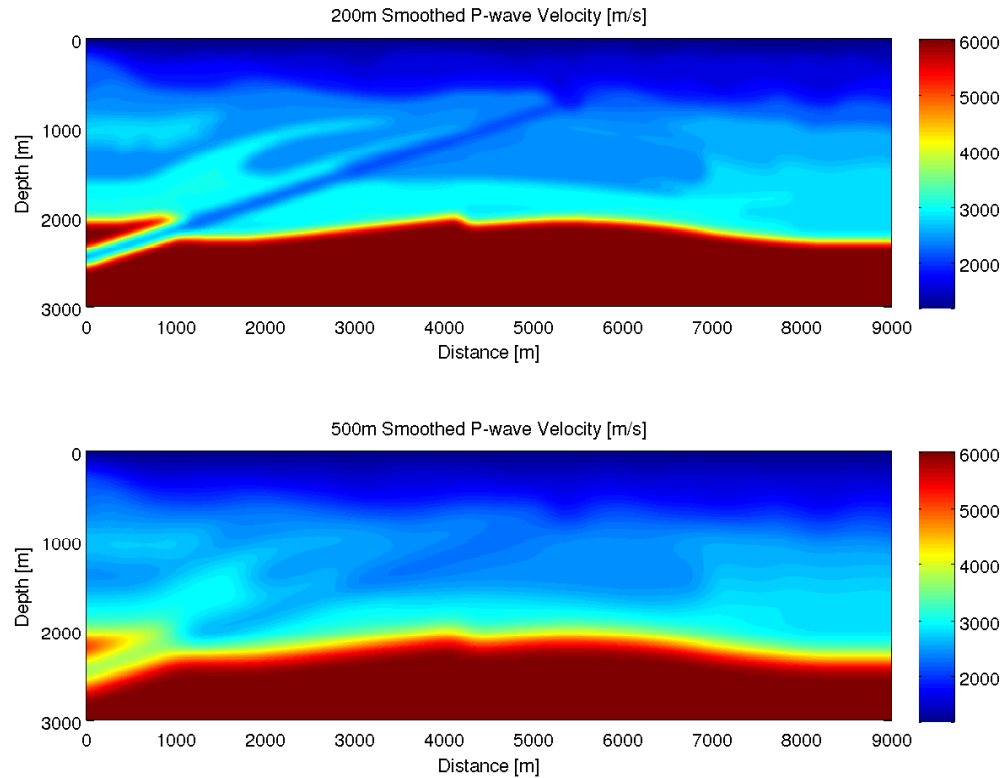


FIGURE 3.9: Smoothed velocity models using a Hamming window of (a) 200 m, and (b) 500 m.

In contrast, the result of the 500 m window has lost some of the prominent features. The Hamming window  $h_l$  in the 1-D time domain is defined by

$$h_l(x) = 0.54 - 0.46\cos\left(\frac{2\pi x}{N}\right) \quad , \quad 0 \leq x \leq N - 1 \quad (3.1)$$

where  $N$  represents the width, in samples, of a discrete-time, symmetrical window function  $h_l(x)$ . The Hamming window function is interesting since decision of the steepness of its slope is applicable in case of varying  $N$ . This property will help us to parametrise the penalty function in order to make constraints on the velocity field.

### 3.6 First and most energetic arrivals

The simplest Green's function representation assumes a single wavefield arrival from each source position, i.e. a single traveltimes, amplitude, and phase value at each point in the subsurface. This simplification of the Green's function may reduce the quality of the Kirchhoff migration image, since the heterogeneity of Earth structure means that multipathing commonly contributes to the complexity of a recorded waveform. Therefore having a scheme that can efficiently predict all arrivals of significant amplitude has important implications e.g. seismic imaging [Rawlinson et al., 2007]. When a complex velocity field causes multipathing, i.e., when several wavepaths connect a single source-receiver location at single depth location. In case of multipathing occurrences, the use of first-arrival Green's functions computed by finite-differencing the eikonal equation do not yield satisfactory images, as demonstrated by Geoltrain and Brac [1993]. This is because first arrivals tend to avoid regions of low wave speed, whereas most energetic arrivals, which do not necessarily exhibit such behaviour, could provide better path coverage and consequently result in improved imaging [Rawlinson et al., 2007].

In other words complex media with wavefront folding, generate complex propagation paths. This causes phase shifts and triplications. Triplications are very diagnostic of the presence of a steep velocity increase or discontinuity [Shearer, 2009]. Whereas the wavefield evolves, complex propagation effects begin to manifest themselves and the arrivals become multivalued, In this case, late energetic arrivals are not fit well by first-arrival finite-difference traveltimes and the first arrivals are associated to low energy events passing through the media [Červený, 2001]. Energetic events are migrated with the unrelated traveltimes of the fast first arrival and end up mispositioned at depth. First-arrival traveltimes follow the fastest branch of the triplication bow-tie, which is also the low energy branch.

Since the traveltimes of most energetic part of the wavefield (METT) dominates the data, computing the METT is recognised as an essential element in modern seismic

imaging techniques [Geoltrain and Brac, 1993]. The most energetic traveltimes are single-valued, but are discontinuous in general, and require the computation of the amplitudes of wavefronts.

In this study, traveltimes are computed for first and most energetic arrivals using the NORSAR ray tracing program package to compare their influence in imaging seismic sources. The first and most energetic arrival traveltime contours for a shot at  $X = 5250$  m and  $Z = 1500$  m in the smoothed velocity models are shown in Figure 3.10.

Particularly in the model with the 200 m Hamming window areas where later arrivals are the most energetic events are recognised. The difference in the first arrival traveltimes for the model with 200 m and 500 m smoothing window is not obvious. In this study the velocity model with the 500 m smoothing window is used in the localisation procedure to achieve the most stable ray tracing results. In the following section I provide the localisation results based on using first and most energetic arrival traveltimes.

### 3.7 Localisation in the smoothed velocity model

The heterogeneous model is considered as displayed in Figure 3.4. In order to apply ray tracing for the computation of first and later arrival traveltimes, the velocity model needs to be smoothed. Therefore a 1-D Hamming window with 500 m extension was applied to each dimension of the model. To illustrate the influence of different source types on localisation, two point sources with different prevailing frequencies are considered. In addition, three numerical simulations modelled by Steiner [2009] with different source mechanisms are considered to generate synthetic microtremors.

#### 3.7.1 Point source

Results for the localisation of high frequency (60 Hz central frequency) and low frequency (4.5 Hz central frequency) point source events of short duration in time in the smoothed velocity model are shown in Figure 3.11 and Figure 3.12.

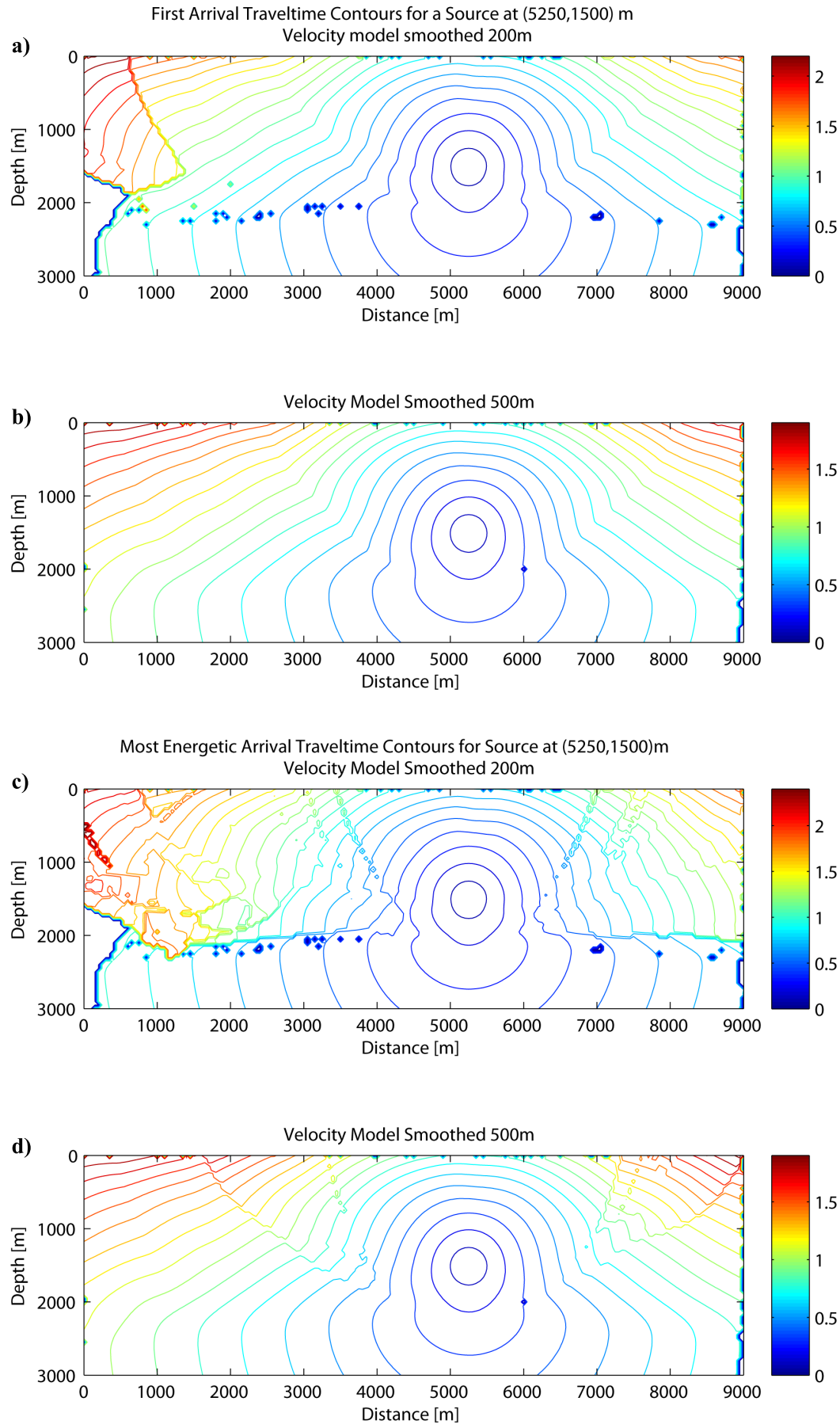


FIGURE 3.10: Traveltime contours of first arrivals computed for (a) 200 m, and (b) 500 m smoothed velocity model and most energetic arrivals for (c) 200 m, and (d) 500 m smoothed velocity models. The colour legend shows the traveltime values in s.

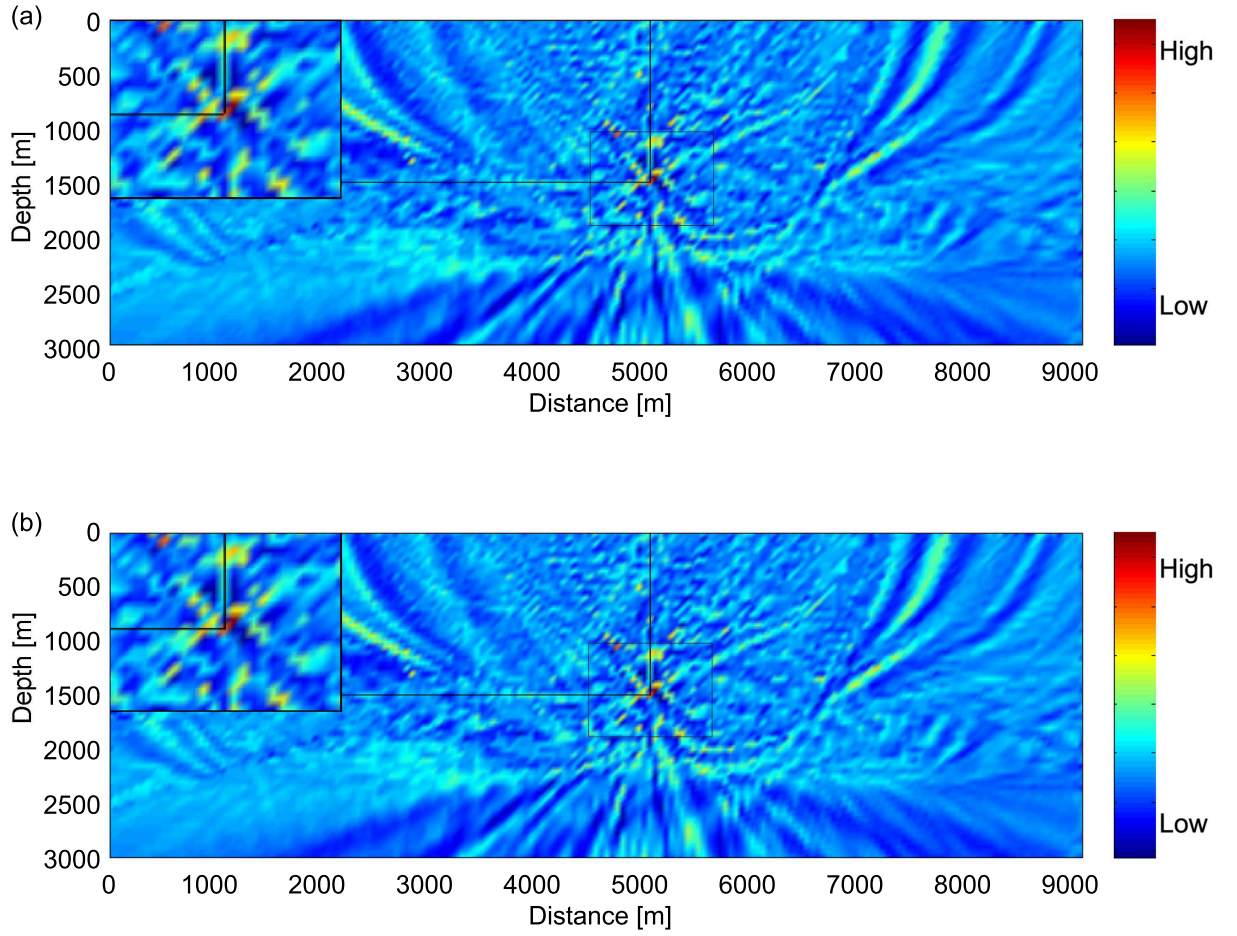


FIGURE 3.11: Localisation of a high frequency point source event simulated by a Ricker wavelet with a central frequency of 60 Hz in smoothed complex media. Stacks over the results of horizontal and vertical component are shown. (a) Cross-correlation stacking image of first arrivals and (b) most energetic arrivals.

The localisation procedure is applied separately to both the horizontal and vertical components of the particle velocities. Then I stacked the results to obtain the final image function. For the high frequency data the first arrival traveltimes match with the moveout of the events fairly well (see Figure 3.5). Therefore, the maximum amplitude is expected at the correct location for this data (see Figure 3.11), which is in fact the case. This is not true for the low frequency signal, since in this case several events are interfering. The moveout of the first arrivals is slightly larger than high frequency data (see Figure 3.12). This leads to a maximum of the image function at a shallower level. For the low frequency data, a difference is observed when the first instead of most energetic arrival traveltimes are used. The imaging result obtained by using the

most energetic arrivals is better focused than the one by first arrivals. The maximum of the image function by first arrivals is shifted about 100 m upward, whereas the image function by the most energetic arrivals is shifted about 70 m downward compared to the source position (see Figure 3.12). In the next examples, microtremor events are considered.

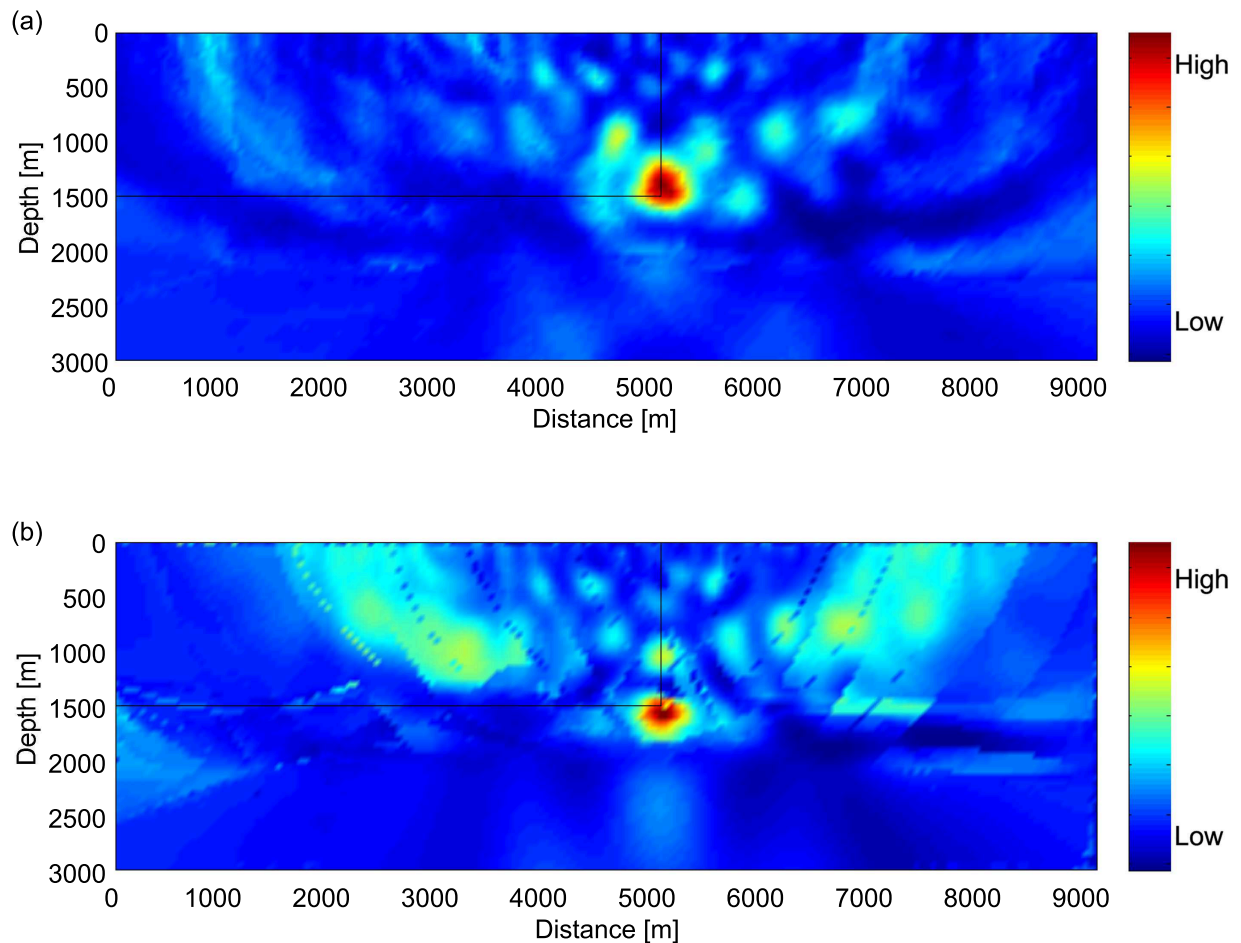


FIGURE 3.12: Localisation of a low frequency point source event simulated by a Ricker wavelet with a central frequency of 60 Hz in smoothed complex media. Stacks over the results of the horizontal and vertical component are shown. (a) Cross-correlation stacking image of the first arrivals and (b) most energetic arrivals.

### 3.7.2 Microtremors simulated by explosion source

The cross-correlation stacking based imaging is applied by using first or most energetic arrival traveltimes to localise the microtremors. Figure 3.13 demonstrates localisation results using first and most energetic arrivals. The white stars in the images indicate the



largest amplitudes of the image function. Figure 3.13(a), shows the localisation result using first arrival traveltimes. They were computed by ray tracing using the model which was smoothed by a 500 m Hamming window. The cloud of high amplitudes displays a lateral extension similar to the reservoir. Its depth is now closer to the actual reservoir depth. The maximum amplitude of the image occurs very close to the reservoir. Figure 3.13(b) illustrates the localisation image using most energetic arrival traveltimes. The image displays a lot of noise in a very broad area of high amplitudes with a magnitude similar to the source area, especially at triplication occurrences (see Figure 3.10).

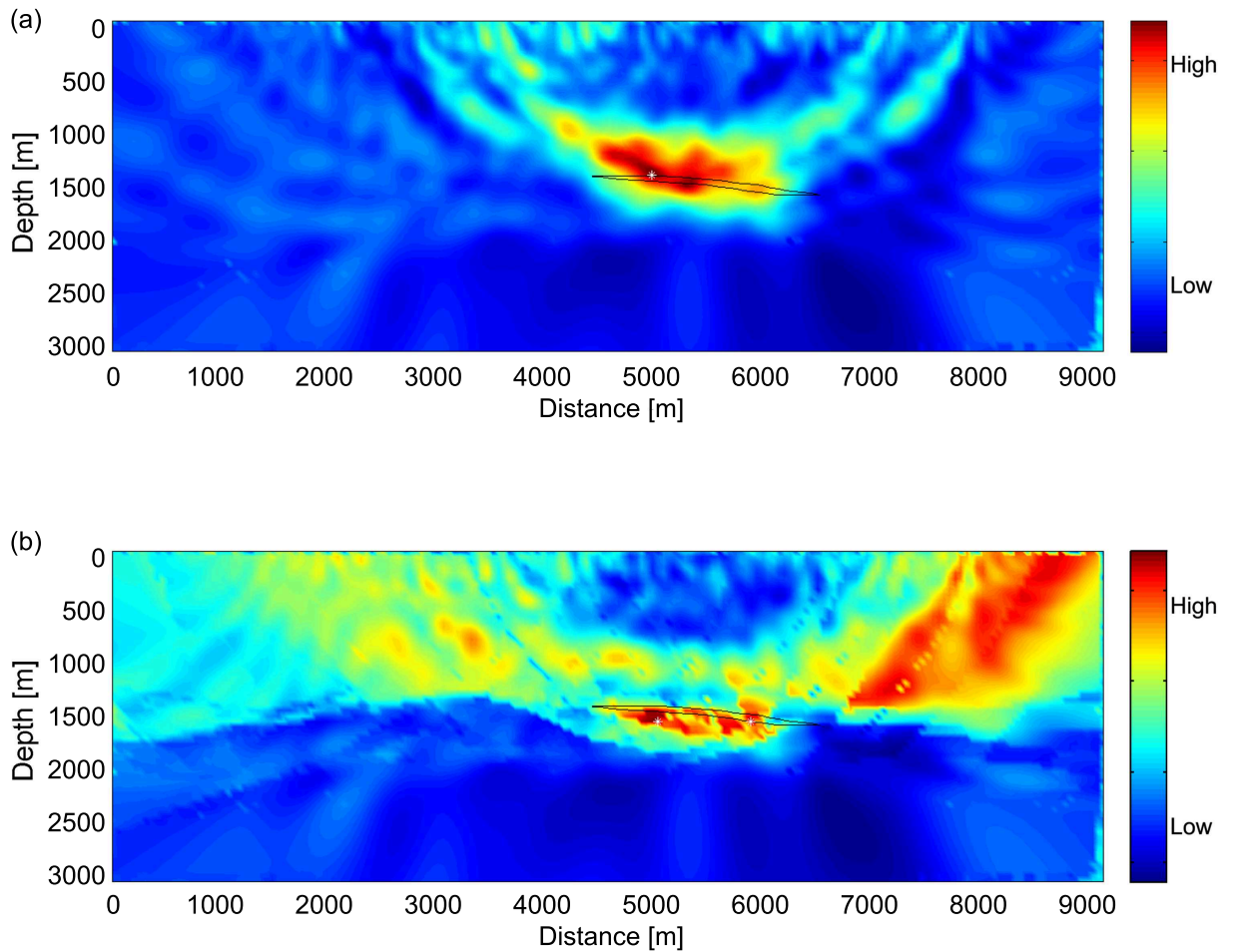


FIGURE 3.13: Localisation of a microtremor signal simulated by an explosion source in smoothed complex media. Stacking over horizontal and vertical images are shown. (a) Cross-correlation stacking result of first arrivals and (b) most energetic arrivals. The white stars define the maxima of the image function.

Figure 3.14 illustrates the comparison of the localisation results based on first arrival traveltimes, at blocky model and smoothed model. The localisation result for the smoothed model is considerably better than the blocky model. It indicates that smoothed model allows reasonable seismic imaging of very complex geological structures. I have seen some difficulties associated with the use of blocky model: it can result in incorrect location of the localisation image. Although ray tracing do not offer perfect kinematic consistency with the low frequency event, i.e. long wavelength, it has the potential, through an approximate kinematic consistency, to give reasonable seismic image of such event.

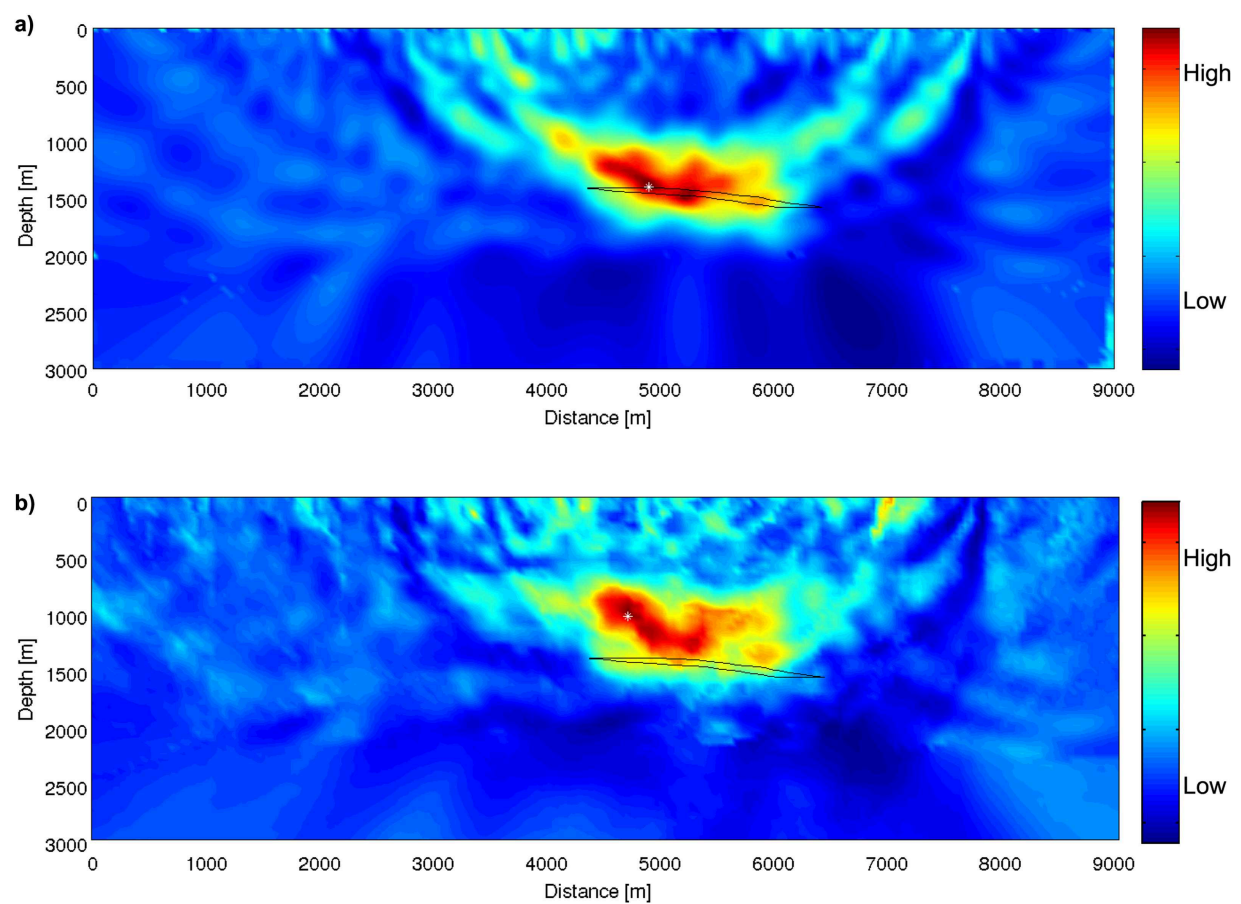


FIGURE 3.14: The comparison of the localisation results of a microtremor signal based on first arrival traveltimes, at (a) smoothed and (b) blocky velocity model. The white stars define the maxima of the image functions.



### 3.7.3 Microtremors simulated by horizontal single force

The type of the source used in this section corresponds to horizontal single forces that mainly emit S-waves in vertical direction. [Steiner et al. \[2008\]](#) developed a source function to add specific values to the velocities in the velocity equations to generate P and S waves with different dominance regarding radiation towards the surface. The applied source function simulates P-waves by adding values to the normal stresses in the stress equations. The horizontal and vertical particle velocities are recorded through time by 11 vertical seismometers at the model surface (see Figure 3.4). The main issue of localisation is the accuracy of the traveltimes. Poor estimation of the velocity model (usually for S-waves), may cause incorrect arrival times for a signal of the same source. Moreover low frequency events may be more effected by model complexity since the computed traveltimes are inherently attributed to high frequency events. Deviations in moveout directly influence the localisation process. This would lead to spatial shift of the focusing point. In this case, S-wave velocities  $V_s$  are derived from P-wave velocities  $V_p$  regarding the P and S-waves velocities ratio

$$\frac{V_p}{V_s} = \sqrt{\frac{2(1-\nu)}{1-2\nu}} \quad (3.2)$$

I considered the Poisson's ratio is considered to be constant and equal to  $\nu = 0.2$  for this specific model. I used first arrival traveltimes of both P and S-waves in the localisation procedure separately, then stacked the localisation images. Figure 3.15(a) shows the localisation result where the image function is stacked over horizontal and vertical images. Figure 3.15(b) displays the case where the final image function is provided by scaling the horizontal image to the vertical image.

The cloud of high amplitudes in the image where amplitudes of horizontal and vertical images are stacked, displays a lateral extension similar to the reservoir. However it occurs too high compared to the actual depth of source area (see Figure 3.15(b)). This can be an effect of poor approximation of the traveltimes, which may result to incorrect location for the same source. However, scaled horizontal to vertical images provided a better result. The lateral extension of high amplitudes appears at a similar position as the reservoir. Its depth is also close to the actual reservoir depth. The maximum amplitude of the image function occurs very close to the reservoir (see Figure 3.15(a)).

### 3.7.4 Microtremors simulated by Vertical single force

The type of the source used in this section corresponds to vertical single forces that mainly emit S-waves in horizontal direction. [Steiner et al. \[2008\]](#) developed a source function to add specific values to the velocities in the velocity equations to generate P and S waves with different dominance regarding radiation towards the surface. The

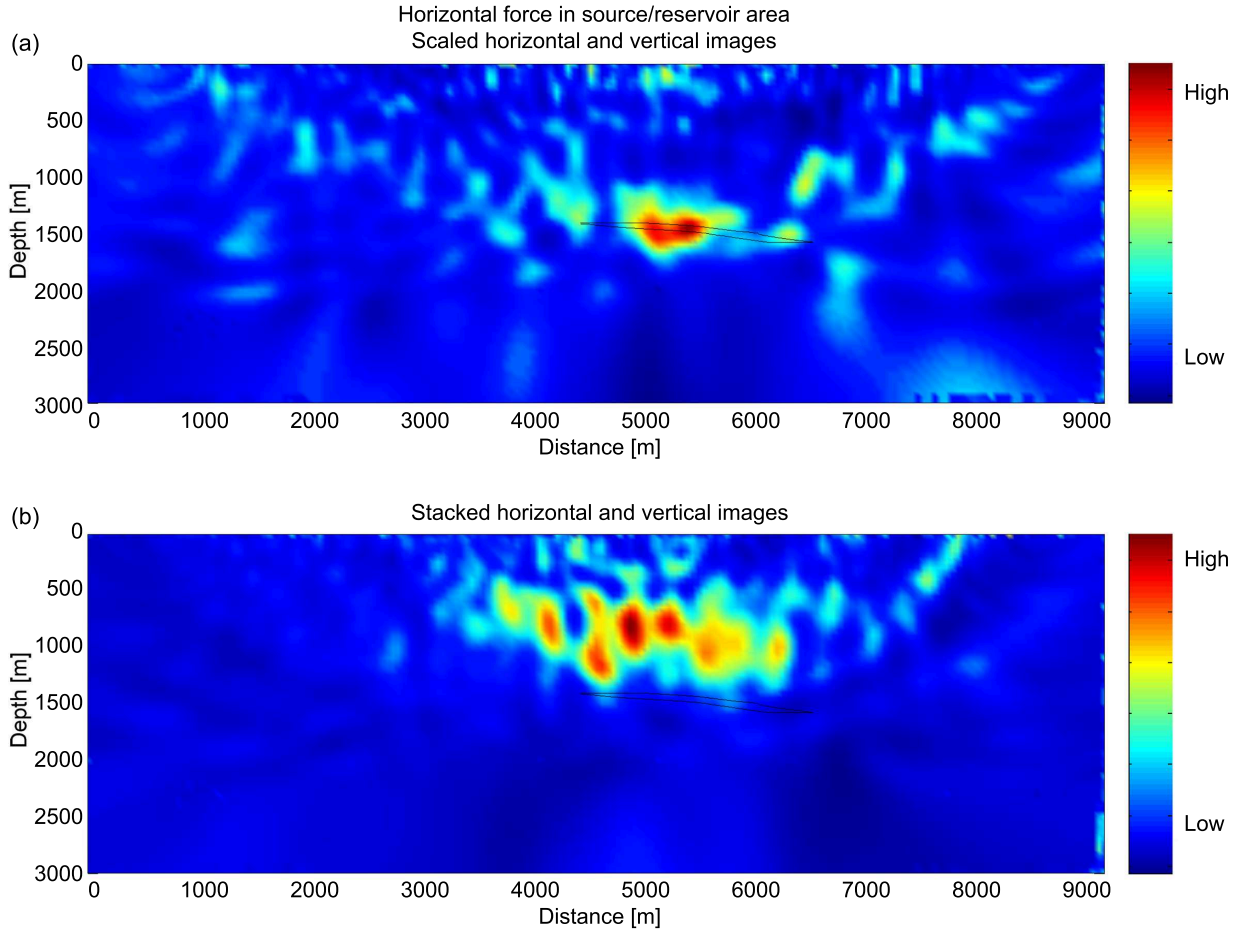


FIGURE 3.15: Localisation of a microtremor signal simulated by horizontal single force in the smoothed complex media. (a) Scaled horizontal to vertical images and (b) stacked horizontal and vertical images are shown.

applied source function simulates P-waves by adding values to the normal stresses in the stress equations. The horizontal and vertical particle velocities are recorded through time by 11 vertical seismometers at the model surface (see Figure 3.4). Again a localisation procedure is applied using S-wave traveltimes to localise the microtremors. Figure 3.16 demonstrates the localisation results of stacked horizontal and vertical images and scaled horizontal to vertical images. Again the cloud of high amplitudes in the image when stacked horizontal and vertical images, displays a lateral extension similar to the reservoir. However high amplitude area appears rather deep compared to the actual depth of the reservoir. Moreover, the image contains a lot of artefacts, which may lead to misinterpretation (see Figure 3.16(b)). Nevertheless, scaled horizontal to vertical images provide a better result. The lateral extension of high amplitudes appears at a similar position to the reservoir and its depth is also close to the actual reservoir

depth. Additionally the maximum amplitude of the image is better focused and close to the reservoir (see Figure 3.16(a)).

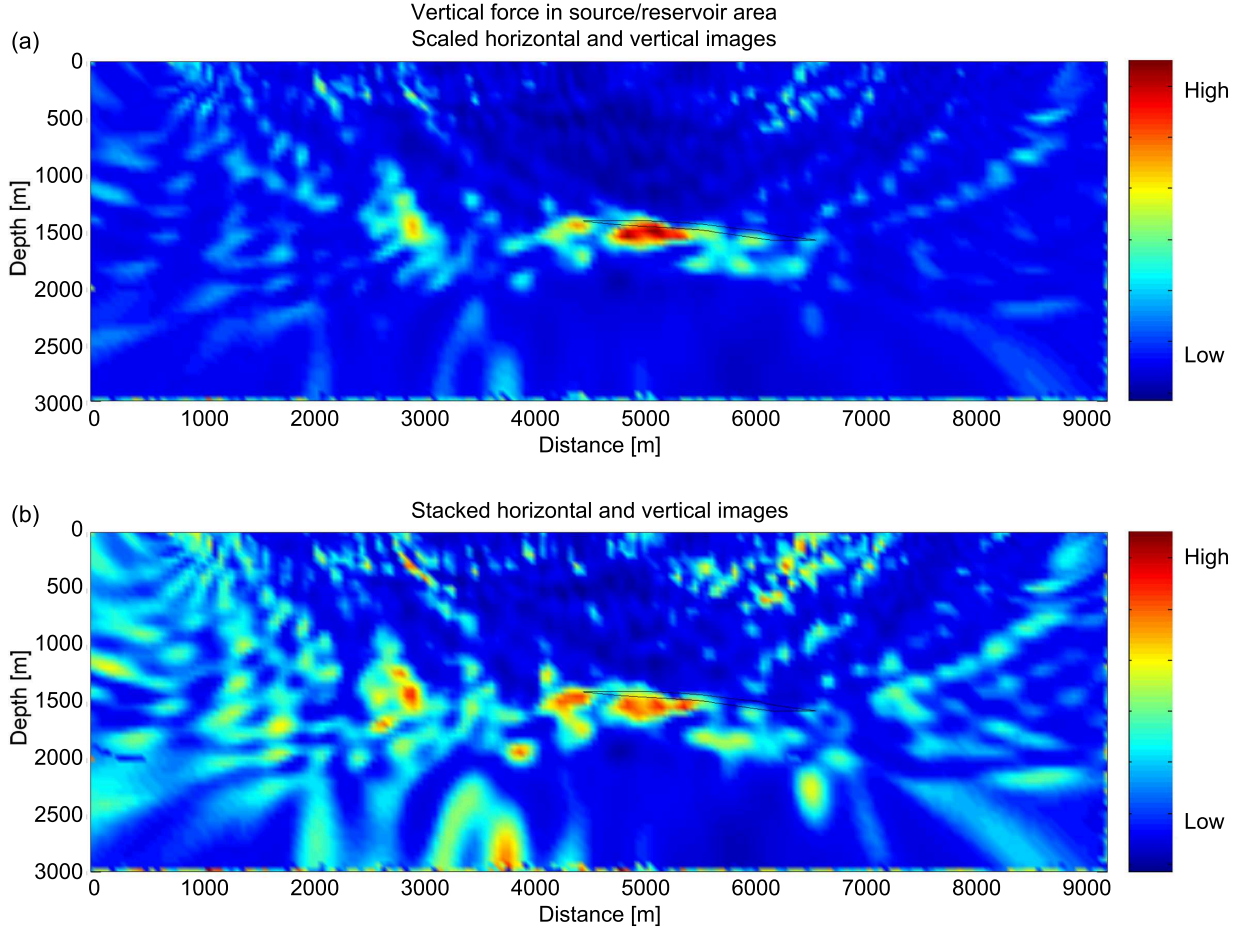


FIGURE 3.16: Localisation of a microtremor signal simulated by vertical single force in smoothed complex media. (a) Scaling the amplitudes of horizontal image to vertical image and (b) stacking over horizontal and vertical images are demonstrated.

In this chapter I provided several synthetic examples at 2-D homogeneous and heterogeneous media to illustrate the impact of method in localisation of the seismic sources. Strong influence of choice of master trace, in correlation process, is shown in homogeneous medium. To avoid this dependency I consider each trace as master trace, then stack all the correlation results. Both P and S-waves' moveouts are considered in localisation separately, then localisation results are stacked. In addition the procedure is applied to horizontal and vertical seismograms separately. Stacking over all the components can provide the final image in this case. In this work scaling horizontal to vertical images is used as another imaging condition which provides the final image. At the end,

cross-correlation stacking procedure provides the location of the seismic event in space and time.

This information makes the seismic monitoring of a reservoir available, which will be investigated in the following chapters. Real-time seismic monitoring of natural or induced seismicity in or around oil and gas production or waste water injection provides the data needed to manage the operations and assess potential risk of induced seismicity.

## Chapter 4

# Acquisition footprint and propagation effects

A major task of this chapter is to overcome the illumination problems caused by the wave propagation and seismic array design. These problems play an important role in many applications of seismology and applied seismics, i.e. migration, tomography, and modelling.

### 4.1 Geometrical spreading compensation

The amplitudes of seismic waves are affected by propagation due to the wavefront divergence and the reflection of the propagating pulse at the many boundaries between rocks of differing impedance. This phenomenon is recognised as geometrical spreading. Figure 4.1 displays schematically a point source within an Earth model and two corresponding wavefronts. The energy flux within this ray tube must remain constant in an elastic medium. However for a wavefront with smaller curvature the same amount of energy is spread over a larger surface than for a wavefront with high curvature. Amplitudes decrease when the wavefront spreads out in area and increase if the wavefront is focused to a smaller area [Shearer, 2009]. Since a detector measures the displacement amplitude, it will register a smaller amplitude for the second wavefront than for the first one (see Figure 4.1).

The ratio of the measuring surface element to the complete wavefront is proportional to  $1/r^2$  in 3-D, and  $\propto 1/r$  in 2-D, where  $r$  is the radius of curvature of the wavefront. The amplitude corresponds to the square-root of the flux, therefore the amplitude of the wave in a 3-D medium decreases with  $1/r$  and with  $1/\sqrt{r}$  in 2-D. The relative geometrical spreading  $\mathcal{L}$  is the inverse of the amplitude, thus  $\mathcal{L} \propto r$  in 3-D and  $\mathcal{L} \propto \sqrt{r}$  in 2-D [Vanelle, 2002]. When a spherical wave propagates in a homogeneous medium, its

amplitude decays with the increase of the distance from the source as  $1/r$ . The energy at far offsets is smaller than at near offsets. Two things affect the geometrical spreading factor: travel distance as mentioned above, and the velocity structure. For a layered model with a trend of increasing velocity with depth, the later arrivals could be more important than the first arrival.

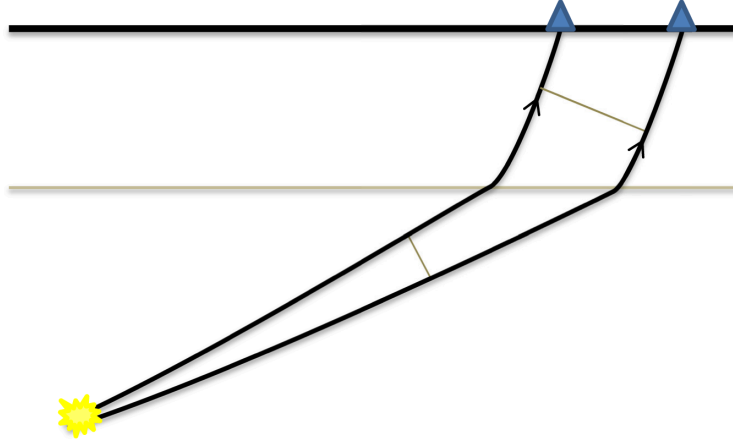


FIGURE 4.1: Raypath geometry for a point source in inhomogeneous medium. Velocities are increasing with depth. The edges of this patch are bounded by the rays that define the local propagation direction.

Ursin [1990] introduced a high order geometrical spreading correction based on elastic wave modelling. Hubral et al. [1992] demonstrated the relationship between the wavefront curvature expressed by the propagator matrix and the ray amplitude. They suggested an expression for the geometrical spreading that is directly related to second order traveltime derivatives in terms of Bortfeld [1989] matrices. Vanelle and Gajewski [2003] improved this idea and present a technique for computing the geometrical spreading by using traveltimes only. The accuracy of the method was sufficient for the calculation of migration weights and divergence corrections. In this chapter, suggested factor for computing geometrical spreading compensation is based on divergence effect. It is closely related to the formula introduced by Newman [1973]. The divergence factor  $D_{one-way}$  which applies in the one-way travel path, is derived for the case of horizontal discrete layering of thickness  $d_i$  ( $\forall i = 1, \dots, n$ ), with no restriction upon the initial incidence angle as

$$D_{one-way} = \frac{\sum_{i=1}^n d_i V_i}{V_s} \quad (4.1)$$

in this expression  $V_i$  is the interval velocity of  $i$ th layer and  $V_s$  is the velocity at the source position. Geometrical spreading factor  $\mathcal{L}$  for a source at  $(x, y, z)$  in an Earth

model consisting of horizontal, isotropic layers is defined as

$$\mathcal{L}(x, y, z) = \frac{t(x, y, z)V_{rms}^2}{V_s} \quad (4.2)$$

where  $t$  is the travelttime of the direct arrival from a source at  $(x, y, z)$  to each receiver location and  $V_{rms}$  represents the root-mean-square velocity.  $V_{rms}$  is determined based on velocity changes along the vertical direction, i.e.  $z$ -axis. Although this formula is only applicable in horizontally stratified media, throughout this study it has considered to solve for propagation problems in heterogeneous media. Therefore, the image function regarding Equation 2.16, by considering the geometrical spreading compensation, is obtained as

$$M(x, y, z) = \sum_{i=1}^N (\mathcal{L}_i(x, y, z) \int_{t_1}^{t_2} E_i(x, y, z, t) dt) \quad (4.3)$$

for the selected time interval  $[t_1, t_2]$  over all receivers  $[1, N]$ . The dataset is weighted with this compensation for each receiver location. It separates the source effects from propagation effects. In this work angel of incident is not considered in geometrical spreading. Considering the angel of incident helps specially in computing the geometrical spreading of far offsets.

## 4.2 Acquisition footprint

In seismic surveys, it is possible to design the acquisition geometry because geophysicists usually have control over the number and position of receivers. But sometimes, especially in passive seismics, the target zone is located in access limited environments, so the acquisition geometry will be a sparse irregular pattern. The acquisition pattern of a 3-D surveys can have a significant effect on the imaging result [Canning and Gardner, 1998]: when the spatial distribution of input traces is irregular, the localisation results can be contaminated by artefacts. Therefore, resulting acquisition footprint can lead to in inaccurate interpretation of images.

In land seismic surveys, surface barriers and a variety of acquisition patterns are responsible for the irregular spatial sampling. The irregularity causes the footprint of the acquisition patterns, which can be observed in 3-D seismic data sets. This effect is amplified when multichannel procedures are applied [Canning and Gardner, 1998]. When the input space is irregularly sampled, the reconstructed amplitude is inexact and the destructive interference is imperfect, thus introducing noise to the data. This problem arises frequently in passive seismics, where sparse and irregular networks are more common than in active experiments.



One possibility to eliminate the problem is suggested by [Canning and Gardner \[1998\]](#). [Canning and Gardner \[1998\]](#) introduced a simplified algorithm based on computing the area around each point. They considered a regular data set, where equal weight (e.g. one) is assigned to each cell of the grid. Each grid point is represented by one trace, as the dataset is regular (see Figure 4.2a), so every trace receives the same weight. In case one trace is missing, polygon construction changes (see Figure 4.2b). The area which belongs to the missing trace is divided by the four nearest grid points. In the example presented in Figure 4.2c, three adjacent traces are missing. The area which corresponds to the missing traces, is not divided equally between the surrounding presented grid points. Instead, it is divided in a more complicated pattern. Nonetheless, it shows the procedure of computing the area around each trace can be viewed as the division of the area belonging to the missing traces between the existing traces. When all traces are projected onto a regular grid, the position of the trace is rounded to the nearest grid point. Consequently, the accuracy of the resulting weighting function is directly related to the density of the grid [[Canning and Gardner, 1998](#); [Zhebel et al., 2011](#)].

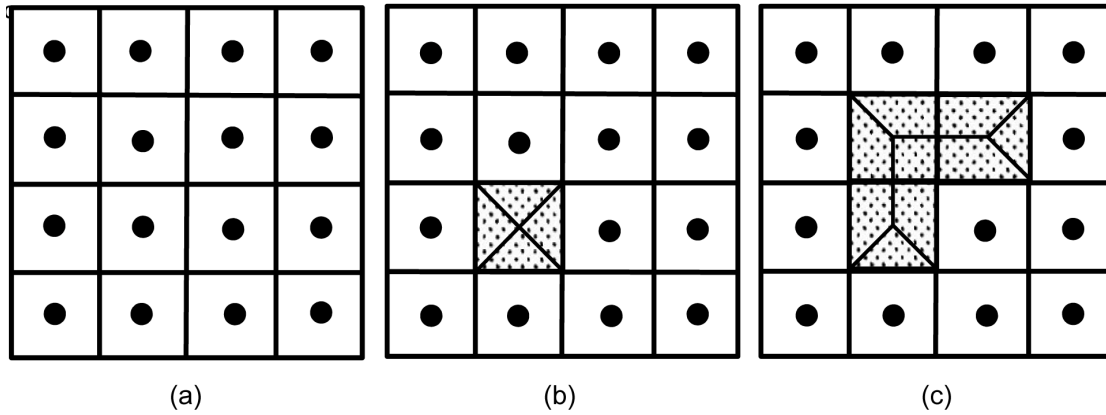


FIGURE 4.2: Simplified grid construction for computing the area around each point in case of (a) regular grid, (b) one cell missing and (c) three cells missing. The shaded area represents the absence of a trace and the black bolt represents the existence of a trace in the cell [[Canning and Gardner, 1998](#)].

The basic idea behind such neighbourhood algorithms is the usage of Voronoi cells to search in parameter space [[Voronoi, 1908](#)]. Figure 4.3 demonstrates the geometrical properties of Voronoi diagrams. The area around any input point  $P$  in Figure 4.3 is described by the locus of all points in  $(x, y)$  space that are closer to  $P$  than any other input point. This area is bounded by polygons known as Voronoi diagrams. Voronoi cells are nearest neighbour regions, defined by a suitable distance norm [[Voronoi, 1908](#)].



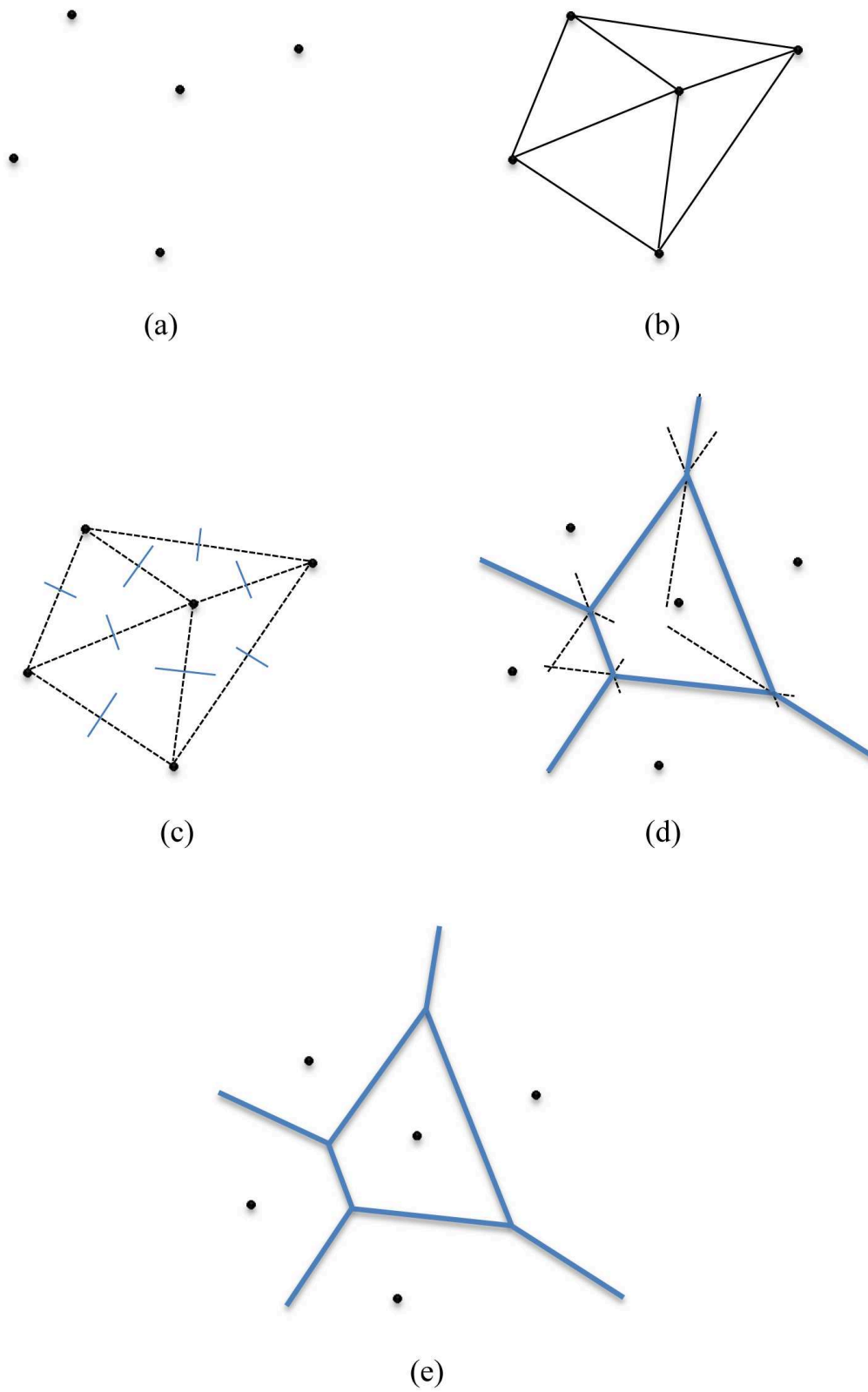


FIGURE 4.3: Definition and basic properties of Voronoi diagrams. (a) Some points are considered, (b) the nearest neighbouring points are connected by lines, (c) the connecting lines are halved, (d) extension of the perpendiculars leads to their intersections, (e) the area spanned by these intersecting points is the Voronoi cell.

The procedure used in this study to overcome the problem is to assign a weight based on calculating the effective region for each receiver from Voronoi cells. That I describe in the following.

- Points (receivers) are considered as the centres of polygons (cells)
- A line is drawn between each adjacent points
- A perpendicular bisector is constructed for every line between neighbouring pairs
- The edges of the polygons are computed
- The intersections of all those perpendiculars define the vertices which construct the polygons
- Lines-to-infinity are computed
- Model boundaries need be considered to avoid bisectors to infinity
- The area of the polygons are determined
- The final weight is assigned to each point based on the normalised area of the cell comprising the point

Some more details about the procedure are given in the following paragraphs. Throughout this study, it is assumed that the points (receivers) are in a 3-D space  $\mathfrak{R}$  and the metric distance is Euclidean. For simplicity the equations are provided in 2-D. The Euclidean distance between two points  $p$  and  $q$  is denoted by  $r(p, q)$ . In the 2-D space it is assumed [de Berg et al., 2008]:

$$r(p, q) := \sqrt{(p_x - q_x)^2 + (p_y - q_y)^2} \quad (4.4)$$

Suppose  $P := \{p_1, p_2, \dots, p_n\}$  be a set of  $n$  distinct points in the space  $\mathfrak{R}$ . These points are the receivers (see Figure 4.3). The Voronoi cell  $V(p)$ , of the point  $p$  from the set  $P$ , is defined as the unique convex polygon which contains all the points in the set  $V(p)$  [de Berg et al., 2008]:

$$V(p) = \{q \in \mathfrak{R} | \forall p_i \in P, r(q, p_i) < r(q, p_j)\} \quad (4.5)$$

Assuming that such a bounded polygon exists (see Figure 4.4). Furthermore, it is assumed that  $p \in P$ . Although this convention differs from the theory of Voronoi diagrams, the result is the same. The key issue in this section is the areas of Voronoi polygons.

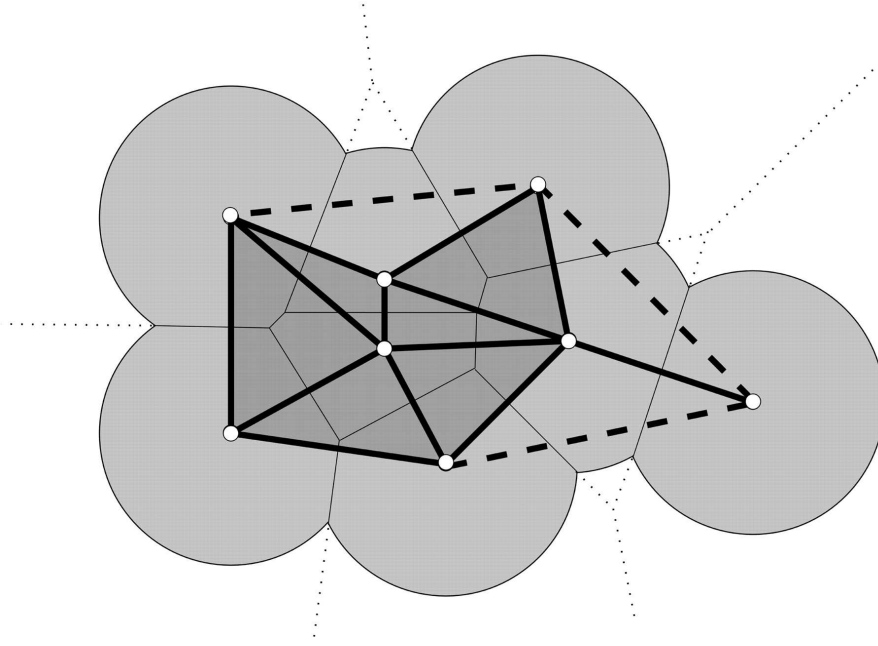


FIGURE 4.4: Schematic areas of Voronoi polygons

I consider a set of areas,  $A := \{A_1, A_2, \dots, A_n\}$  in the space  $\mathfrak{R}$ . Let's assume

- Area  $A_i$  is a connected closed set.
- Areas do not overlap each other, i.e.,

$$A_i \cap A_j = \emptyset \quad , \quad i \neq j, \quad , \quad \forall i, j \in I_n \quad (4.6)$$

- An Area  $A_i$  is not necessarily convex.
- An Area  $A_i$  may have holes in which another area may exist.

Using these assumptions, a distance from a point  $p$  to an area  $A_i$  is defined as the shortest distance from  $p$  to  $A_i$ , i.e.,

$$d_s(p, A_j) = \min_{x_i} \{\|x - x_i\| : x_i \in A_i\} \quad (4.7)$$

where  $x$  and  $x_i$  are the location vectors of  $p$  and  $p_i$ , respectively. Concerning this distance, it is defined a set of Voronoi polygon area  $V(A_i)$  associated with  $A_i$  by

$$V(A_i) = \{p : d_s(p, A_i) \leq d_s(p, A_j), j \neq i, \forall i, j \in I_n\} \quad (4.8)$$

Therefore, a set of the Voronoi polygon area is generated by the set  $A$  corresponding to

$$V(A) = \{V(A_1), V(A_2), \dots, V(A_n)\} \quad (4.9)$$

Area Voronoi diagrams are useful to compensate the irregular spatial sampling. Thus, the modified image value,  $E_{Vi}$ , is described by

$$E_{Vi} = V(A_i)E_i \quad (4.10)$$

$E_{Vi}$  is calculated for each receiver using Equation 2.14. Finally, the modified image of the localisation by considering the acquisition footprint removal and geometrical spreading compensation is

$$M(x, y, z) = \sum_{i=1}^N \int_{t_1}^{t_2} \mathcal{L}_i(x, y, z) E_{Vi}(x, y, z, t) dt \quad (4.11)$$

In the following, 3-D synthetic examples are considered before and after using the acquisition footprint removal and geometrical spreading compensation. I verify the method and discuss their influence on the localisation procedure. Although the point sources have completely different source characteristics compared to the tremors, they provide insight to check the performance of the procedure.

### 4.3 Application to synthetic data with an impulsive source

The complex heterogeneous velocity model constructed by Steiner [2009] is considered, and is extended to 3-D with a 2.5 D velocity distribution. So the velocity is constant along the transverse, i.e.  $y$ -axis. It is assumed that the velocity value of the corresponding  $(x, y \neq 0, z)$  position of 2-D model. This model consists of ten sedimentary layers with P-wave velocities between 1200 and 3000 m/s above a crystalline basement with a P-wave velocity of 6000 m/s (see Figure 4.5). Figure 4.6 illustrates an arbitrary surface array consisting of 31 seismometers and the related Voronoi polygons as seen from the top. The type of the source used in this section corresponds to a horizontal single force that mainly emits S-waves in vertical direction. The horizontal and vertical particle velocities are recorded through 4 s by 31 seismometers which are irregularly distributed at the model surface (see Figure 4.6).

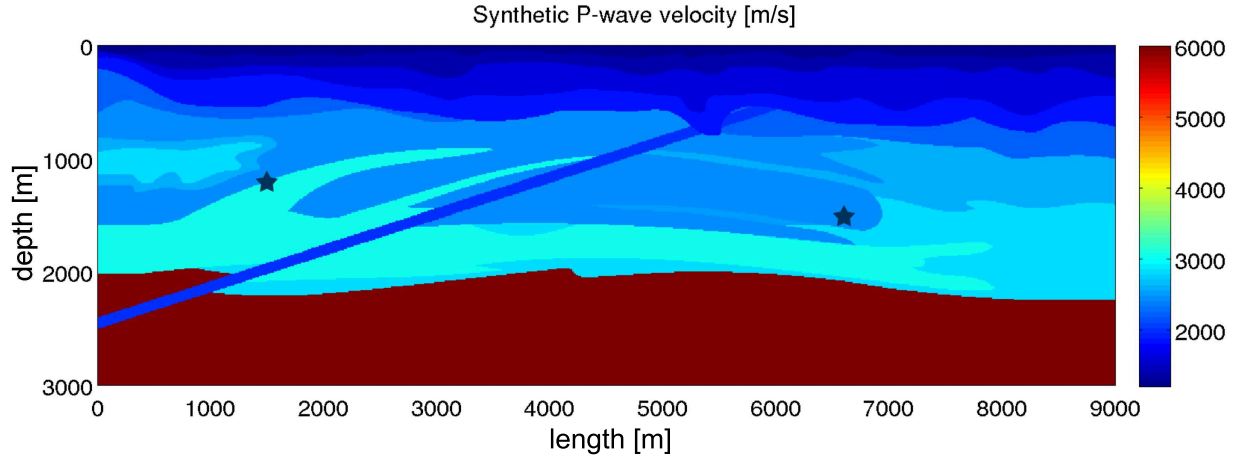


FIGURE 4.5: The synthetic velocity model consists of ten sedimentary layers above a basement unit. Black stars define the source positions in the XZ-plane. The colour legend on the right shows the P-wave velocity in m/s [Steiner, 2009].

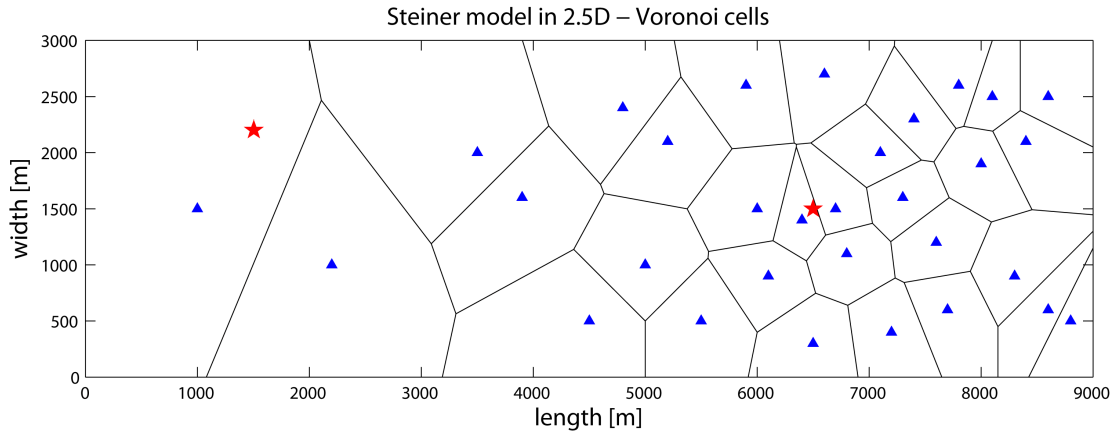


FIGURE 4.6: The 2-D array on the surface consists of 31 seismometers (blue triangles). The polygons mark the related Voronoi cells. The two stars indicate the epicentres of the microseismic events.

Synthetic seismograms were generated for two horizontal single force sources. One is set within the aperture of the seismic array and the other at the edge of the aperture with minimal coverage by the array. A Ricker wavelet is used as a source time function with a 10 Hz main frequency and SNR of about 5. The horizontal and vertical particle velocities are recorded through time by 31 vertical seismometers at the model surface (see Figure 4.7).

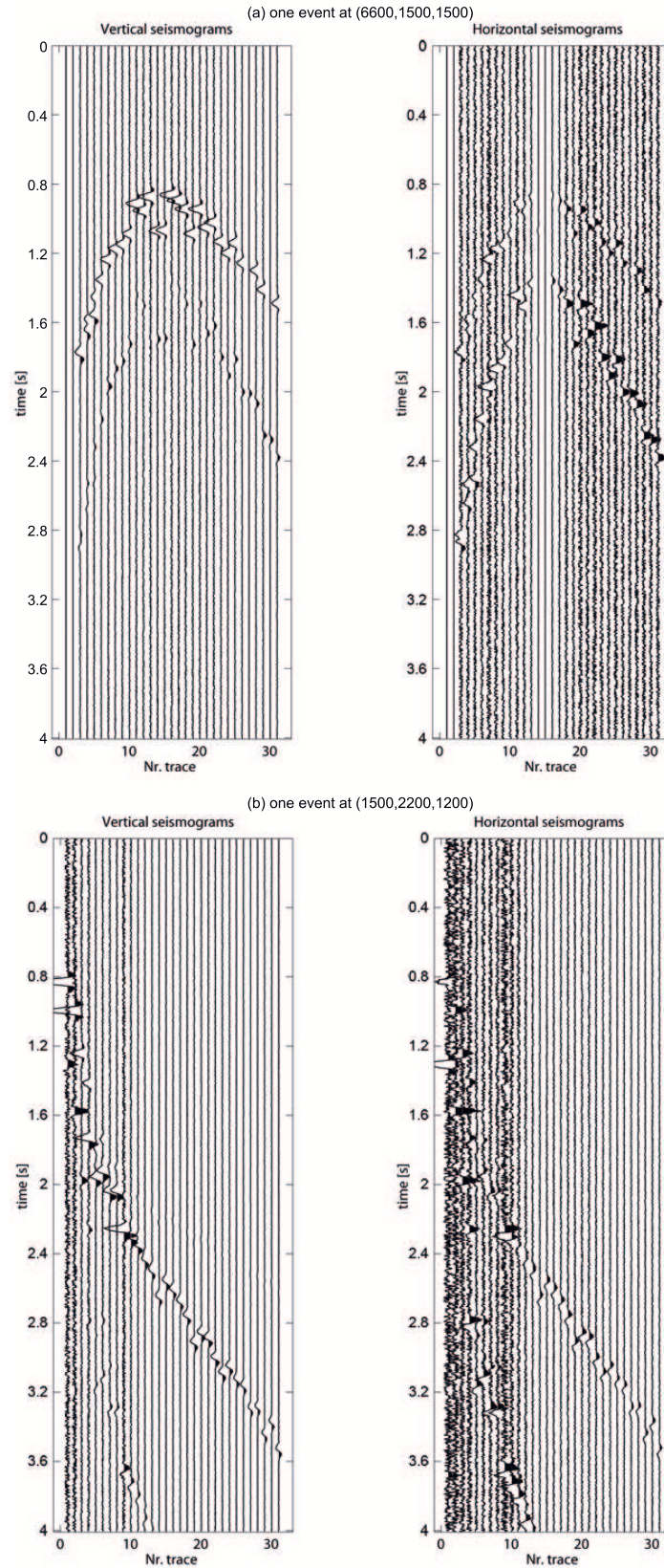


FIGURE 4.7: Seismograms of the sources in a heterogeneous model. (a) One set within the aperture of the seismic array and (b) the other one at the edge of the aperture with minimal coverage by the array with the SNR of 5. A Ricker wavelet with central frequency of 10 Hz is used to compute the traveltimes.



The localisation procedure was applied with P and S-wave first arrival traveltimes performed individually, to localise each source. Afterwards the localisation results of P and S-wave are stacked. Figure 4.8 demonstrates the localisation images of the event set within the aperture in the complex media, without and with removal of the acquisition footprint and compensation for geometrical spreading. The application of the method to the data led to a well focused image with a maximum corresponding to the real source position, with no significant improvement by considering acquisition footprint and geometrical spreading.

Figure 4.9 illustrates the localisation images of the event at the border of the aperture in the complex media, without and with the removal of the acquisition footprint and compensation for geometrical spreading. The application of the method to the data led to a well focused image function with a maximum corresponding to the real source position. However, the image without the correction is very noisy. This could be an expression of poor event coverage by the array (see Figure 4.9(a)). In this case, the correction procedure has considerably improved the image and reduced the amount of noise (see Figure 4.9(b)).

Figure 4.10 displays the 1-D amplitude section of two events without and with acquisition footprint removal (FP) and geometrical spreading correction (GS) performed individually at the real source position along length and width directions, respectively. Although both corrections improve the image, it is shown that the acquisition footprint removal obtains the higher image value at source position compared to geometrical spreading compensation. Acquisition footprint removal and geometrical spreading compensation increase the amplitude of the image function at source position and thus provide better SNR and reliable detection.

A survey acquisition with sparsely and irregularly distributed receivers leaves a footprint on the image. The acquisition footprint removal allows for a separation of source and receiver effects. Geometrical spreading compensation also allows to separate the source effects from propagation effects. Weighting the data results in a more focused image function. Image functions generated in this way allow for a direct comparison of the source strengths. However sometimes it leads to artificial focusing in the image.

Now that I have shown that the method performs well for the localisation of an impulsive source, I will investigate it on some field examples in the next chapter.

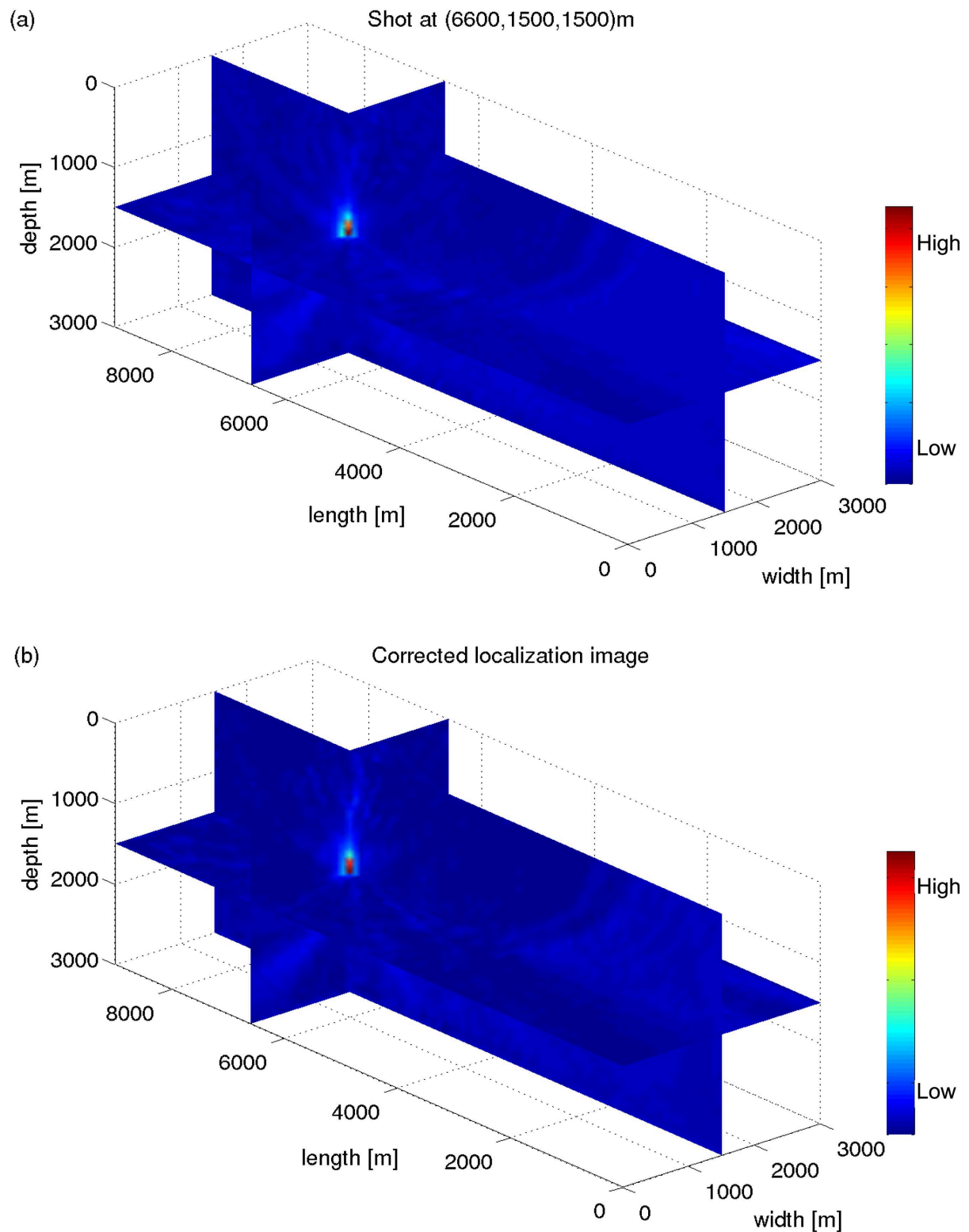


FIGURE 4.8: Image function for a point source event set within the aperture at (6600,1500,1500) in a complex media. (a) Without the correction for the acquisition footprint and the compensation for geometrical spreading, and (b) with the correction.

The maximum value of the image corresponds with the source location.



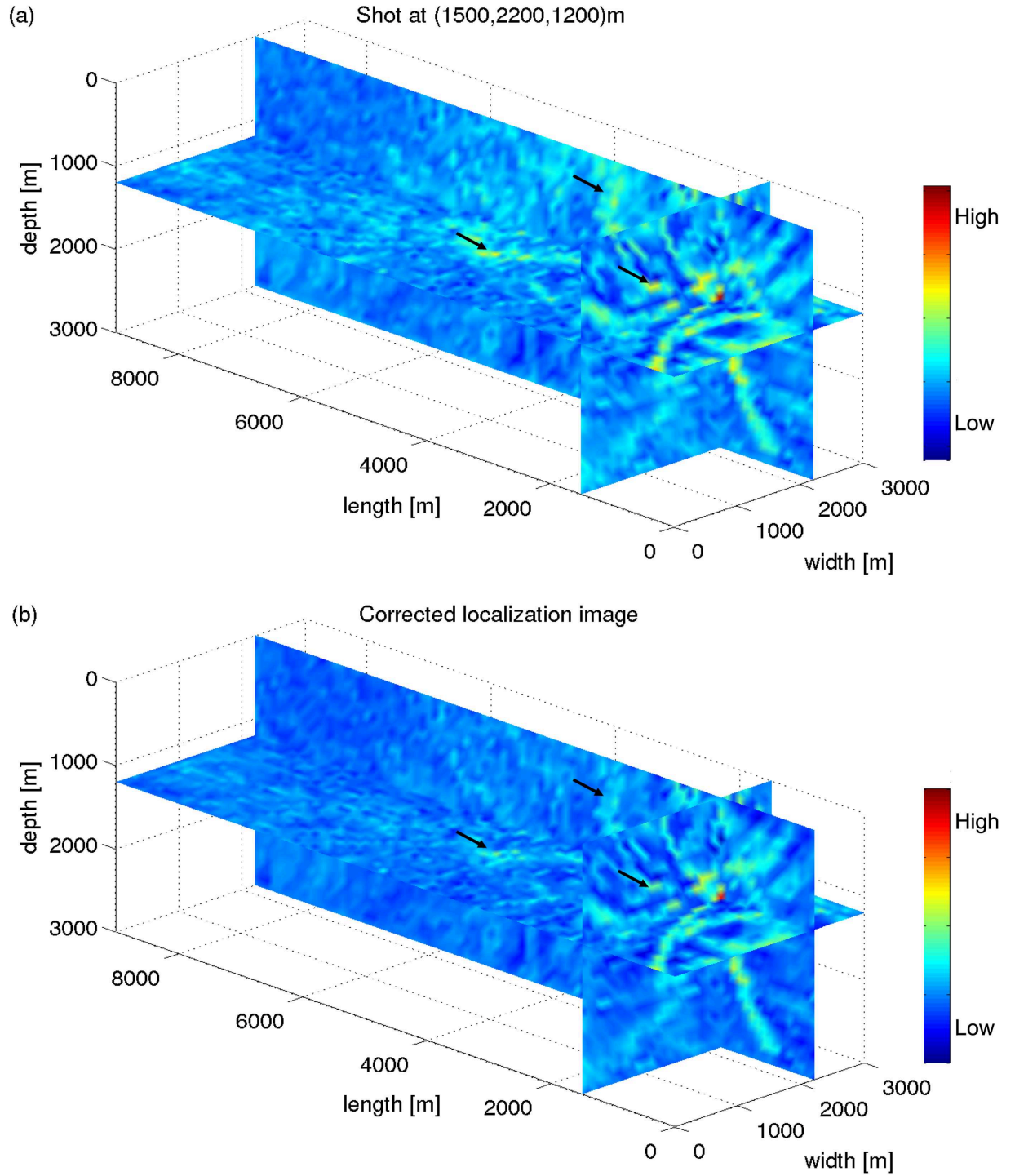


FIGURE 4.9: Image function for a point source event set at the edge of the aperture at (1500, 2200, 1200) in a complex media. (a) Without the correction for the acquisition footprint and the compensation for geometrical spreading, and (b) with the correction. The maximum value of the image corresponds with the source location. Arrows indicate the changes in the amount of noise in the image without and with the correction. The correction leads to a considerable reduction of the noise.

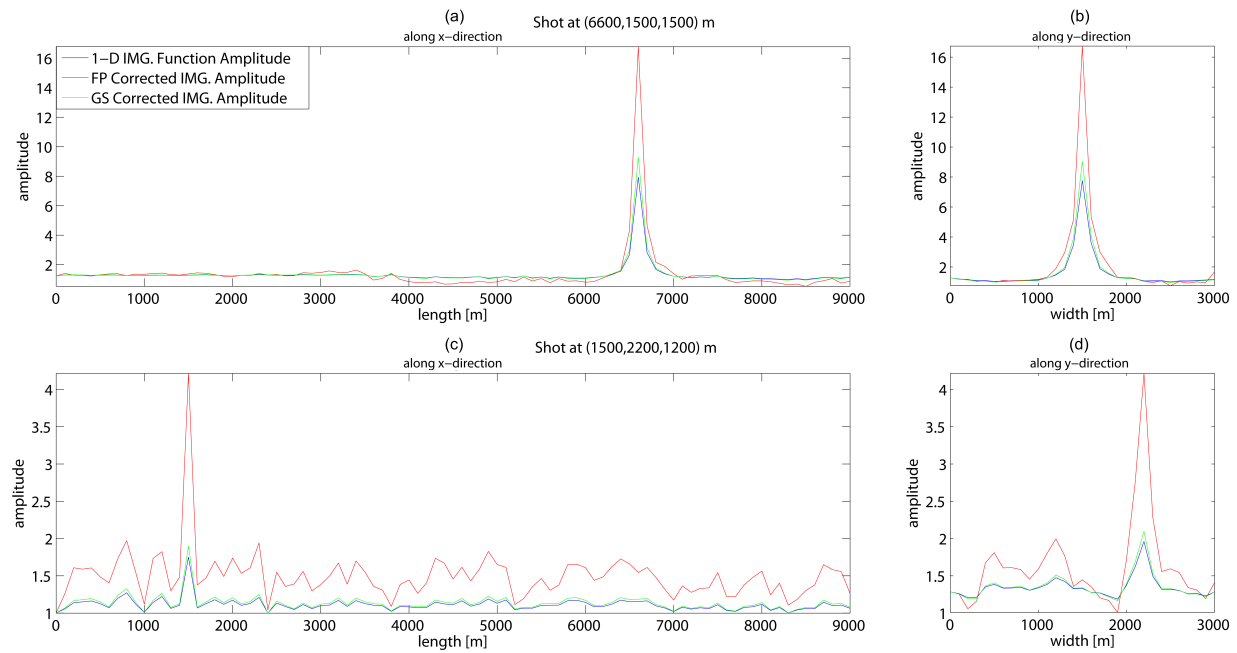


FIGURE 4.10: 1-D amplitude section without and with acquisition footprint removal (FP) and geometrical spreading correction (GS) performed individually. For the point source set within the aperture along (a) length, (b) width direction and the point source set at the edge of the aperture along (c) length, (d) width direction. The depth and length, respectively width coordinates are taken at the real source position.

## Chapter 5

# Application to field data

In this chapter the localisation method is applied to a subset of the induced microseismic event dataset and episodic tremor and slip dataset. Although microseismic recordings have completely different characteristics compared to the tremors, it is a good experiment for checking the performance of the method.

### 5.1 Induced microseismic event

Induced hydraulic fracturing is a reservoir stimulation technique where fluid is injected to a wellbore in order to create fractures (usually less than 1.0 mm wide). This is done, e.g. in shale gas formations in order to allow natural gas to migrate to the well. Hydraulic fracturing is commonly used for production well completion of formations of low-permeability, and greatly assists in mobilising fluids (gas, petroleum), and thus increases the productivity of the well. Induced microseismic is a consequence of the fracturing process. Microseismic monitoring is used to estimate the size and orientation of induced fracturing.

For the particular field investigation, I applied the cross-correlation stacking approach to a dataset from a hydraulic fracturing experiment from an unknown reservoir area. Since it was supposed to be a blind test, there is neither information about the source location nor about the field under consideration. Figure 5.1 illustrates the 1-D velocity model for the field under consideration. Absolute value of velocity as a function of depth,  $Vel$ , corresponding average velocity,  $V_{mean}$ , and root-mean-square velocity  $V_{rms}$  model are shown. In this study the root-mean-square velocity model is considered, i.e. a lateral homogeneous 3-D model is considered to compute the traveltimes of each image point to all the receiver positions. The data were used the dataset recorded by 951 receivers on the surface above the reservoir area. Figure 5.2 illustrates the distribution of the vertical component receivers. The injection pad is approximately in the centre of the array. Lines of receivers radiate from the injection pad.

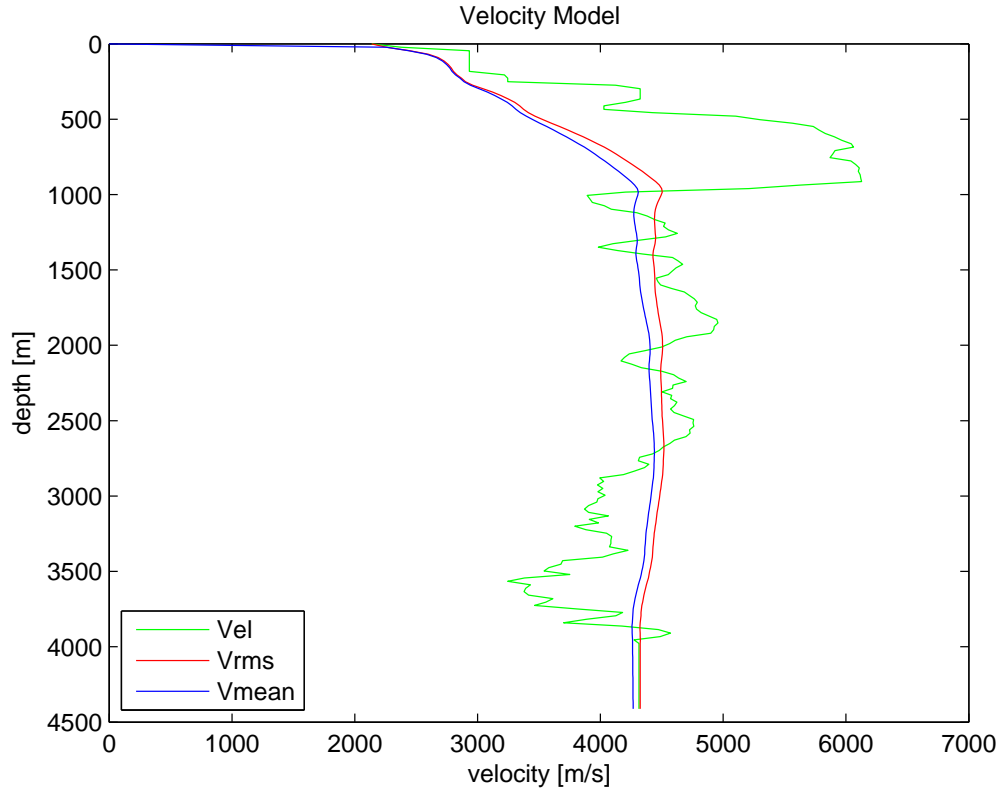


FIGURE 5.1: The 1-D velocity model of a hydraulic fracture experiment.

Figure 5.3 shows the waveforms of particle velocity of a weak event, which were induced during hydraulic fracturing. The localisation procedure is applied to locate this weak microseismic event. Static move-out of the image point with highest amplitude is consistent with the main event. Figure 5.4 shows the localisation result of a microseismic event. The cloud of high amplitudes in the image represents the source position. The maximum amplitude of the image occurs very close to position of the injection pad at approximately the depth of the 4300 m. Although the seismogram looks very noisy the imaging result is very well focussed. The localisation procedure enhanced the signal to noise ratio of this weak event.

Some other maxima are observed in the vicinity of this event. One reason for the high number of similar events may be due to the possibility that the largest events may be associated with a large fault. Their smaller aftershocks (or foreshocks or repeated failures) may provide crucial information about the fracture propagation along these structures [Eisner et al., 2006; Rutledge and Phillips, 2003].

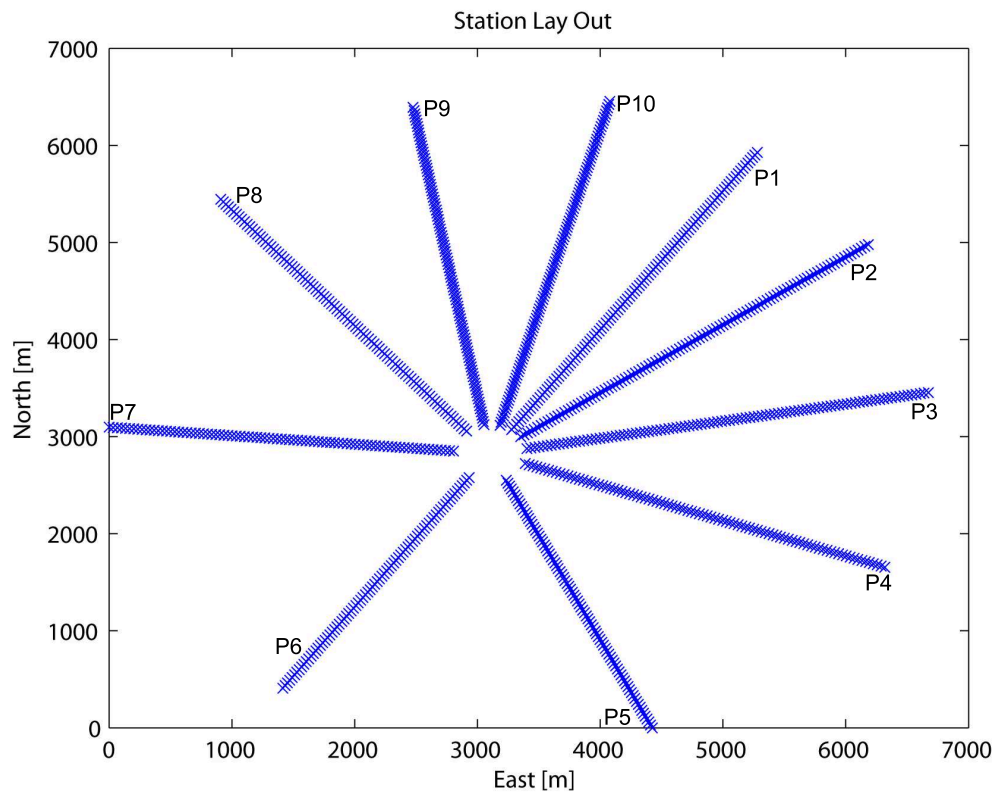


FIGURE 5.2: Distribution of surface receivers along various profiles during monitoring of the hydraulic fracture treatment. A + represents a receiver and the injection pad is at the centre of receivers' lines.

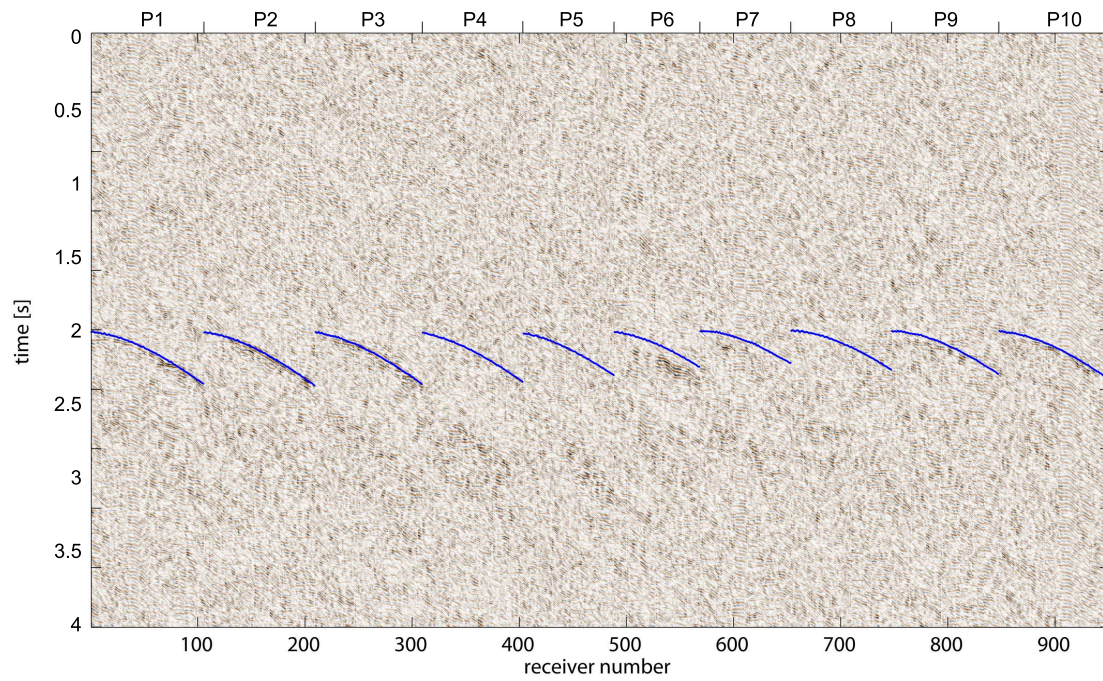


FIGURE 5.3: Waveforms of particle velocity on vertical component geophones due to an induced microseismic event detected. Blue dots indicate the consistent traveltime curves with the main event.



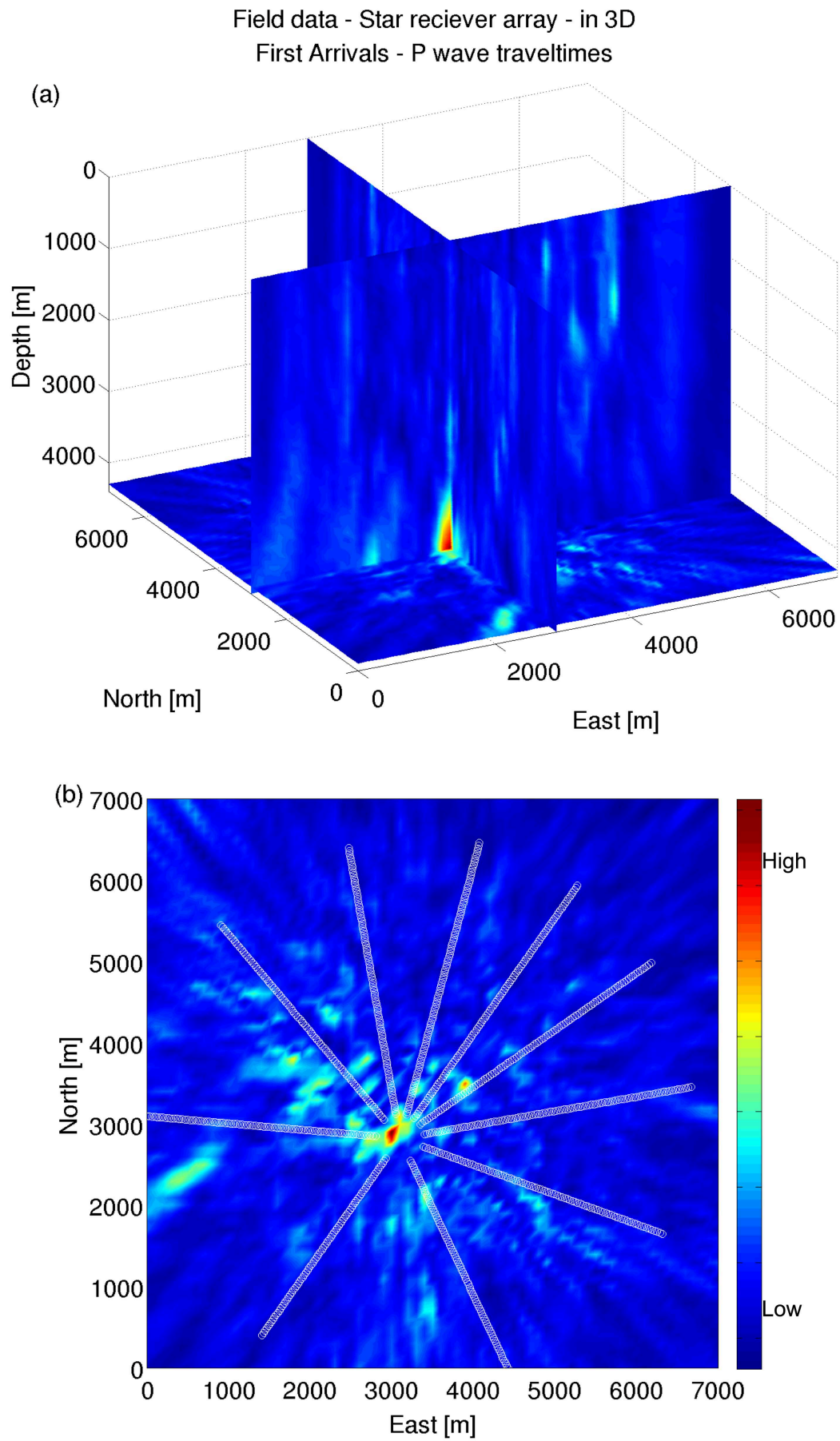


FIGURE 5.4: Localisation of an induced microseismic event in a complex medium.

## 5.2 Non-volcanic tremors in the Cascadia

This section focusses on localisation of deep non-volcanic tremor (NVT), which is one of the seismic expressions of slow slip. NVT has been observed in several tectonically active regions: in subduction zones <sup>1</sup>, including Cascadia [Rogers and Dragert, 2003], southwest Japan (e.g. Shikoku [Obara, 2002] and Osaka [Aso et al., 2011]), as well as at transform plate boundaries <sup>2</sup>, e.g. the San Andreas fault (SAF) [Ryberg et al., 2010]. A relation with the subduction dynamics was inferred from the current occurrence of slow slip, which is detected geodetically [Obara, 2002; Obara and Hirose, 2006]. In these regions, the occurrence of major episodic tremor and slip (ETS) events is surprisingly periodic [Rogers and Dragert, 2003].

In subduction zones, slow slip and tremor are often coupled in space and time. Slow slip occurs in the transition zone, between updip locked and downdip freely slipping segments of the fault. ETS refers to the remarkably periodic slow-slip events and associated NVT activity that recurs approximately every 14.5 months in Cascadia. In short, ETS represents slow earthquakes which occur at the plate interface and accompany tremor [Rogers and Dragert, 2003].

Minor NVT was triggered by the stresses of low-frequency seismic waves radiated by major distant earthquakes [Calvert et al., 2011; Miyazawa and Mori, 2005]. Also, NVT is modulated by ocean tidal loading [Rubinstein et al., 2008], indicating that small stress perturbations may trigger it. NVT is characterised by low amplitudes, a lack of energy at high frequencies, coherent envelopes between seismic stations kilometres apart, emergent onsets, an absence of clear impulsive phases, and durations from minutes to days. The Cascadia subduction zone is a convergent plate boundary which stretches from northern Vancouver Island to northern California. It is a subduction zone with a very long and flat slope fault. The thinner oceanic plate is subducting beneath the thicker continental plate offshore. The Cascadia Subduction Zone is located where these two plates meet (see Figure 5.5). Attempts to locate tremors in Cascadia have resulted in a broad, 50 km-thick distribution in depth. This leads to the interpretation that the tremor is related to a large volume of fluids which are inserted through subduction above the plate interface [Kao et al., 2005; La Rocca et al., 2009; McClausland et al., 2005]. Spatio-temporal distributions of tremors are commonly derived by cross-correlating envelope transformed seismic traces [Obara, 2002] in combination with the source-scanning techniques [Calvert et al., 2011; Kao et al., 2005]. source-scanning method presents mapping the source distribution without any priory knowledge of the orientation or geometry of the actual fault plane. The method exploits the waveform information, including both relative

---

<sup>1</sup>subduction zone is an area where two tectonic plates move towards one another and subduction occurs. In this case, one tectonic plate moves under another tectonic plate, sinking into the Earth's mantle, as the plates converge

<sup>2</sup>Transform Plate Boundary is an area where two tectonic plates slide past one another. The fracture zone that forms a transform plate boundary is known as a transform fault.



amplitudes and arrival times, from an array of seismic stations, to determine whether or not a seismic source is present at a particular time and location [Kao and Shan, 2004]. Recently, tremors were also located by using array processing technique based on beamforming, which is used to stack the data in the tremor frequency band ( $3 - 8Hz$ ) [Ghosh et al., 2009; Ryberg et al., 2010].

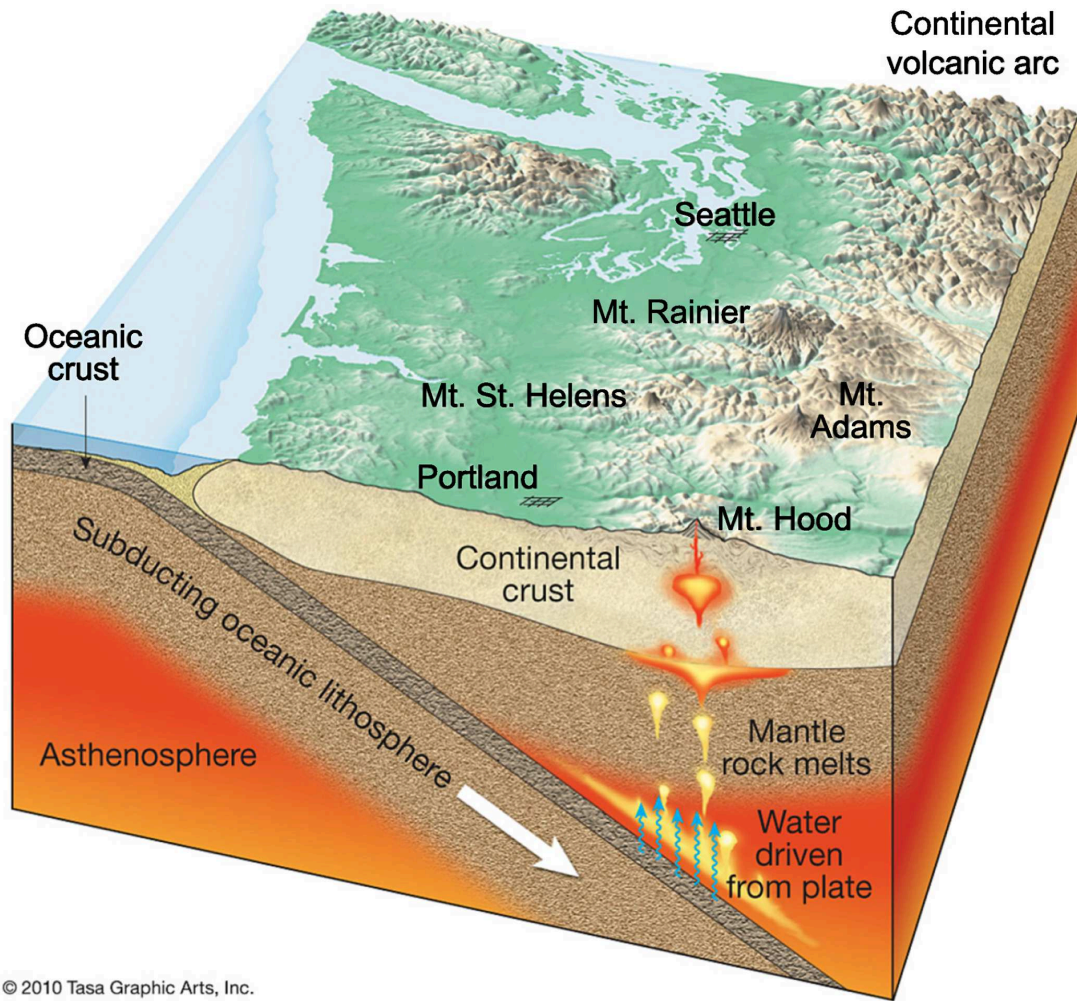


FIGURE 5.5: Structure of the Cascadia subduction zone. The thinner oceanic plate is subducting beneath the thicker continental plate offshore.

This method assumes plane waves and applies a delay-and-sum approach to stack for a range of horizontal slownesses [Ghosh, 2011; Johnson and Dudgeon, 1993]. Moreover, La Rocca et al. [2009] used a localisation method based on S minus P-wave arrival times on NVT in Cascadia to collapsed tremor locations near the plate interface. They applied vertical and horizontal seismograms cross-correlation to reveal signals common to both,

but with the horizontal delayed with respect to the vertical. This lagged correlation represents the time interval between vertical compressional waves and horizontal shear waves. In addition to this direct evidence, bursts of NVT triggered by the surface waves of teleseismic earthquakes at both Cascadia, and SAF correlate strongly with long-period Love waves. The phasing suggests that tremor originates because of the shear slip on the main fault plane [Ghosh et al., 2009; Rubinstein et al., 2008]. However, it is difficult to detect and locate NVT due to its noise-like, emergent waveforms. Therefore, the level of tremor detectability and the resolution of localisation methods are not so clear, and still remain areas of active research. The challenge is to come up with a new procedure that can take a large amount of seismic data and combine it to detect and locate tremors. It is difficult to locate tremor because of its lack of distinct impulsive body wave arrivals used by traditional earthquake localisation methods. Nonetheless tremors in Cascadia contain relatively energetic and isolated pulses which were identified as low-frequency earthquakes (LFEs). They lie above the dipping subduction interface.

Here, localisation results of NVT events are presented using the cross-correlation stacking based imaging. The performance of the method and its ability to extract a weak signal from noisy data was demonstrated in previous sections by using synthetic tests. Localisation images are presented for NVTs which coincide with several LFEs, occurred between the Nov 2012 and Jan 2013 in Cascadia and were reported in the earthquake catalogue provided by USGS/NEIC. Continuous microtremor recordings were collected from IRIS networks. They consist of 53 stations with three-component sensors which recorded data with a sampling interval of 25 ms in continuous mode. Figure 5.6 illustrates the chosen 3-D array on the surface. It shows the related Voronoi polygons which belong to each receiver. Tremor episode datasets were considered for localisation during the Nov 2012-Jan 2013 period. The yellow lines in Figure 5.6 indicate the isolines of 20, 30 and 40 km depth of the slab above the low velocity zone (LVZ) along the Cascadia margin by McCrory et al. [2006]. S-wave velocity studies generally interpret a thin LVZ to be slab crust beneath the entire Cascadia subduction margin. The LVZ may represent a detached fragment of Eocene oceanic crust beneath the Pacific plate McCrory et al. [2006].

The compilation of depth to the plate interface [McCrory et al., 2006] shows a steeply dipping, north-south striking subducting Juan de Fuca plate in southern and central Cascadia. North of 49N, it transits into a shallower dip with a northwest-southeast striking direction. This compilation is based on numerous independent characterisations of slab structure, obtained mostly from active source seismic profiling (e.g., refraction, wide-angle reflection) and regional earthquake tomography. As mentioned before the first step for localisation is traveltime computation, so a velocity model is required.



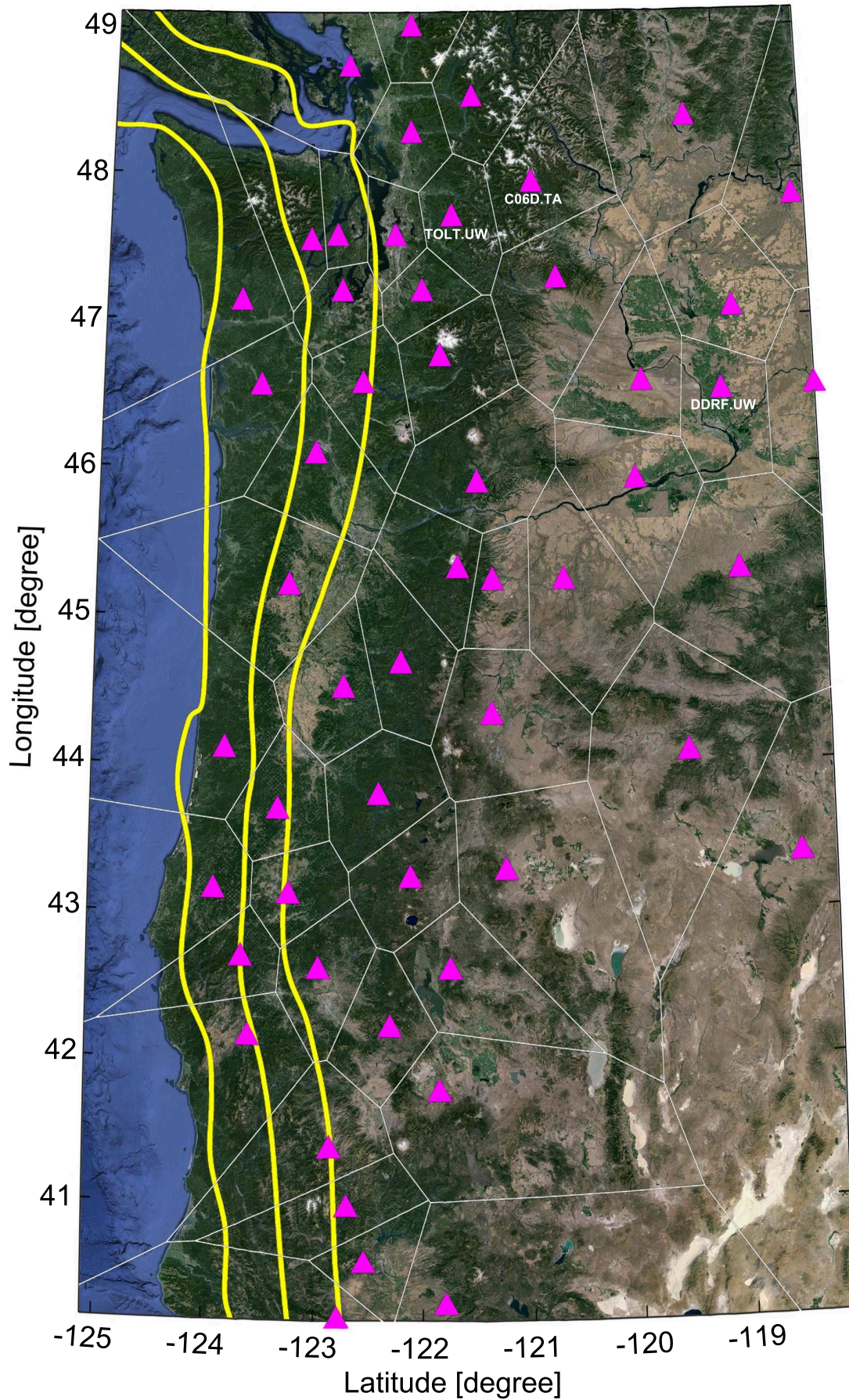


FIGURE 5.6: The 3-D array on the surface consists of 53 seismometers in Cascadia. Related Voronoi polygons are also displayed. The yellow lines indicate the isolines of 20, 30 and 40 km depth of the slab above a low velocity zone along the Cascadia margin [McCrory et al., 2006]. Triangles represent the receivers. The station code is indicated for three arbitrary stations used in the further investigations.

Here, the 3-D P-wave velocity model derived by Preston [2003] is considered. First arrivals of 1,433 high-quality local earthquakes recorded by the Pacific northwest Seismograph Network, and four active source seismic surveys and oceanic Moho (PmP) reflections were used in the integrated 3-D tomographic inversion for the P-wave velocity model [Preston, 2003]. The model comprises cells of dimension 4 km horizontally and 2 km vertically. I extended the model to cover the whole area under consideration (see Figure 5.7). The velocity is extended laterally in the x and y-direction, where the velocity remains constant along the longitudinal and transverse, i.e., x and y-axis from last xz and yz-plane of the original model to the boundaries of the new model. S-wave velocities are determined from P-wave velocities by considering constant Poisson's ratio  $\nu = 0.25$  for this model in Equation 3.2.

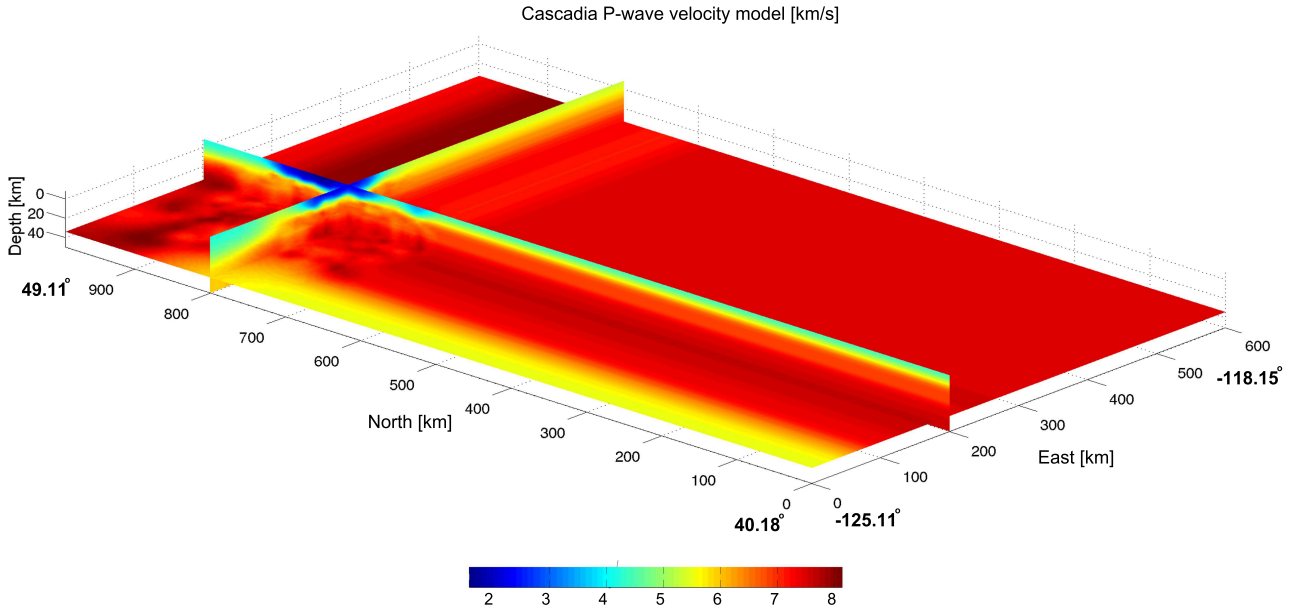


FIGURE 5.7: Cascadia 3-D velocity model derived by 3-D seismic tomography by Preston [2003]. The colour legend shows the P-wave velocity in km/s.

To further constrain the NVT detection, I applied a visual estimation of frequency anomalies by using the spectrograms<sup>3</sup> of each trace. For this investigation, time windows with a focussed spectrum were selected. A spectrogram analysis is commonly applied for processing signals and provides information about the time dependent frequency-content in a specified time window of data. Spectrograms can be utilised for event detection, since the arrival of an event changes the spectral content compared to the background

<sup>3</sup>vertical slices of spectral amplitudes versus frequencies, with slices plotted against time



noise. Figure 5.8 displays three recordings at different stations, kilometres apart, but at the same time, and their corresponding spectrograms. The geographic location of these stations is indicated in Figure 5.6. The intensity in db is increasing from cool to hot colours. A distinct maximum (hot colours) in a spectrogram indicates the existence of NVTs during the respective the 30 minutes time window, although the event is too weak to be visible in the seismogram.

Figure 5.9 presents example images for the detection of NVTs with positive and negative tremor detections. The image with positive detection has two distinct and well focussed maxima in the image which correspond to tremor locations. It shows the tremor's activity within the data under consideration. However, in the other image with negative detection, there is no distinct maximum. Therefore, it just comprises the background noise. In this case no tremor activity is observed.

The data were bandpass filtered from 1 to 8 Hz and the localisation was carried out for 30 minutes time buffers using a sliding time window of 5 minutes length. Figure 5.10 displays the image of the horizontal image section of a NVT event in Cascadia on 19th Nov. 2012 using cross-correlation stacking in the depth of the maximum image value ( $z=20\text{km}$ ). White stars in the images indicate a coinciding LFE location, according to the earthquake catalogue provided by USGS/NEIC, which occurred at 14 : 15 : 09 with a magnitude of 3.2 ML at Lat/Lon  $45.65^\circ / -122.76^\circ$  in a depth of 19 km. First arrival traveltimes are considered in the imaging procedure. I found a satisfactory match. The high amplitudes of the horizontal to vertical scaled image displays a focussed maximum close to the LFE event. The depth of the tremor observed close to the LFE event depth. This indicates that LFE occurring at the plate interface are accompanied by tremors. Moreover, scaling the horizontal images to vertical ones reduced the amount of noise fairly well, compared to the localisation image based on vertical component seismograms alone. it provides an image with a more focussed maximum at the source position. In this case, stacking the horizontal and vertical images led to an incorrect location.

Figure 5.11 illustrates the localisation image of a NVT event on 19th Jan. 2013 without and with acquisition footprint removal and geometrical spreading compensation. Black arrows in the images indicate the changes in the images. It is shown that the image is improved after the correction procedure, however in some parts correction led to artificial focussing in the image (see Figure 5.11(a2) relative to Figure 5.11(b2)). The localisation result with the correction is considerably better than the result without the correction.

Several smaller maxima are observed in the vicinity of the maximum value of the image. It may demonstrates that tremors can be explained as a swarm of small LFEs, each of which occurs as shear faulting on the subduction-zone plate interface. My result suggests that tremor and slow slip are different manifestations of a single process as Shelly et al. [2007] already presumed.

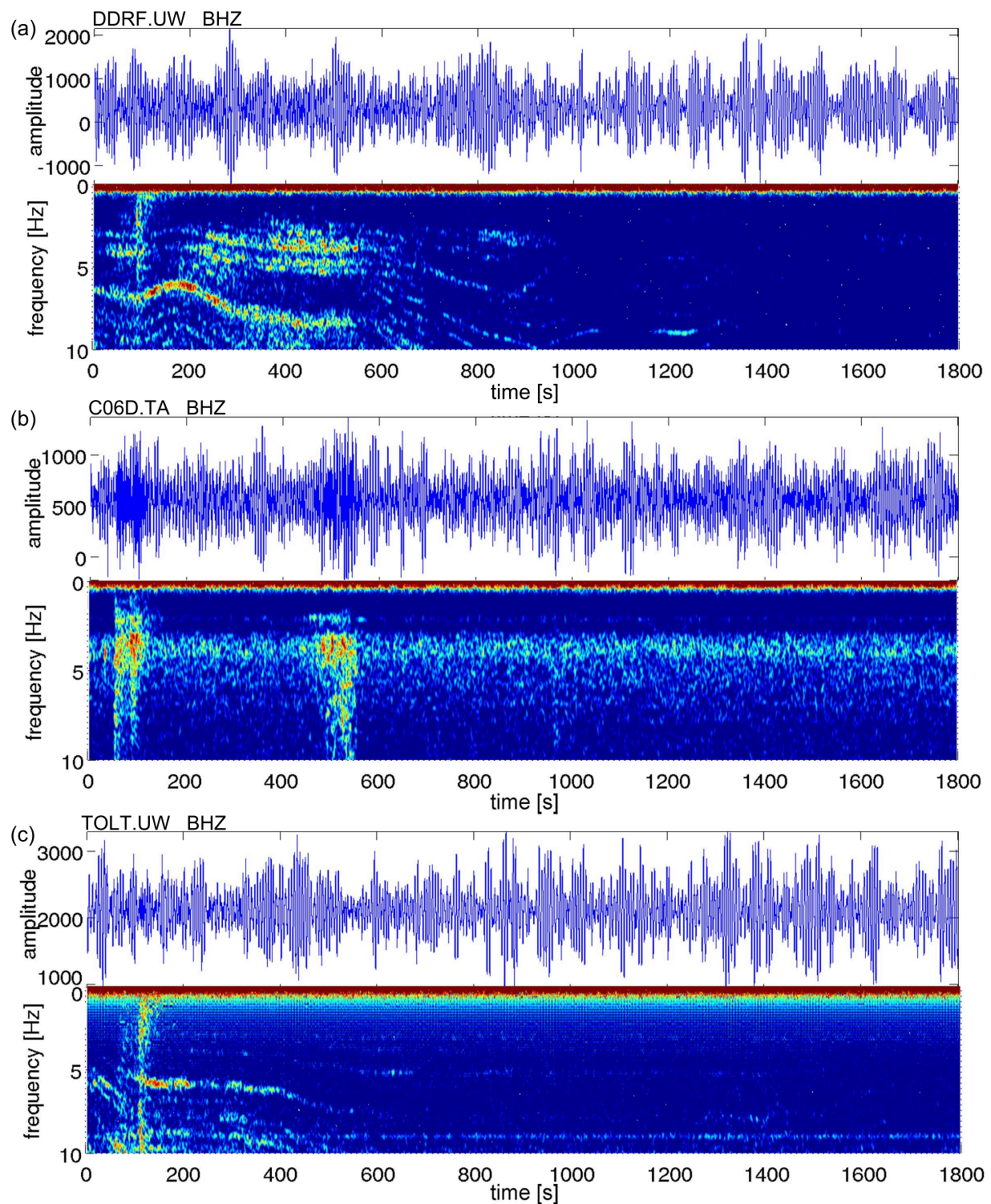


FIGURE 5.8: Example of the visual estimation of NVT detection on 19th Nov. 2012 at 14 : 15 : 00. (a), (b) and (c) are three vertical component recordings at different stations at the same time, and their corresponding spectrograms. The intensity in db is increasing from cool colours to hot colours. The maxima (hot colour) of the spectrograms indicate the existence of NVTs during a half hour time window. The station codes is indicated on the seismogram.

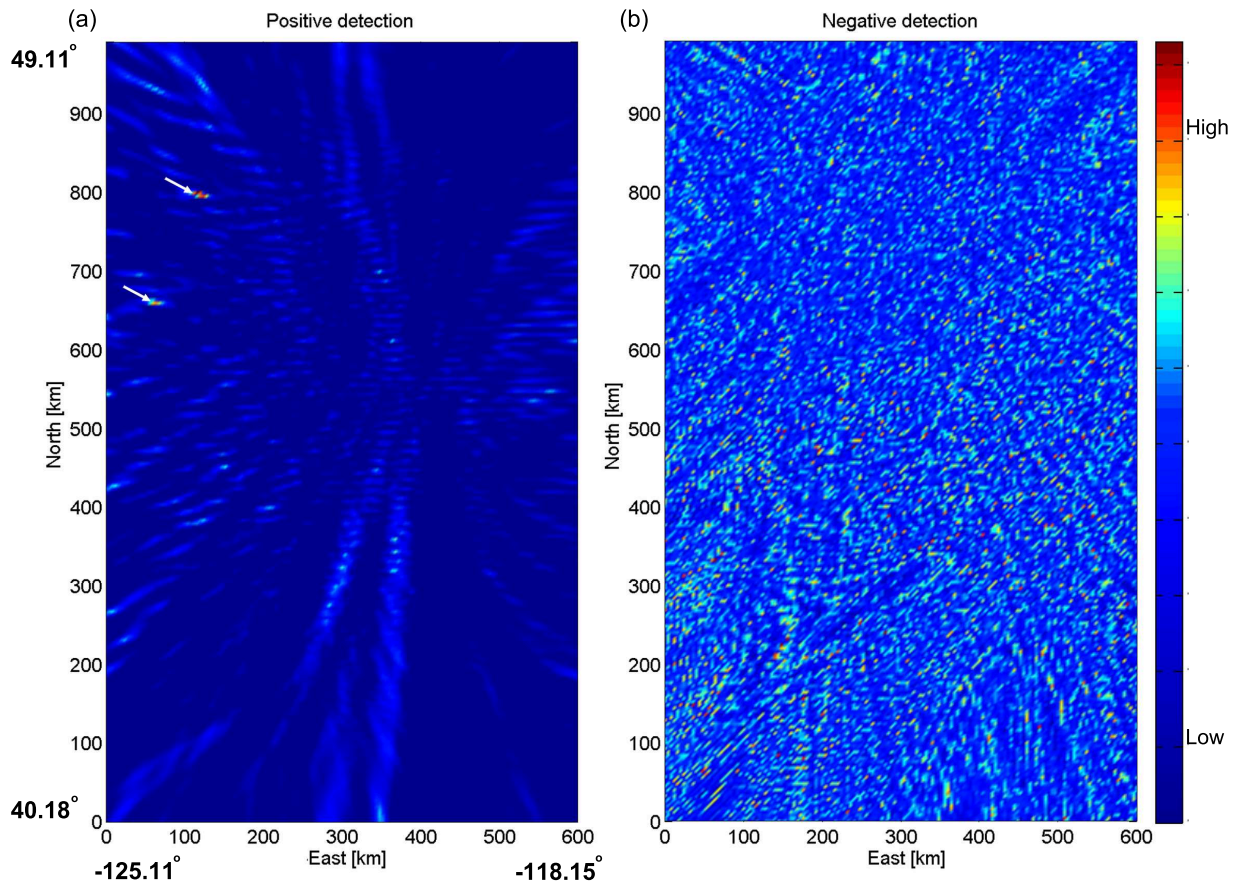


FIGURE 5.9: Example images of localisation with (a) positive and (b) negative tremor detection. Arrows indicate the tremor location.



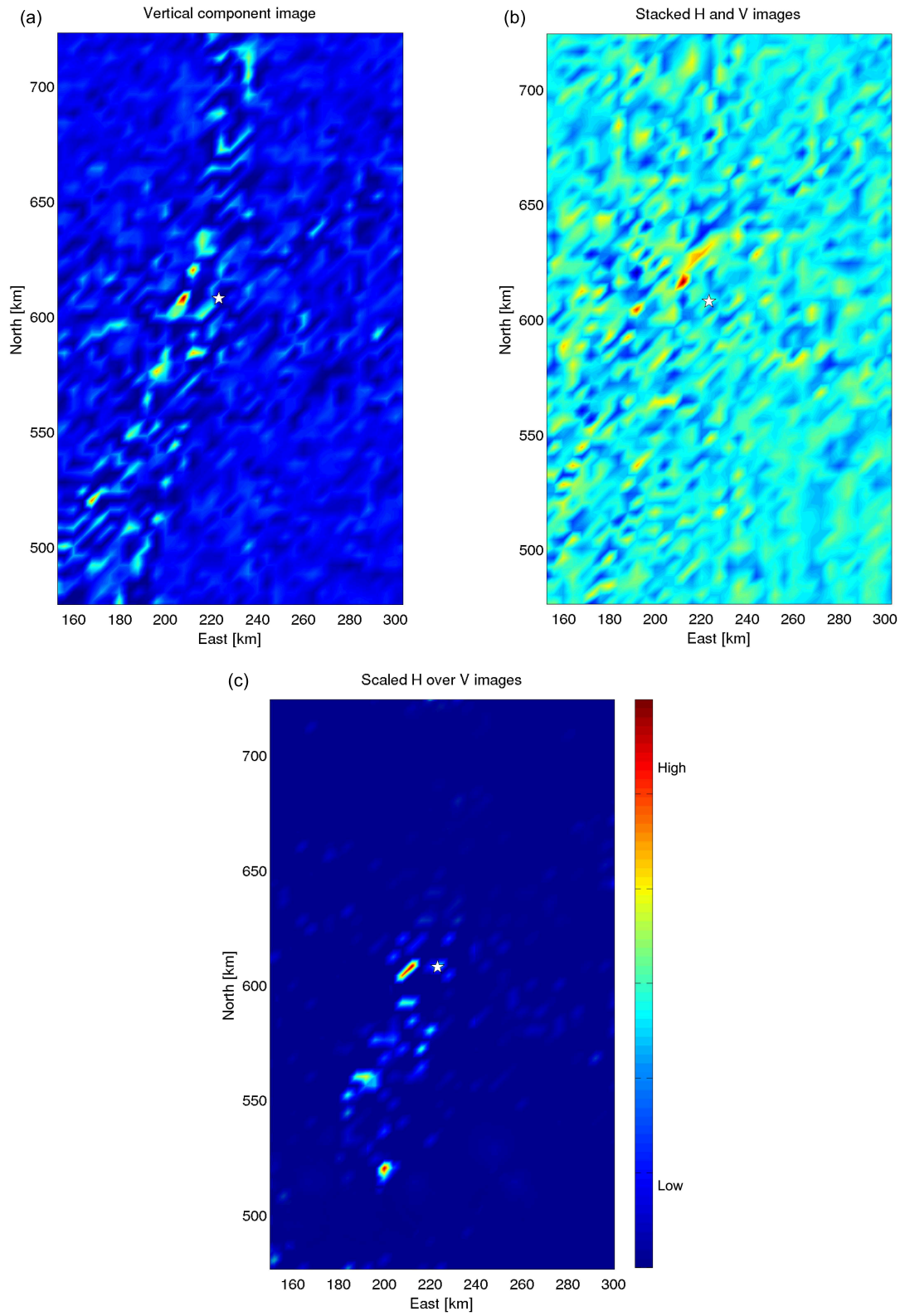


FIGURE 5.10: Horizontal image section for a NVT event in Cascadia on 19th Nov. 2012: (a) Localisation image based on vertical component seismograms (vertical image), (b) stacked horizontal and vertical images and (c) scaled horizontal to vertical image, at the depth of the maximum image value ( $z=20\text{km}$ ). The colour legend on the right shows the value of the image function amplitude. White stars in the images indicate the reference event location.



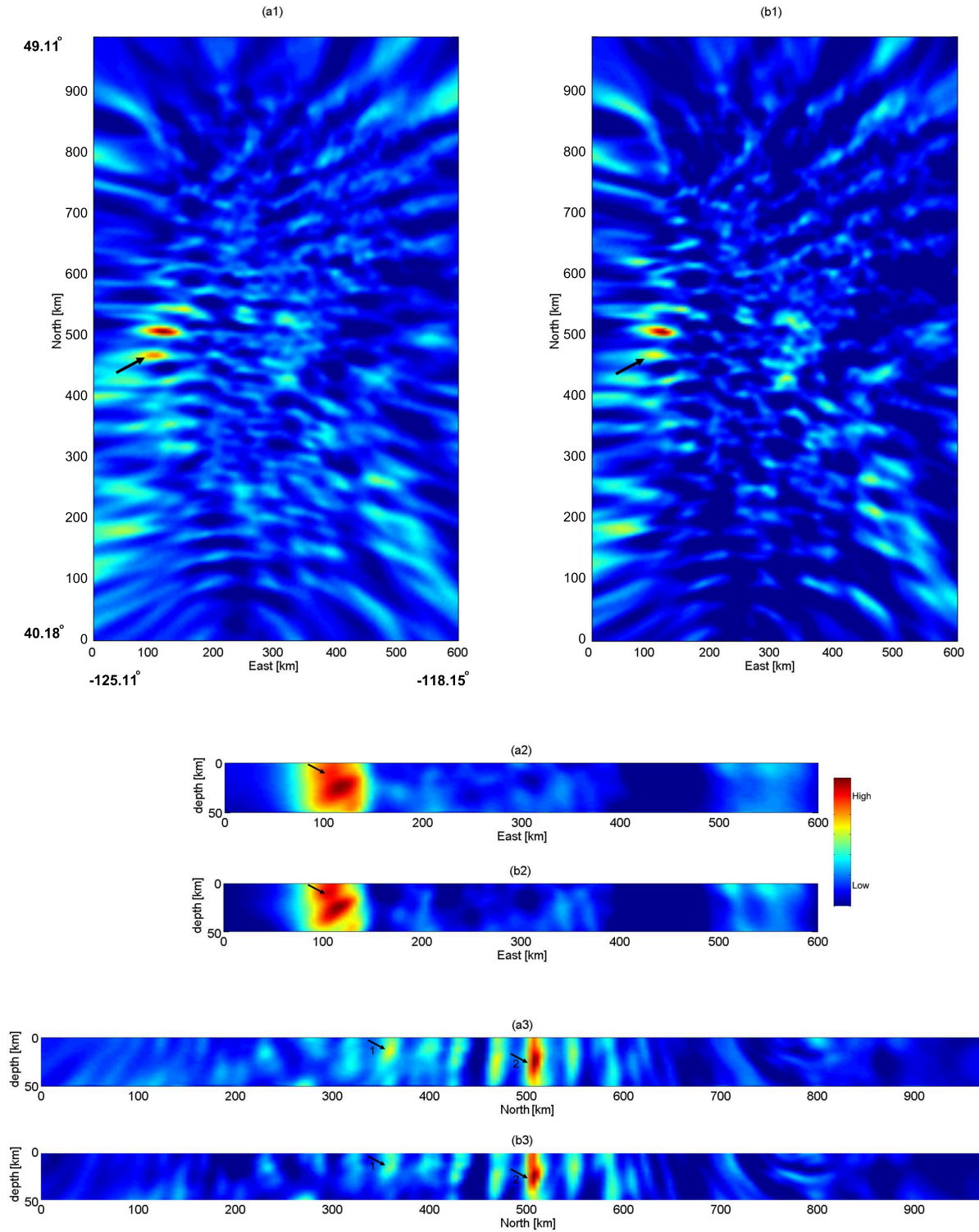


FIGURE 5.11: Localisation image for a NVT event on 19th Jan. 2013 in Cascadia. (a1) NE-section, (a2) EZ-section and (a3) NZ-section are shown without the acquisition footprint removal and geometrical spreading compensation, and with correction in (b1) NE-section, (b2) EZ-section and (b3) NZ-section. Black arrows indicate some changes in the images.

Figure 5.12 illustrates the 1-D amplitude section of the NVT event, localised in Cascadia on 27th Nov. 2012 without and with acquisition footprint removal (FP) and geometrical spreading correction (GS) performed individually. along north and east direction. The depth ( $40\text{km}$ ), north and east coordinates are taken at the real source position respectively. The blue line indicates the 1-D image function without any correction. The green line shows the image function with geometrical spreading compensation and the red line shows image function with the acquisition footprint removal. Although both corrections improve the image, the removal of the acquisition footprint obtains the higher value in the image function at source position. The application of the acquisition footprint removal and the geometrical spreading compensation decreased the amount of noise by increasing the amplitude of the image function at the source position.

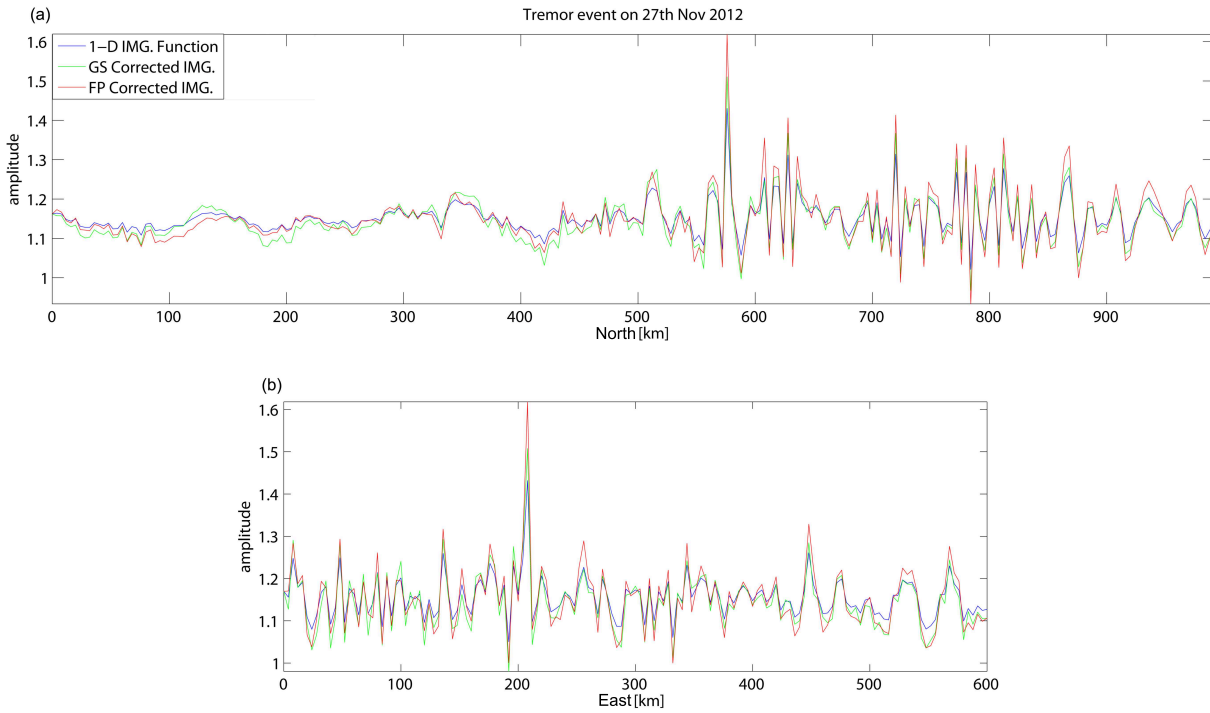


FIGURE 5.12: 1-D amplitude section without and with acquisition footprint removal (FP) and geometrical spreading correction (GS) performed individually. For the NVT event, localised in Cascadia on 27th Nov. 2012 along (a) north and (b) east direction. The depth ( $40\text{km}$ ), north and respectively east coordinates are taken at the real source position.

Figure 5.13 shows the localisation results where cross-correlation stacking was applied. I used the data of a LFE which occurred at Lat/Lon  $45.35^\circ / -123.2^\circ$  and a depth of  $23.3\text{ km}$  on 19th Jan. 2012 at 02 : 35 : 28 with a Magnitude of 2.3 ML. White stars in the images indicate the reference source position according to the earthquake catalogue provided by USGS/NEIC. Acquisition footprint removal and geometrical spreading compensation were applied before the localisation procedure. In the example shown in Figure 5.13 the

cloud of high amplitudes in the image function represents the NVT location. Several artefacts are observed in the vertical localisation image (see Figure 5.13(a)). Stacking the horizontal and vertical images led to a wrong location of the tremor (see Figure 5.13(b)). Whereas, scaling the horizontal by vertical image has reduced the amount of noise, and provides an image with a more focussed maximum at the source position (see Figure 5.13(c)).

Finally, Figure 5.14 shows the map of the tremor epicentres during the the Nov 2012-Jan 2013 period. Only strong detections are shown. The source time is colour-coded to illustrate temporal evolution. Even though tremors are hard to detect due to their lack of clear impulsive arrivals, Figure 5.14 shows that in general tremor activities are observed near the plate interface. It suggests that they are possibly a result of shear slip on the subduction fault. Moreover, tremor activity is mostly observed in northern area than the less active southern at 20-35 km depth, i.e. above the LVZ. It is important to note that tremors are not distributed uniformly, they appear in distinct patches. Moreover, tremors migration along the strike of subduction zone is shown, which started from centre, migrates to north then come back to centre.

Without proper imaging conditions, localisation may lead to misinterpretations and thus provide wrong information about the considered area. I showed that even weak tremor events in dataset episodes with a low SNR can be detected. The contribution of three components of seismograms can give reasonable estimates of tremor depths, which has been a highly debated issue since the tremors' discovery. The localisation images presented in this study are normalised, which means that the results does not depend on absolute amplitudes.

The procedure is applied to locate several slow earthquakes during the Nov 2012-Jan 2013 period. The median of the absolute differences between the locations of the events which are provided by USGS catalogue and which I localised with the CCS imaging method is approximately 5% percent. However it might be caused by different seismic datasets, as what is used in this study is a part of real time datasets provided by IRIS from a very spars array. Choosing a multiple dense seismic array dataset would lead to a more accurate result.

Tests on a reservoir area (of less than 10km) have shown that Cross-correlation stacking based imaging detects an event within seconds. This allows for real time monitoring of reservoir areas. Real time monitoring of a region with natural tectonic activity such as Cascadia is also possible. Although such areas are usually in the order of several 100 kilometres, the number of channels in such seismological survey is limited.

Although this study was restricted to the NVTs from Cascadia, the sequence of analyses presented in this study is potentially applicable to many similar phenomena; the only requirements are continuous records, velocity model and a reference catalogue.

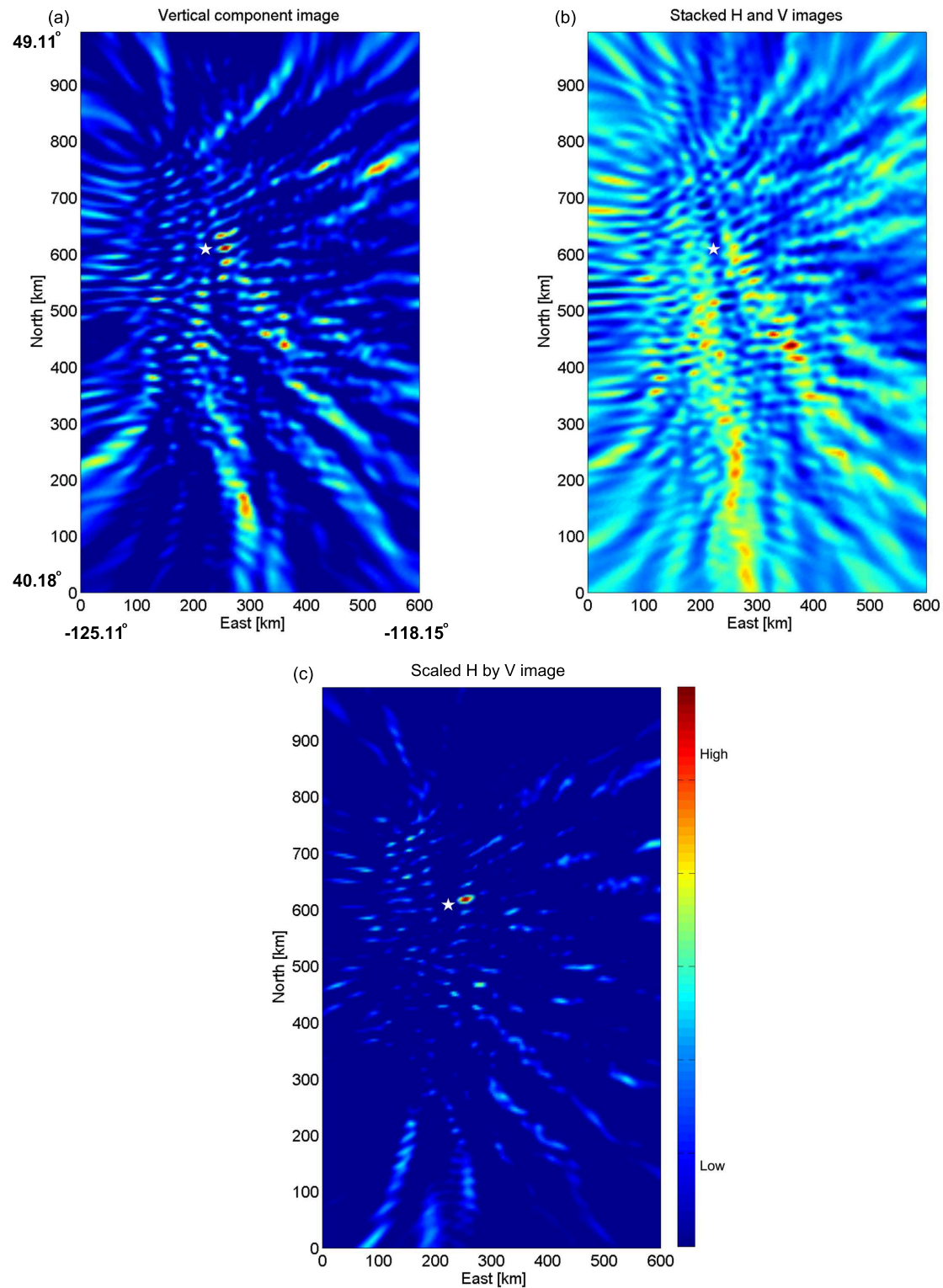


FIGURE 5.13: Horizontal image section for a NVT event in Cascadia on 19th Jan. 2013: Localisation result for the (a) vertical image, (b) stacked horizontal and vertical images and (c) scaled horizontal to vertical image, in the depth of the maximum image value ( $z=24$  km). Acquisition footprint reduction and geometrical spreading compensation were applied prior to the localisation procedure. White stars in the images indicate the LFE location suggested by USGS/NEIC.



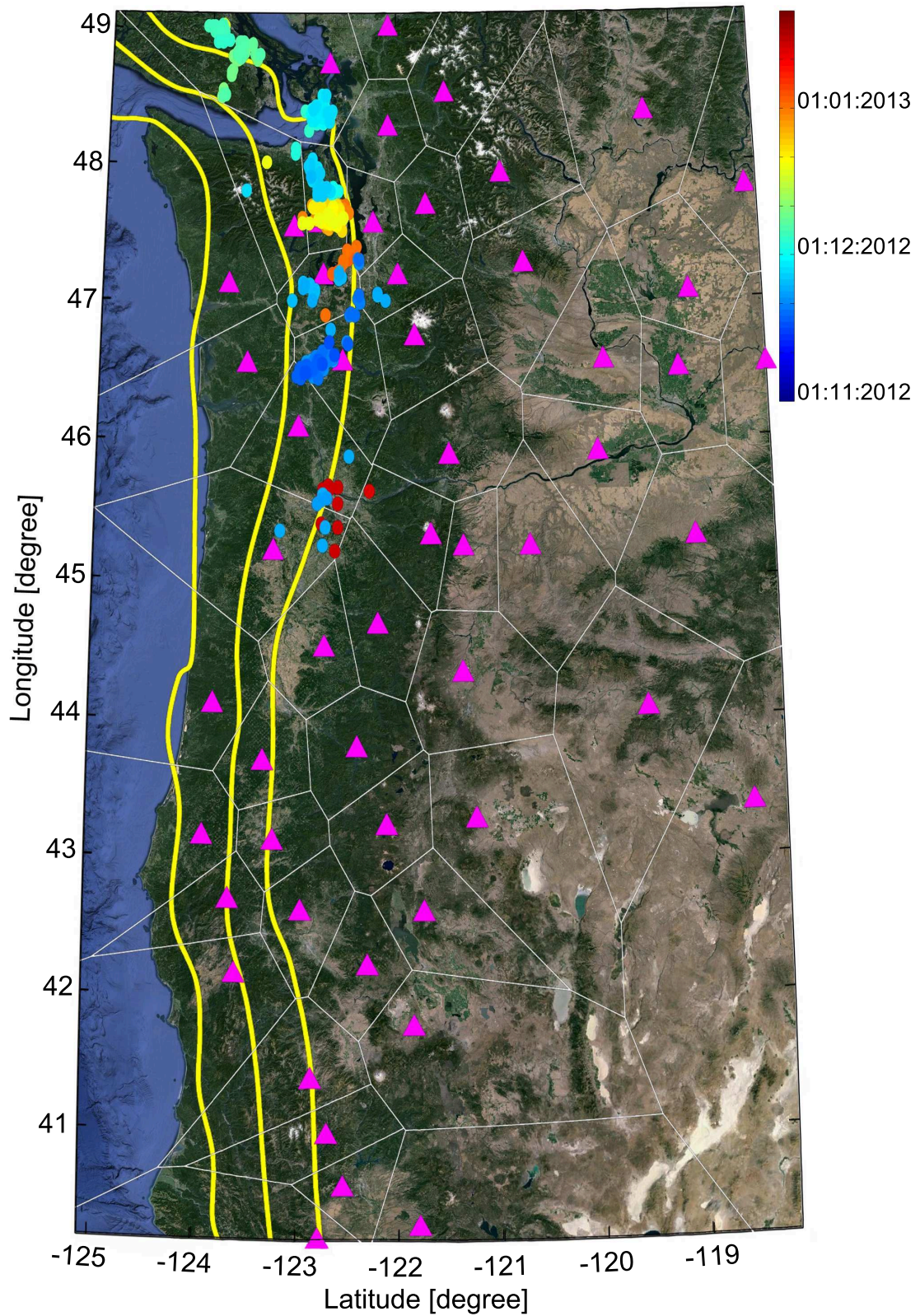


FIGURE 5.14: Satellite imagery of the Cascadia subduction zone and overlaid tremor epicentres (coloured circles) during the the Nov 2012-Jan 2013 period. Only strong detections are shown. The source time is colour coded.



## Chapter 6

# Conclusion

### 6.1 Summary

In this study a new imaging based procedure for localisation of seismic sources is presented. This procedure does not require event picking and uses all channels simultaneously. It is based on cross-correlation, which is a measure of the similarity of two waveforms as a function of time-lag between them. The approach was applied to synthetic data examples which were modelled with different source types, acquisition geometries and apertures.

Cross-correlation stacking has great potential to provide monitoring the subsurface. It appears to give well-determined locations of tremor events in 3-D space, and provides an analytical approach. Without proper imaging conditions, the localisation procedure may lead to misinterpretations, thus provide wrong information about the considered area. I have shown that even weak microtremor events in dataset episodes with a low SNR can be detected.

Cross-correlation stacking based imaging allows for real time monitoring of the subsurface which is the key issue in passive seismics. Tests on a reservoir area (less than 10 km) have shown that localisation procedure detects an event within seconds. Real time monitoring of a region with natural tectonic activity such as Cascadia is also possible. Although such areas are usually in the order of several 100 kilometres, the number of channels in such seismological survey is limited.

The accuracy of the velocity model is the main issue of localisation. The velocity model is expressed by the physical elastic moduli as Young's modulus, Poisson's ratio and density, which comprises two velocity models for both P-and S-waves in elastic media. The appropriate determination of both velocities is required to estimate the traveltimes correctly, to be able to accurately localise the seismic source. Contribution of P and S-waves in imaging may help to improve the seismic imaging. In this study P and S-wave

moveouts are considered separately in imaging condition, then stacked the localisation results. A poorly determination of velocity models may cause incorrect arrival times of signal and therefore lead to an unfocused image and spatial shift of the source.

The uniform illumination of the subsurface especially in complex models is crucial, a migration implementation would enhance the quality of the results. The influence of errors in velocity has examined in this study. In this study a time-lag cross-correlation has evaluated to countermand the effect of errors in velocity in localisation. In homogeneous case, the suggested imaging condition improved the result.

Since the Eikonal equation is a result of the high frequency approximation of the equation of motion for heterogeneous media, the moveout of the high frequency event matches better than the moveout of the traveltimes for the low frequency event. Deviations in moveout directly influence the localisation process. Because of the low frequency content, microtremor events are likely to be more effected by model complexity.

Depending on the method used to compute traveltimes, smoothing of the velocity model might be necessary. The localisation results using the traveltimes obtained for the unsmoothed velocity model displays a shift of the high amplitudes of the image to shallower levels. Smoothing of the input velocity model improved the localisation result. Smoothing of the velocity model can not exactly describe the averaging feature of wave propagation in complex structures where the prevailing wavelength is considerably larger than the spacial model variations. However, for the velocity models considered in this study, it helped to better localise the low frequency microtremor events.

In this study, ray tracing is used to compute the traveltime of first and most energetic arrivals. For the synthetic velocity model considered in this study, some depth differences in localisation results were observed when either first or most energetic arrivals were used.

In localisation process, Low frequency events may be more effected by model complexity since the computed traveltimes are inherently attributed to high frequency events. Deviations in moveout directly influence the localisation process.

It is intuitive that an array of three component receivers, compared to a vertical component array, provides even more information e.g. backazimuth, dips of the wave field and depth of the event, which can be used to increase the robustness of the localisation.

Imaging conditions have a strong influence in localisation results. In this study stacking horizontal and vertical images and also scaled horizontal image by vertical image are considered. It is important to note that both imaging conditions lead to the same results. Depending on the source type and contribution of S-wave in the stacked energy, scaling the horizontal by the vertical image may provide a better result.

Survey acquisition with sparsely and irregularly distributed receivers leave a footprint on the image. Weighting the data results in a more focussed image function. The acquisition



footprint removal allows for a separation of source and receiver effects. In this study, I present an algorithm for acquisition footprint suppression which is easy to understand and relatively fast. For land data sets with an acquisition footprint, an approach based on Voronoi polygons yields satisfactory results. Although it may generate some artefacts in the image which may lead to wrong source location.

To summarise, my approach is able to detect long duration tremor episodes, and unveils several tremor patches on the subduction interface during the Nov. 2012-Jan. 2013 period of episodic tremor and slip events in Cascadia. Seismic tremor and slow slip in Cascadia correlate well in space and time. The method provides a great resolution. Also the results have important implications for our general understanding of the causes of intraslab earthquakes, seismic hazards, and fluid processes within the shallowest portion of a warm subduction zone.

## 6.2 Outlook

This study has introduced a new localisation technique based on Cross-correlation. Application of the method to synthetic as well as field dataset examples illustrate that the method promises to become a powerful tool in image processing. A variety of factors influence the localisation results, e.g. traveltimes computation and accuracy, detecting sources with different properties, Geometrical spreading compensation, and the acquisition footprint. Some questions were raised during this study which are worth a thorough investigation.

The polarity of the direct waves depend on the take-off angle. Therefore, the polarities of the data amplitudes can be positive or negative. The role of the source radiation pattern in a reliable localisation needs to be studied.

Contribution of P and S-waves in imaging may help to improve the seismic imaging. In this study P and S-wave moveouts are considered separately in imaging condition, then stacked the localisation results. Considering P minus S-wave traveltimes simultaneously in imaging and correlation of P and S-wave images are only two examples of possible future research.

Another interesting subject could be considering the anisotropy. Seismic anisotropy is defined as the velocity dependency on direction or angle. In this study the performance of method in isotropic homogeneous and heterogeneous media is proved. The influence of anisotropic medium on localisation results has to be considered.

Tremor distribution shows long term tremor migration along the strike of the subduction zone in Cascadia and Japan. Stresses due to slow slip in a section of the fault causes slip and associated tremor in the adjacent section. The resulting progressive along-strike transfer of stress is responsible for the long-term migration of tremor during an

---

episodic tremor and slip event. What is not known, however, are the details of this migration pattern, its relationship with slow slip, and the underlying physics controlling the migration.

# List of Figures

1.1	Schematic passive technology . . . . .	3
2.1	Simulated seismograms in a homogeneous model . . . . .	8
2.2	The concept of the cross-correlation stacking procedure in a homogeneous model . . . . .	9
2.3	A snapshot of the calculation midway through fast sweeping procedure ordering 1 . . . . .	12
2.4	Schematic view of ray propagation in a media of increasing velocity with depth . . . . .	13
2.5	Illustration of H/V method [Nakamura, 2008]. . . . .	18
3.1	Localisation images of an explosive source in a homogeneous medium . . .	20
3.2	Comparison of the traveltimes contours . . . . .	22
3.3	Localisation of an explosive source in homogeneous medium . . . . .	23
3.4	The synthetic heterogeneous velocity model . . . . .	24
3.5	Vertical component seismograms in a heterogeneous model . . . . .	25
3.6	Localisation of a high frequency point source event in heterogeneous media	26
3.7	Localisation of a low frequency point source event in heterogeneous media	27
3.8	Localisation image of a synthetic microtremor signal in heterogeneous media	28
3.9	Smoothed velocity models using a Hamming window . . . . .	29
3.10	Travelttime contours of first arrivals and most energetic arrivals . . . . .	32
3.11	Localisation of a high frequency point source event in smoothed complex media . . . . .	33
3.12	Localisation of a low frequency point source event in smoothed complex media . . . . .	34
3.13	Localisation of a microtremor signal simulated by explosion source in smoothed complex media . . . . .	35
3.14	The comparison of the localisation results of a microtremor signal simulated by explosion source . . . . .	36
3.15	Localisation of a microtremor signal simulated by horizontal single force in smoothed complex media . . . . .	38
3.16	Localisation of a microtremor signal simulated by vertical single forces in smoothed complex media . . . . .	39
4.1	Raypath geometry for a point source in inhomogeneous medium . . . . .	42
4.2	Simplified grid construction for computing the area around each point . .	44
4.3	Definition and basic properties of Voronoi diagrams . . . . .	45
4.4	Schematic areas of Voronoi polygons . . . . .	47
4.5	The synthetic heterogeneous velocity model . . . . .	49

4.6	The 2-D array on the surface and the related Voronoi polygons . . . . .	49
4.7	Seismograms of the sources in a heterogeneous model . . . . .	50
4.8	Image function for a point source event set within the aperture in a complex media . . . . .	52
4.9	Image function for a point source event set at the edge of the aperture in a complex media . . . . .	53
4.10	1-D amplitude section without and with acquisition footprint removal and geometrical spreading correction performed individually . . . . .	54
5.1	The 1-D velocity model of a hydraulic fracture experiment. . . . .	56
5.2	Distribution of surface receivers along various profiles during monitoring of the hydraulic fracture treatment. A + represents a receiver and the injection pad is at the centre of receivers' lines. . . . .	57
5.3	Waveforms of particle velocity on vertical component geophones due to an induced microseismic event detected . . . . .	58
5.4	Localisation of an induced microseismic event in a complex medium. . . . .	59
5.5	Structure of the Cascadia subduction zone. The thinner oceanic plate is subducting beneath the thicker continental plate offshore. . . . .	61
5.6	The 3-D array on the surface consists of 53 seismometers in Cascadia. Related Voronoi polygons are also displayed. . . . .	63
5.7	Cascadia 3-D velocity model derived by 3-D seismic tomography . . . . .	64
5.8	Example of visual estimate of NVT detection from vertical component recordings and corresponding spectrograms . . . . .	66
5.9	Example images of localisation in Cascadia with positive and negative tremor detection . . . . .	67
5.10	Horizontal image section for a NVT event in Cascadia . . . . .	68
5.11	Localisation image for a NVT event in Cascadia without and with correction . . . . .	69
5.12	1-D amplitude section for the NVT event, localised in Cascadia without and with correction . . . . .	70
5.13	Horizontal image section for a NVT event in Cascadia . . . . .	72
5.14	Satellite imagery of the Cascadia subduction zone and its tremor epicentres . . . . .	73

# Bibliography

- Aso, N., Ohta, K., and Ide, S. (2011). Volcanic-like low-frequency earthquakes beneath Osaka Bay in the absence of a volcano. *Geophysical Research Letters*, 38(L08303).
- Aster, R. (2011). Fundamentals of ray tracing. Technical report, <http://www.ees.nmt.edu/outside/courses/GEOP523/Docs/rays.pdf>.
- Bortfeld, R. (1989). Geometrical ray theory: rays and traveltimes in seismic systems (second-order approximation of the traveltimes). *Geophysics*, 54:342–349.
- Bruss, A. (1982). The eikonal equation: some results applicable to computer vision. *Journal of Mathematical Physics*, 23(5):890–896.
- Calvert, A. J., Preston, L. A., and Farahbod, A. M. (2011). Sedimentary underplating at the Cascadia mantle-wedge corner revealed by seismic imaging. *Nature Geoscience*, 4:545–548.
- Canning, A. and Gardner, G. H. F. (1998). Reducing 3-D acquisition footprint for 3-D DMO and 3-D prestack migration. *Geophysics*, 63:1177–1183.
- de Berg, M., Cheong, O., van Kreveld, M., and Overmars, M. (2008). *Computational geometry (3rd edition)*. Springer-Verlag.
- Detrixhe, M., Gibou, F., and Min, C. (2013). A parallel fast sweeping method for the eikonal equation. *Journal of Computational Physics*, 237:46–55.
- Eisner, L., De La Pena, A., Wessels, S., Barker, W. B., and Heigl, W. M. (2011). Why surface monitoring of microseismic events works. In *Expanded Abstracts*, number PAS10. Third Passive Seismic Workshop - Actively Passive!
- Eisner, L., Fischer, T., and Le Calvez, J. (2006). Detection of repeated hydraulic fracturing (out-of-zone growth) by microseismic monitoring. *The Leading Edge*, 25(5):547–554.
- Eisner, L., Heigl, W. M., Duncan, P. M., and Keller, W. R. (2009). Uncertainties in passive seismic monitoring. *The Leading Edge*, 28(6):648–655.

- Emidio, A. and Nunes, L. (2010). Pitfalls of tremor-like signals for hydrocarbon exploration in producing oil fields in Potiguar Basin, northeast Brazil. *The Leading Edge*, 29(7):826–830.
- Falcone, M. and Ferretti, R. (1994). Discrete time high-order schemes for viscosity solutions of Hamilton-Jacobi-Bellman equations. *Numerische Mathematik*, 67:315–344.
- Gajewski, D., Anikiev, D., Kashtan, B. M., Tessmer, E., and Vanelle, C. (2007). Source location by diffraction stacking. In *Expanded Abstracts*, number P215. 69th EAGE Conference and Exhibition.
- Gajewski, D., Coman, R., and Vanelle, C. (2002). Amplitude preserving Kirchhoff migration: a travelttime based strategy. *Studia Geophysica et Geodaetica*, 46(2):193–211.
- Gajewski, D. and Tessmer, E. (2005). Reverse modeling for seismic event characterization. *Geophysical Journal International*, 163:276–284.
- Geoltrain, S. and Brac, J. (1993). Can we image complex structures with first arrival travelttime? *Geophysics*, 58:564–575.
- Ghosh, A. (2011). *Imaging slow earthquakes in Cascadia using seismic arrays*. PhD thesis, University of Washington.
- Ghosh, A., Vidale, J. E., Sweet, J. R., Creager, K. C., and Wech, A. G. (2009). Tremor patches in Cascadia revealed by seismic array analysis. *Geophysical Research Letters*, 36(L17316).
- Graf, R., Schmalholz, S. M., Podladchikov, Y., and Saenger, E. H. (2007). Passive low frequency spectral analysis: Exploring a new field in geophysics. *World Oil*, 228:47–52.
- Grasso, J. R. (1992). Mechanics of seismic instabilities induced by the recovery of hydrocarbons. *Pure and Applied Geophysics*, 139:507–533.
- Gray, S. (2000). Velocity smoothing for depth migration: How much is too much? In *Expanded Abstracts*, pages 1055–1058. SEG Technical Program.
- Helmsen, J., Puckett, E., Colella, P., and Dorr, M. (1996). Two new methods for simulating photolithography development in 3D. SPIE Proceedings.
- Hubral, P., Schleicher, J., and Tygel, M. (1992). Three-dimensional paraxial ray properties: Part I. Basic relations. *Journal of Seismic Exploration*, 1:265–279.
- Johnson, D. H. and Dudgeon, D. E. (1993). *Array Signal Processing: Concepts and Techniques*. Prentice Hall, Upper Saddle River, N. J.
- Julian, B. R. and Gubbins, D. (1977). Three-dimensional seismic ray tracing. *Geophysics*, 43:95–113.

- Kao, H., Shan, S.-J. and Draggert, H., Rogers, G., Cassidy, J. F., and Ramachandran, K. (2005). A wide depth distribution of seismic tremors along the northern Cascadia margin. *Nature*, 436:841–844.
- Kao, H. and Shan, S.-J. (2004). The Source-Scanning Algorithm: mapping the distribution of seismic sources in time and space. *Geophysical Journal International*, 157:589–594.
- Kawase, H., Sánchez-Sesma, F. J., and Matsushima, S. (2011). The Optimal Use of Horizontal-to-Vertical Spectral Ratios of Earthquake Motions for Velocity Inversions Based on Diffuse-Field Theory for Plane Waves. *Bulletin of the Seismological Society of America*, 101(5):2001–2014.
- La Rocca, M., Creager, K. C., Galluzzo, D., Malone, S., Vidale, J. E., Sweet, J. R., and Wech, A. G. (2009). Cascadia tremor located near plate interface constrained by S minus P wave times. *Science*, 323:620–623.
- Lambert, M. A., Schmalholz, S. M., Saenger, E. H., and Steiner, B. (2009). Low-frequency microtremor anomalies at an oil and gas field in Voitsdorf, Austria. *Geophysical Prospecting*, 57(3):393–411.
- Malladi, R. and Sethian, J. A. (1996). A unified approach to noise removal, image enhancement, and shape recovery. *IEEE Transactions on Image Processing*, 5(11):1554–1568.
- McClausland, W., Malone, S., and Johnson, D. (2005). Temporal and spatial occurrence of deep non-volcanic tremor: From Washington to northern California. *Geophysical Research Letters*, 32(L24311).
- McCrory, P. A., Blair, J. L., Oppenheimer, D. H., and Walter, S. R. (2006). Depth to the Juan de Fuca slab beneath the cascadia subduction margin: A 3-d model for sorting earthquakes. Data series 91 version 1.2, USGS Data Service.
- Miyazawa, M. and Mori, J. (2005). Detection of triggered deep low-frequency events from the 2003 Tokachi-Oki earthquake. *Geophysical Research Letters*, 32(L10307).
- Nakamura, Y. (1989). A method for dynamic characteristics estimation of subsurface using microtremor on the ground surface. *Quarterly Report of RTRI*, 30(1):25–33.
- Nakamura, Y. (2008). On the H/V spectrum. In *Expanded Abstracts*, number 14wcee–hv. 14th World Conference on Earthquake Engineering.
- Newman, P. (1973). Divergence effect in a layered earth. *Geophysics*, 38:481–488.
- Obara, K. (2002). Nonvolcanic deep tremor associated with subduction in southwest Japan. *Science*, 296:1679–1681.



- Obara, K. and Hirose, H. (2006). Non-volcanic deep low-frequency tremors accompanying slow slips in the southwest Japan subduction zone. *Tectonophysics*, 417:33–51.
- Popovici, A. M. and Sethian, J. A. (2002). 3-D imaging using higher order fast marching traveltimes. *Geophysics*, 67:604–609.
- Preston, L. A. (2003). *Simultaneous inversion of 3D velocity structure, hypocenter locations, and reflector geometry in Cascadia*. PhD thesis, University of Washington.
- Rawlinson, N., Hauser, J., and Sambridge, M. (2007). Seismic ray tracing and wavefront tracking in laterally heterogeneous media. *Advances in Geophysics*, 49:203–267.
- Rogers, G. and Dragert, H. (2003). Episodic tremor and slip on the Cascadia subduction zone: The chatter of silent slip. *Science*, 300:1942–1943.
- Rubinstein, J. L., La Rocca, M., Vidale, J. E., Creager, K. C., and Wech, A. G. (2008). Tidal modulation of non-volcanic tremor. *Science*, 319:186–189.
- Rutledge, J. T. and Phillips, W. S. (2003). Hydraulic stimulation of natural fractures as revealed by induced microearthquakes, carthage cotton valley gas field, east texas. *Geophysics*, 68:441–452.
- Ryberg, T., Haberland, C., Fuis, G. S., Ellsworth, W. L., and Shelly, D. R. (2010). Locating non-volcanic tremor along the San Andreas Fault using a multiple array source imaging technique. *Geophysical Journal International*, 183(3):1485–1500.
- Saenger, E. H., Torres, A., Rentsch, S., Lambert, M., Schmalholz, S. M., and Mendez-Hernandez, E. (2007). A hydrocarbon microtremor survey over a gas field: Identification of seismic attributes. In *Expanded Abstracts*, pages 1277–1281. SEG/San Antonlo annual meeting.
- Sánchez-Sesma, F. J., Rodríguez, M., Iturrarán-Viveros, U., Luzón, F., Campillo, M., Margerin, L., García-Jerez, A., Suárez, M., Santoyo, M. A., and Rodríguez-Castellanos, A. (2011). A theory for microtremor H/V spectral ratio: Application for a layered medium. *Geophysical Journal International*, 183:221–225.
- Shearer, P. M. (2009). *Introduction to seismology, Second Edition*. Cambridge University Press.
- Shelly, D. R., Berozal, G. C., and Ide, S. (2007). Non-volcanic tremor and low-frequency earthquake swarms. *Nature*, 446:305–307.
- Steiner, B. (2009). *Time reverse modeling of low-frequency microtremors*. PhD thesis, ETH Zurich.
- Steiner, B., Saenger, E., and Schmalholz, S. (2008). Time reverse modeling of low-frequency microtremors: Application to hydrocarbon reservoir localization. *Geophysical Research Letters*, 35(L03307).

- Tessmer, E. (2000). Seismic finite-difference modeling with spatially varying time steps. *Geophysics*, 65(4).
- Ursin, B. (1990). Offset-dependent geometrical spreading in a layered medium. *Geophysics*, 55(4):492–496.
- Usher, P. J., Angus, D. A., and Verdon, J. P. (2013). Influence of a velocity model and source frequency on microseismic waveforms: some implications for microseismic locations. *Geophysical Prospecting*, 61:334–345.
- Vanelle, C. (2002). *Traveltime-Based True-Amplitude Migration*. PhD thesis, Universität Hamburg.
- Vanelle, C. and Gajewski, D. (2003). Determination of geometrical spreading from traveltimes. *Journal of Applied Geophysics*, 54:391–400.
- Červený, V. (2001). *Seismic Ray Theory*. Cambridge University Press.
- Vidale, J. (1988). Finite-Difference Calculation of Travel Times. *Bulletin of the Seismological Society of America*, 78(6):2062–2076.
- Voronoi, G. F. (1908). Nouvelles applications des paramètres continus à la théorie de formes quadratiques. *Journal für die reine und angewandte Mathematik*, 134:198–287.
- Šílený, J. and Milev, A. (2005). Source mechanism: Dipole vs. single force application to mining induced seismic events in deep level gold mines in South Africa. In *Expanded Abstracts*, pages 259–265. 6th Int. Conference Rockbursts and Seismicity in Mines.
- Winter, R. G. and Steinberg, A. M. (2008). *Coherence*. AccessScience@McGraw-Hill.
- Zhao, H. (2004). A fast sweeping method for eikonal equations. *Mathematics of Computation*, 74(250):603–627.
- Zhebel, O. (2013). *Imaging of seismic events. The role of imaging conditions, acquisition geometry and source mechanisms*. PhD thesis, Universität Hamburg.
- Zhebel, O., Gajewski, D., and Vanelle, C. (2011). Localization of seismic events in 3D media by diffraction stacking. In *Expanded Abstracts*, number C005. 73rd EAGE Conference and Exhibition.

## *Acknowledgements*

Foremost, I would like to express my sincere appreciation to my advisors Prof. Dr. Dirk Gajewski and Dr. Claudia Vanelle for the continuous support of my doctoral research and my committee members.

My sincere thanks also go to sponsors of WIT consortium and University of Hamburg doctoral fellowships in accordance with HmbNFG for financial support. Credits for the good atmosphere in Applied seismics group of the University of Hamburg go to it's leader, Prof. Dr. Dirk Gajewski, and all of it's members. Especially Manizheh Vefagh and Dr. Oksana Zhebel, I think of much more as friends than as colleagues.

I am grateful to my colleagues at Institute of Geophysics, especially Dr. Ali Dehghani for his generous help and support.

I especially thank Manizheh Vefagh, Mohsen Koushesh, Ivan Abakumov and Inka Zinoni for proofreading of this work.

I thank Dr. Brian Steiner, from Proseis AG, and Dr. Leiph Alexander Preston, from Sandia National Laboratories, for scientific collaborations in different parts of this research.

The last but not the least, I am deeply thankful to my family.

## *Eidesstattliche Versicherung*

Hiermit versichere ich, die vorliegende Arbeit selbstständig angefertigt und nur die angegebenen Hilfsmittel verwendet zu haben.

Mehrnoosh Behzadi